

Enhancing solar cells with plasmonic nanovoids



Niraj Narsey Lal

Clare Hall
Cavendish Laboratory
University of Cambridge

A dissertation submitted for the degree of
Doctor of Philosophy

June 2012

Declaration

This report is an account of research undertaken between January 2009 and June 2012 at The University of Cambridge, United Kingdom. This dissertation is my own work and contains nothing which is the outcome of work done in collaboration with others except where specifically acknowledged in the customary manner. The report has not been submitted in whole or part for a degree in any university and is less than 60,000 words.

Niraj Narsey Lal
June 2012

Acknowledgements

There are so many people that I would like to thank for making this journey possible. First, I'd like to thank my supervisor Jeremy Baumberg for teaching me how to ask good questions. It has been a privilege to learn with a professor who is unafraid of new ideas and technologies - I feel as if I absorbed how to be energetic and creative with science just by being around him. It's been organic-plasmonic Jeremy, thanks heaps.

I'd like to thank the Gates Trust for giving me the opportunity to study at Cambridge. To have this scholarship weighed on the same ledger as the lives of 1 billion people currently living in extreme poverty, is sobering. I can only hope that the work that comes from this thesis, and the future work that I achieve because of it, can somehow justify that investment.

I'd like to thank all the post-docs that I've been able to work with in the NanoPhotonics Group. Sumeet Mahajan for teaching me how to fabricate nanovoids and be an apprentice chemist. Bruno Soares for teaching me how to understand plasmons and swim more efficiently. Fumin Huang for the pak-choi seeds and for being patient with photovoltaics. And Matt Hawkeye for being a great sounding board and generally chilled-out guy in the office.

To all the collaborators I've been able to work with, thanks so much. Dr Jatin Sinha for making countless silver nanovoid samples to get this project going. Professor Javier de Abajo for being patient with theory and showing me what can be done with a pencil and paper. And Mathias Arens for giving BEMAX a good crack and for showing me what it's like on the other side of the desk - I look forward to hearing stories of the world-changing things you'll be getting up to.

To everyone in the NanoPhotonics group, thanks for making the lab the incredibly dynamic place that it is. Thanks especially to all my office mates in both Kapitza and the Fishbowl, and to James and Peter - it's been fun being on the plasmonics ride together.

I'd also like to thank all the assistant staff that make the Cavendish a great place to be. Zina for telling me about Lithuania. Mark for always being cheery in the Bragg side. Nigel for showing me how to machine metal. Colin for making the computers work in one of the most demanding and tech-savvy places in Cambridge. Antony for always poking fun, and Richard for the lunchtime runs. I'd especially like to thank Angela for all her Marje

Proops advice, and for generally being just lovely.

To Arco Iris for waking me up to the world of samba drumming, and to The Valence Band for having such a lame name. It's been so much fun to play together. I'm going to miss it like crazy. To the lads at CHFC and CUARFC, cheers for the kickarounds.

I'd like to thank my housemates Andrew, Joe and Alexandra - Auckland has been such a great home. Thanks too to Stella, Talia, Henning, and Stefan and Lisa for being extended family in Cambridge.

To my family in Australia, Mum and Dad I can't thank you enough. Thanks for giving me this solid ground to launch from. Yo and Chris - I know you guys say I should pay it forward - and I hope I can someday, but I want to say thanks for being there for me and reminding me of the important things.

Gabba, thanks for being my early sunshine in England. And Garance, I'd like to thank whatever butterfly flapped its wings to let us be together. You're awesome.

Finally, I'd like to thank my brand new little nephew Jayan for being motivation to make the world a better place, and motivation also to hurry up and finish so that I can come home and teach you to surf. This one's for you little fella.

Abstract

This thesis explores the use of plasmonic nanovoids for enhancing the efficiency of thin-film solar cells. Devices are fabricated inside plasmonically-resonant nanostructures, demonstrating a new class of plasmonic photovoltaics. Novel cell geometries are developed for both organic and amorphous silicon solar cell materials. An external-quantum efficiency rig was set up to allow simultaneous microscope access and micrometer-precision probe-tip control for optoelectronic characterisation of photovoltaic devices. An experimental setup for angle-resolved reflectance was extended to allow broadband illumination from 380 - 1500 nm across incident angles 0 - 70° giving detailed access to the energy-momentum dispersion of optical modes within nanostructured materials.

A four-fold enhancement of overall power conversion efficiency is observed in organic nanovoid solar cells compared to flat solar cells. The efficiency enhancement is shown to be primarily due to strong localised plasmon resonances of the nanovoid geometry, with close agreement observed between experiment and theoretical simulations. Ultrathin amorphous silicon solar cells are fabricated on both nanovoids and randomly textured silver substrates. Angle-resolved reflectance and computational simulations highlight the importance of the spacer layer separating the absorbing and plasmonic materials. A 20% enhancement of cell efficiency is observed for nanovoid solar cells compared to flat, but with careful optimisation of the spacer layer, randomly textured silver allows for an even greater enhancement of up to 50% by controlling the coupling to optical modes within the device.

The differences between plasmonic enhancement for organic and amorphous silicon solar cells are discussed and the balance of surface plasmon absorption between a semiconductor and a metal is analytically derived for a broad range of solar cell materials, yielding clear design principles for plasmonic enhancement. These principles are used to outline future directions of research for plasmonic photovoltaics.

Contents

Declaration	i
Acknowledgements	ii
Abstract	v
Nomenclature	ix
1 Introduction	2
1.1 Motivation and context	2
1.2 Plasmonic photovoltaics	5
1.3 Thesis layout	7
2 Background theory	8
2.1 Plasmonics	8
2.1.1 Overview	9
2.1.2 Electromagnetics of metals	10
2.1.3 The Drude model	11
2.1.4 Surface plasmon polaritons	13
2.1.5 Localised surface plasmons	16
2.2 Photovoltaics	21
2.2.1 Energy-level diagrams	22
2.2.2 Solar cell equation	23
2.2.3 Charge transport	26
2.2.4 Organic semiconductors	26
2.2.5 Amorphous silicon	28
2.3 Plasmonic photovoltaics	30
2.3.1 Summary of relevant length scales	30
2.3.2 Plasmonic interactions in thin films	31
2.3.3 Plasmon absorption balance	32
2.3.4 Material considerations	33

3	Literature review	35
3.1	Particle plasmon enhanced solar cells	35
3.2	Plasmonic surface solar cells	38
3.2.1	Plasmonic rear-surface contacts	39
3.2.2	Detrimental plasmonic absorption	40
3.3	Summary	41
4	Nanovoid solar cell design and fabrication	43
4.1	Motivations	43
4.2	Nanovoid photovoltaics	44
4.3	Device design considerations	45
4.3.1	Material choice	46
4.4	Deposition techniques	48
4.4.1	Plasma-enhanced chemical vapour deposition	48
4.4.2	Spin-coating	49
4.4.3	Sputter-coating	49
4.4.4	Metal evaporation	50
4.4.5	Dye-sensitized solar cells	50
4.5	Nanovoid fabrication	51
4.5.1	Template deposition	51
4.5.2	Electrochemical plating	52
4.6	Nanovoid plasmon control	54
4.7	Summary	55
4.7.1	Organic nanovoid solar cell	56
4.7.2	Amorphous silicon nanovoid solar cell	57
5	Characterisation and simulation	58
5.1	Optical characterisation	58
5.2	Electrical characterisation	60
5.3	Modelling	61
5.3.1	BEMAX	61
5.3.2	Lumerical	63
5.4	Summary	65
6	Organic plasmon-enhanced nanovoid solar cells	66
6.1	Introduction	66
6.2	Methods	67
6.3	Results	69
6.3.1	Angularly-resolved reflectance	69
6.3.2	Theoretical simulation	70
6.3.3	Photocurrent measurements	72
6.4	Discussion	74
6.5	Conclusions	75

7	Amorphous silicon plasmonic solar cells	76
7.1	Introduction	76
7.1.1	Introduction to spacer layers	77
7.2	Methods	78
7.3	Geometry	80
7.3.1	Nanovoids	80
7.3.2	Randomly textured	83
7.3.3	Flat	86
7.4	Discussion	87
7.4.1	Simulations	87
7.4.2	Spectral analysis	90
7.4.3	Geometry and curvature	92
7.5	Amorphous silicon near-field absorption	94
7.6	Conclusions	94
8	Design principles and ongoing research	96
8.1	Plasmon absorption balance	96
8.2	Design principles	98
8.3	Ongoing research	100
8.3.1	Advanced nanovoid photovoltaics	100
8.3.2	Optimising random textures	102
8.3.3	Pyramid plasmonics for silicon PV	103
8.4	Summary	105
9	Conclusions	106
	List of publications	108
	References	110

Nomenclature

Roman symbols

- i Imaginary number = $\sqrt{-1}$
- h Planck's constant = $6.626 \times 10^{-34} Js$
- c Speed of light = $2.998 \times 10^8 ms^{-1}$
- e Electron charge = $1.602 \times 10^{-19} C$
- E** Electric field vector
- B** Magnetic induction vector
- H** Magnetic vector
- D** Electric displacement vector
- J** Current density
- r** Spatial vector
- t Time
- x Displacement
- m Mass
- k Wave vector
- \hat{k} Complex wave vector = $k_1 + ik_2$
- n Refractive index
- \hat{n} Complex refractive index = $n + i\kappa$
- \bar{t} Normalised sample thickness

Greek symbols

- μ Free space magnetic permeability = $4 \times 10^{-7} Hm^{-1}$
- ρ Charge density
- σ Conductivity
- δ skin depth
- ν Frequency
- ω Angular frequency = $2\pi\nu$

λ	Wavelength
ϵ	Dielectric constant
$\hat{\epsilon}$	Complex dielectric constant = $\epsilon_1 + i\epsilon_2$
ω_p	Plasma frequency
ω_{sp}	Surface plasma frequency
ω_0	Resonant frequency
θ	Incident angle

Acronyms

TE	Transverse electric
TM	Transverse magnetic
SPP	Surface plasmon polariton
LSPR	Localised surface plasmon resonance
PV	Photovoltaic
SERS	Surface enhanced Raman scattering
a-Si:H	Hydrogenated amorphous silicon
FP	Fabry-Perot
GM	Guided mode
CIGS	Copper indium gallium selenide

Enhancing solar cells with plasmonic nanovoids

Chapter 1

Introduction

1.1 Motivation and context

The average reader of this thesis will use 10 kilowatt-hours (kWh) of electricity today, part of approximately 195 kWh of primary energy used if you include transport, heating and food production¹ [1]. The number of people in the world at the time of writing this thesis is 6.8 billion, of which about 20% (1.3 billion) don't have access to electricity at all [2, 3]. The demand for electricity is expected to increase in both the developed and developing world and to accommodate this the total production of electricity must also increase. This is a significant technological challenge, but it is not only the total amount that matters but how the electricity is produced.

The world's electricity

Approximately 65% of the world's electricity is generated by burning fossilised hydrocarbons (Fig. 1.1) [4]. A chemical byproduct of this is carbon dioxide (CO₂), which contributes to climate change via the greenhouse effect. There are a number of steps the world can take to address the challenge of CO₂-induced climate change in addition to the concurrent challenges of sustainable development, resource scarcity and environmental stewardship. One technological step is to consider supplementing our current electricity

¹Assuming the reader is warm, well fed and in a country as developed as the UK. The average American uses 250 kWh per day, the average European 125 kWh. Regarding units, this thesis uses SI unless stated otherwise. The kWh is presented as the unit of electricity consumption however, because it is the amount we pay approximately 13p for on our electricity bill.

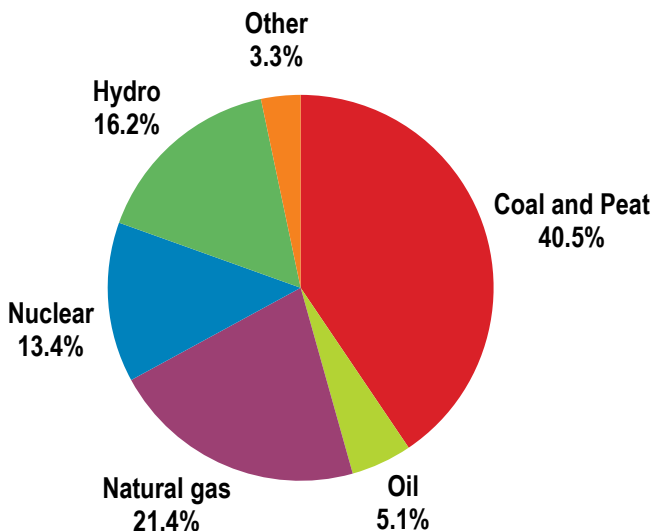


Figure 1.1: World electricity generation by source of energy. ‘Other’ includes wind, solar, geothermal and biofuels. From the OECD i-library [4].

production with alternative methods that do not require the mining and burning of fossilised hydrocarbons. Within this there are a wide range of options including wind, hydro, tidal, geothermal, nuclear and solar, and each are expected to form a part of the energy future [5].

The key metric and figure of merit for an electricity-generation technology is its cost, most often calculated as the levelised cost of electricity (LCOE). This is the cost of generating electricity calculated at the point of connection to the grid, and whilst dependent on social and political factors [6, 7], it serves as an initial measure of the present economic viability of each technology.

The levelised costs of electricity predicted for electricity plants entering service in the USA in 2016 are represented in Table 1.1. All of these technologies, with the exception of solar photovoltaics (PV), generate electricity by turning magnets inside conducting coils, which leads to the remarkable consideration that 99% of the world’s electricity arises from the understanding and application of Faraday’s Law of Induction: $\nabla \times \mathbf{E} = -\frac{\partial \mathbf{B}}{\partial t}$. It is a robust, well-understood technology that has had steady, though incremental, increases in rotation-to-electricity conversion efficiencies through careful

Plant type	LCOE (c/kWh)
Gas	6.6
Hydro	8.6
Coal	9.5
Wind - Onshore	9.7
Geothermal	10.2
Biomass	11.3
Nuclear	11.4
Coal with CCS	13.6
Solar PV	21.1
Wind - Offshore	24.3
Solar Thermal	31.2

Table 1.1: Estimated levelised cost of electricity (LCOE) for plants entering service in 2016. From the US Department of Energy [8].

engineering design for well over a century.

Photovoltaics

The only major generation technique that is not an application of Faraday’s Law is photovoltaics, which instead directly converts light into electricity via photovoltaic cells. It is a younger technology with significant scope for improvement in energy-conversion efficiency through basic scientific research. The current world record efficiency for a solar cell converting sunlight to electricity at the earth’s surface is 42 % [9] and is much lower than the theoretical limit of 85 % [10], discussed further in Chapter 2. Understanding the physical processes of light-matter interactions within solar cells provides an opportunity to significantly raise the position of solar photovoltaics’ LCOE in Table 1.1.

Solar cells have the additional property of being both portable and capable of providing decentralised electricity in remote areas. This is currently allowing the transformation of remote communities in the Australian outback and across the developing world by providing access to communication, distance learning and the powerful social and political consequences of the information revolution [11].

To research light-matter interactions that are capable of aiding sustainable development, helping increase access to electricity for the 1.3 billion

people in the world currently without it, and doing so in a manner that contributes minimally to climate change - whilst still being an area of rich, colourful and exciting physics - is the motivation for this PhD.

1.2 Plasmonic photovoltaics

Thin solar cells are promising candidates for reducing the cost and increasing the efficiency of solar energy. Thin films use less semiconductor material (often costly and/or rare), have higher manufacturing throughputs and offer electrical advantages due to increased fields within the device. Shorter cell thicknesses also demand less of the electrical properties of the semiconductor material, allowing the use of novel materials as absorbing layers.

Opposing the shift towards thin cells is the necessity of large *optical* thicknesses to efficiently harvest the full solar spectrum. As cell thicknesses reduce from the micron length scale (used for crystalline silicon), towards the range of tens to hundreds of nanometres (typical for thin-film devices), light can no longer be approximated in the ray-optics regime and must be considered as a wave. In this regime, traditional absorption enhancement techniques such as anti-reflective coatings and surface texturing are no longer effective: dielectric materials with thicknesses less than the wavelength of light instead contribute to an effective refractive index.

One mechanism for coupling light into thin layers is the use of plasmonics. By careful design of coinage metals (Ag, Au, Cu), structures can be fabricated with high scattering cross-sections and strong near-field localisations of light through the excitation of plasmonic resonances.

A plasmon is defined as a quantum of collective charge excitation in an electron gas [12, 13]. More intuitively, they are a way in which free electrons in a metal respond to incident light, oscillating against a backdrop of fixed positive ions. Plasmons can be excited in the volume of a conductor (volume plasmons), on the surface between a conductor and a dielectric material (surface plasmons), or locally across metallic nanostructures (localised plasmons).

Following the initial work of Stuart and Hall [14], the main research effort in plasmonic photovoltaics has investigated the plasmonic scattering resonances of metal nanoparticles to increase light absorption in thin solar cells

[15, 16].

Recently it has been shown that similar resonances occur in metallic *voids*; just as metallic nanoparticles surrounded by a dielectric experience plasmonic interaction with incident light, so too do dielectric ‘inverse’ particles in metallic media: metal nanovoids [17–19]. Substrates of such metallic nanovoids have recently been harnessed for use in surface-enhanced Raman spectroscopy (SERS) [18–22]. This thesis investigates the application of metallic nanovoids for enhancing solar cell efficiency (Fig. 1.2).

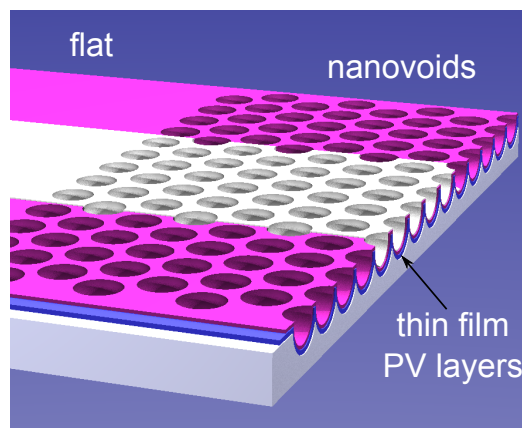


Figure 1.2: Schematic representation of solar cells fabricated on plasmonic nanovoids. Individual void diameters are typically 100 - 1000 nm.

Plasmonic substrates have similar advantages to plasmonic-particles for enhancing solar cells but are additionally able to act as the cell bottom contact. This feature is especially useful in allowing enhanced absorption to occur in close proximity to the region of charge-carrier extraction.

We first investigate organic solar cells fabricated on nanovoids, showing a four-fold enhancement in efficiency compared to flat cells. Theoretical modelling enables identification of localised plasmon resonances and suggests a possible route towards third generation plasmonic photovoltaics. We next demonstrate a 20% enhancement of efficiency for amorphous silicon solar cells in nanovoids compared to flat, but find that with careful optimisation of the spacer layer, randomly textured silver allows for an even greater enhancement of up to 50%. We examine the differences between the two substrates and investigate the dependence of plasmonic near-field enhancement on semiconductor material, curvature and the spacer layer. From this research we demonstrate clear design principles for plasmonic-enhanced photovoltaics.

1.3 Thesis layout

Chapter 2 presents an introduction to the background theory of plasmonics (Section 2.1) and photovoltaics (Section 2.2), with a summary of relevant length scales in Section 2.3.1. Chapter 3 reviews the literature of plasmonic photovoltaics in two subsections, 3.1 and 3.2, reviewing particle plasmonic and surface plasmonic photovoltaics respectively.

Chapter 4 presents the experimental techniques of nanovoid and solar cell fabrication and discusses the factors involved in plasmonic PV design. Chapter 5 outlines the optical and electronic characterisation techniques with which we measure photovoltaic performance alongside methods of theoretical simulation. Chapter 6 presents plasmon-enhanced organic solar cells fabricated on nanovoids. Chapter 7 presents plasmon-enhanced amorphous silicon solar cells fabricated on nanovoids and randomly textured glass and discusses the mechanisms for coupling to optical modes within each device. Chapter 8 analytically derives the balance of absorption between a metal and a semiconductor with a surface plasmon excited at the interface and discusses this ratio for a wide range of photovoltaic materials. The thesis concludes with a discussion of practical design principles for plasmonic-enhanced photovoltaics, and outlines future directions of research.

Chapter 2

Background theory

This chapter reviews the background theory relevant to this project. Section 2.1 reviews the theoretical description of plasmons, starting with Maxwell's equations and continuing to the derivation of the surface plasmon dispersion relation. The section concludes with a review of localised plasmons in particles and voids and an introduction to the theoretical modelling of nanostructured surfaces.

Section 2.2 reviews the physics of photovoltaics, including an outline of band-gap diagrams, the solar cell equation and a discussion of charge transport in semiconductor materials. Section 2.3 summarises plasmonic photovoltaics and the physics related to relevant length scales, optical interactions in thin films and material absorption considerations.

2.1 Plasmonics

Plasmonics is a wave-optics phenomenon arising from the structuring of metal on the nanoscale, and it is precisely for this reason that plasmonic light-trapping can be achieved in thin solar cells. For solar cells with sub-wavelength thicknesses, traditional light trapping mechanisms based on the ray-optics picture of light are ineffective. With the inclusion of plasmonic structures, light may be both concentrated in the near-field or scattered to a broad range of optical modes in thin films. This section briefly reviews the initial theoretical description of plasmons.

2.1.1 Overview

Plasmonic phenomena have been witnessed since at least the 4th century AD when stained glass such as the Lycurgus cup was found to display the plasmonic properties of gold and silver nanoparticles - showing green in reflection, but red in transmission. This technique of colouring glass was used throughout Europe in later centuries, including for the original glass windows of the Notre Dame Cathedral in Paris (Fig. 2.1) [23].

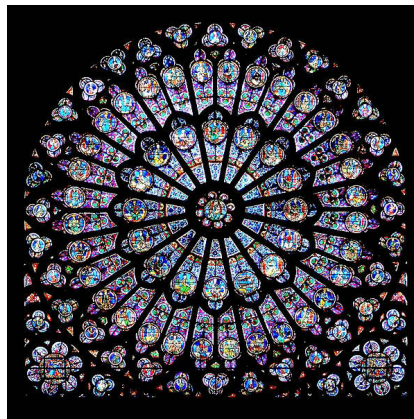


Figure 2.1: Gothic rose window of Notre-Dame cathedral in Paris. The original windows of the cathedral contained red and green glasses, coloured by the plasmonic properties of silver and gold nanoparticles. Figure from [23].

In a scientific context, plasmonic behaviour was first identified from the anomalous diffraction of light from a grating by Wood in 1935 [24]. The initial theoretical understanding of plasmonics is attributed to the work of Mie [25] and Ritchie [26] through the 20th century. A plasmon is a quantum of coupled excitation between free electrons in a metal and an incident electric field. A more intuitive description is that of a coupled resonance of electrons to light; a way in which conduction electrons in a metal respond to incident light by oscillating against the background of fixed positive metallic ions. Detailed analysis of the present theory of plasmonics can be found in references [27] and [28] and in the texts by Raether [29] and Maier [12].

2.1.2 Electromagnetics of metals

The optics of plasmonic interactions within metals is understood through the framework of classical electromagnetism, that of Maxwell's equations:

$$\nabla \cdot \mathbf{D} = \rho_{ext} \quad (2.1)$$

$$\nabla \cdot \mathbf{B} = 0 \quad (2.2)$$

$$\nabla \times \mathbf{E} = -\frac{\partial \mathbf{B}}{\partial t} \quad (2.3)$$

$$\nabla \times \mathbf{H} = \mathbf{J}_{ext} + \frac{\partial \mathbf{D}}{\partial t} \quad (2.4)$$

Here charge and current densities are distinguished between external $(\rho_{ext}, \mathbf{J}_{ext})$ and internal (ρ, \mathbf{J}) so that $\rho_{tot} = \rho_{ext} + \rho$ and $\mathbf{J}_{tot} = \mathbf{J}_{ext} + \mathbf{J}$. These are the macroscopic Maxwell equations and are further linked through:

$$\mathbf{D} = \epsilon_0 \mathbf{E} + \mathbf{P} \quad (2.5)$$

$$\mathbf{H} = \frac{1}{\mu_0} \mathbf{B} - \mathbf{M} \quad (2.6)$$

Where \mathbf{P} and \mathbf{M} are the polarisation and magnetisation of the material respectively. In linear, isotropic and nonmagnetic materials, those which this work mainly considers, the following relationships are defined:

$$\mathbf{D} = \epsilon_0 \tilde{\epsilon}_r \mathbf{E} \quad (2.7)$$

$$\mathbf{B} = \mu_0 \tilde{\mu}_r \mathbf{H} \quad (2.8)$$

Here ϵ_r and μ_r are the relative dielectric and permeability functions of the material, with $\mu_r = 1$ for nonmagnetic materials.

Combining equations 2.3 and 2.4 with recognition of the Fourier transforms: $\nabla \rightarrow i\mathbf{k}$, $\frac{\partial}{\partial t} \rightarrow -i\omega$, with wavevector \mathbf{k} , and frequency ω , and assuming an homogenous medium with no external stimuli $(\rho_{ext}, \mathbf{J}_{ext} = 0)$, we arrive at the fundamental expression between the relative dielectric function $\tilde{\epsilon}_r$ and conductivity [30]:

$$\tilde{\epsilon}_r = 1 + \frac{i\tilde{\sigma}}{\epsilon_0\omega} \quad (2.9)$$

The dielectric function and conductivity are in general both complex: $\tilde{\epsilon}_r = \epsilon_1 + i\epsilon_2$ and $\tilde{\sigma} = \sigma_1 + i\sigma_2$. The index of refraction \tilde{n} is defined $\tilde{n} = \sqrt{\tilde{\epsilon}_r}$,

and is also separated into its real and imaginary parts: $\tilde{n} = n + i\kappa$. These are related to the dielectric function by:

$$\epsilon_1 = n^2 - \kappa^2 \quad (2.10)$$

$$\epsilon_2 = 2n\kappa \quad (2.11)$$

The experimental quantity that can be directly measured for the dielectric function is the absorption coefficient (α): the rate at which light intensity decays as it passes through a material.

$$\alpha = \frac{2\omega}{c}\kappa \quad (2.12)$$

2.1.3 The Drude model

The dielectric function ($\tilde{\epsilon}_r$) expresses the defining optical features of a material. The plasma model of a metal, the basis of the Drude model, is that of a sea of electrons moving against a background of positive ion cores. In general, $\tilde{\epsilon}_r$ is a function of both wavevector and frequency, however we assume the characteristic dimensions of the material are much smaller than the wavelengths of incident light, and neglect the wavevector dependence. We then consider the oscillatory response of the electron gas to an incident electromagnetic wave $\mathbf{E}(t) = \mathbf{E}_0 e^{-i\omega t}$ with frequency ω .

The response can be understood through classical mechanics. The equation of motion in one dimension is written for an electron in an external electric field:

$$m^* \ddot{\mathbf{x}} + m^* \gamma \dot{\mathbf{x}} = -e\mathbf{E} \quad (2.13)$$

Here m^* is an approximation of the effective mass of each electron incorporating the effects of the lattice potential and electron-electron interactions alongside γ the characteristic damping term. Considering a harmonic incident electric field $E_0 e^{-i\omega t}$ with frequency ω , and assuming an oscillatory electron response $x_0 e^{-i\omega t}$, we can write: $\mathbf{x} = -\frac{e}{m^*(\omega^2 + i\gamma\omega)}\mathbf{E}$. Combining Equations 2.7 and 2.5 for a linear medium, and with $\mathbf{P} = -n_e e\mathbf{x}$, where n_e is the electron density, we arrive at the following expression of the dielectric function [12]:

$$\tilde{\epsilon}_r = 1 - \frac{\omega_p^2}{\omega^2 + i\gamma\omega} \quad (2.14)$$

2. Background theory

This is the central result for the dielectric function of the Drude Model. The plasma frequency ω_p is defined $\omega_p^2 \equiv \frac{ne^2}{m^*\epsilon_0}$; it represents the resonant frequency of the nearly free electron gas in a metal under an incident oscillating electromagnetic field.

The real and complex parts of Equation 2.14 can be identified via reflectivity and absorption studies of a real metal, and the real and imaginary parts of the dielectric constants are presented in Figure 2.2.

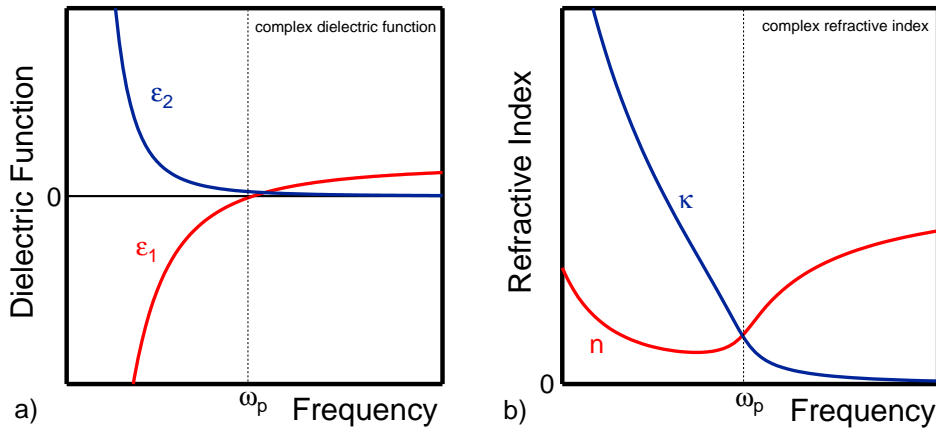


Figure 2.2: Graphs of the real and imaginary parts of the dielectric function $\tilde{\epsilon}_m$ and refractive index \tilde{n}_m versus frequency, for a Drude model metal. Typical values for fit constants are $\omega_p \sim 10^{15}$ Hz and $\gamma \sim 10^{14}$ Hz.

The Drude free-electron model provides an excellent basis for understanding the optical response of electrons in a metal. It fails, however, at the onset of interband electron transitions of metals that occur as frequency increases. Figure 2.3 presents a comparison of the Drude model theory versus experimental data of the real and imaginary dielectric functions of gold.

Discrepancies between theory and experiment in Figure 2.3 can be addressed by including an additional bound-electron term in Equation 2.13 [12]. With an understanding of the dielectric function we can examine the physics of light and electron interactions at the surface between a dielectric and a metal.

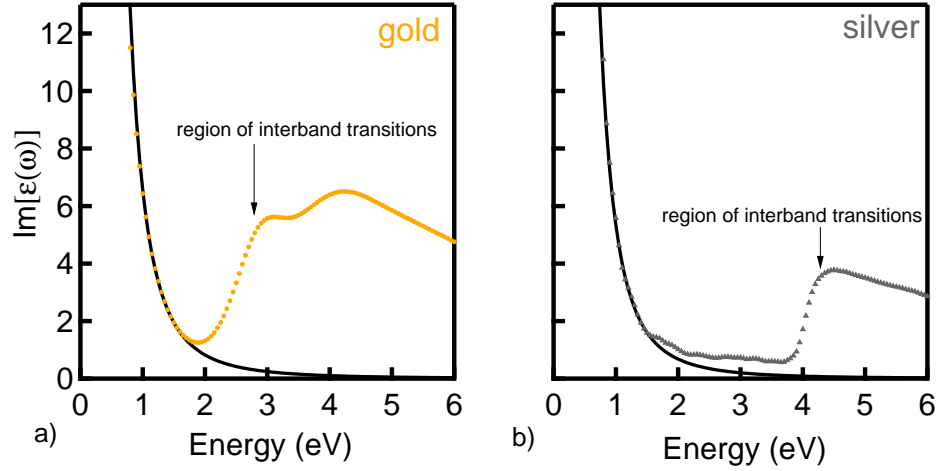


Figure 2.3: The imaginary parts of the dielectric function (ϵ_2) of gold (a) and silver (b) compared with Drude-model fits. The onset of interband transitions can be observed at 2.5 eV for gold and 4 eV for silver. Dots are experimental values from Palik [31].

2.1.4 Surface plasmon polaritons

Applying Maxwell's Equations to the surface between a dielectric and a metal leads to interesting phenomena. For a non-absorbing dielectric with real dielectric constant $\epsilon_d > 0$ and an adjacent conducting metal with $\text{Re}(\tilde{\epsilon}_m) < 0$, we arrive at two sets of solutions for waves propagating along the interface: those for transverse magnetic (TM) and transverse electric (TE) polarisations. Applying boundary conditions at the surface shows that surface-bound modes exist only for TM polarisations of the incident electromagnetic wave with the following conditions [12]:

$$\begin{aligned} \frac{\partial^2 H_y}{\partial z^2} + \left(\frac{\omega^2}{c^2} \tilde{\epsilon} - \tilde{k}_x^2 \right) H_y &= 0 \\ E_x &= -i \frac{1}{\omega \epsilon_0 \tilde{\epsilon}} \frac{\partial H_y}{\partial z} \\ E_z &= i \frac{\tilde{k}_x}{\omega \epsilon_0 \tilde{\epsilon}} H_y \end{aligned} \quad (2.15)$$

Here ω is the angular frequency of incident light in vacuum and \tilde{k}_x the

2. Background theory

wave vector of the propagating wave in the x direction:

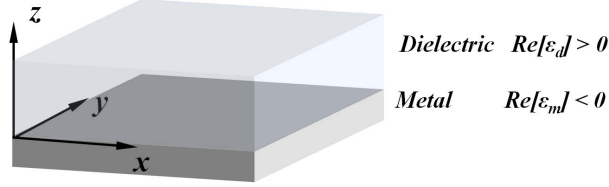


Figure 2.4: Geometry for surface plasmon polariton propagation at the interface between a metal and dielectric.

Continuity of \mathbf{B} at the interface yields $\frac{\tilde{k}_{z,d}}{\tilde{k}_{z,m}} = -\frac{\tilde{\epsilon}_d}{\tilde{\epsilon}_m}$, and we arrive at the dispersion relation for a transverse magnetic electromagnetic wave with wavevector $\tilde{k}_{x,spp}$ propagating along the surface of the metal/dielectric interface [29].

$$\tilde{k}_{x,spp} = \frac{\omega}{c} \sqrt{\frac{\tilde{\epsilon}_m \tilde{\epsilon}_d}{\tilde{\epsilon}_m + \tilde{\epsilon}_d}} \quad (2.16)$$

Plotting frequency versus the real part of \tilde{k}_x (Fig. 2.5), shows two salient features of the coupled electromagnetic wave at the interface, named the surface plasmon polariton SPP (Surface Plasmon Polariton). The first feature is that the real part of \tilde{k}_{spp} lies to the right of the light line. That is, the momentum of the coupled surface plasmon polariton ($\hbar k_{spp}$) is always greater than the momentum of a free photon ($\hbar k_0$) travelling parallel to the flat surface with the same frequency ω .

The second feature to note is the asymptotic behaviour of $\text{Re}(\tilde{k}_{spp})$ for large in-plane wave vector k . As k increases, $\text{Re}(\tilde{k}_{spp})$ tends to a value of $\frac{\omega_p}{\sqrt{1+\epsilon_d}}$. In this limit, $\frac{d\omega}{dk}$ tends to zero, and the surface plasmon polariton becomes electrostatic in nature. Approaching this limit, the SPP is now referred to simply as a surface plasmon. The surface plasmon frequency is then $\frac{\omega_p}{\sqrt{1+\epsilon_d}}$, known as the Ritchie frequency [27].

A physical analogy of surface plasmon polaritons can be thought of as a lattice of charged particles connected with springs. Upon oscillatory driving, a response of the particles is induced with a collective natural resonance. As the charged particles oscillate at their natural frequency they set up a standing wave of electromagnetic field (Fig. 2.6).

We can see how surface plasmons are ‘tethered’ to the interface of the dielectric and metal with intensity of the SPP field amplitude decreasing as

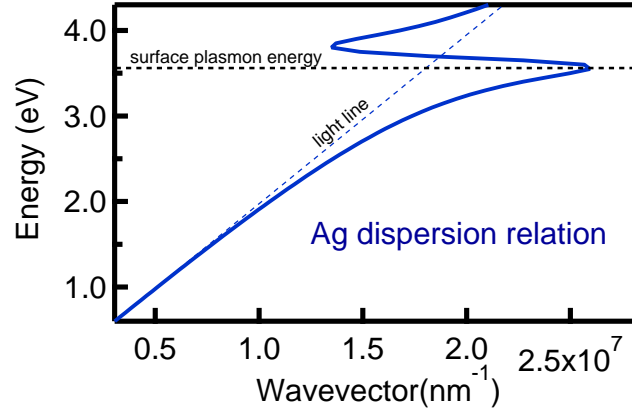


Figure 2.5: Graph of the dispersion relation found by taking the real part of Equation 2.16. The metal dielectric function is the Drude model approximation for silver, and the diagonal line is the dispersion line for light with gradient c .

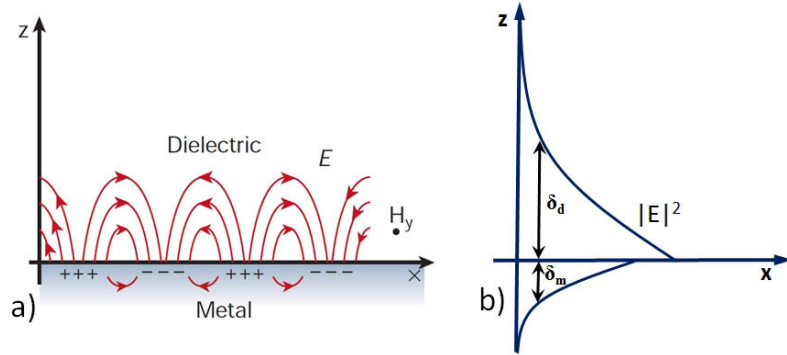


Figure 2.6: a) Schematic diagram of a surface plasmon coupled at the interface of a metal and a dielectric, from Barnes 2003 [32]. b) Length scales for the exponential decay of the plasmonic field into both the metal and dielectric.

$e^{-|k_{z,i}||z|}$. The natural decay lengths are hence $\delta_i = \frac{1}{|k_{z,i}|}$ for both the dielectric and metal, and are given by the following expressions [29]:

$$\begin{aligned}\delta_d &= \frac{\lambda}{2\pi} \left(\frac{\text{Re}[\epsilon_m] + \epsilon_d}{\epsilon_d^2} \right)^{\frac{1}{2}} \\ \delta_m &= \frac{\lambda}{2\pi} \left(\frac{\text{Re}[\epsilon_m] + \epsilon_d}{(\text{Re}[\epsilon_m])^2} \right)^{\frac{1}{2}}\end{aligned}\quad (2.17)$$

For incident light at $\lambda = 600$ nm on a silver/air interface $\delta_{air} = 390$ nm and $\delta_{Ag} = 24$ nm, [29], for gold: $\delta_{air} = 280$ nm and $\delta_{Au} = 31$ nm. Surface plasmons also decay in-plane *along* the interface between the dielectric and

metal. The intensity decreases as $e^{-2\text{Im}[k_x]x}$, with decay length $L = \frac{1}{\text{Im}[k_x]}$. At 600 nm the propagation length is 10 μm at a gold/air interface and 100 μm for silver and air.

These length scales and their implications for plasmonic photovoltaics are further discussed in Section 2.3.1.

2.1.5 Localised surface plasmons

The plasmons depicted in Figure 2.6 are surface plasmons occurring on a flat semi-infinite metal surface. Now consider curving the metal surface into a closed particle with size on the order of the wavelength of the incident light. Since the resulting circumference is much less than the propagation length, surface plasmon polaritons excited on the surface interact with themselves to create distinct resonant modes. The simplest modes to theoretically consider are those for spherical particles. The full treatment is given by Mie theory which analyses the different eigenmodes of the electromagnetic field and expands them into their spherical harmonic contributions [25]. For particles with diameter much less than the wavelength of light, the phase of the incident wave can be modelled as constant over the nanosphere, leading to stationary resonant modes of polarisation. In this limit they are known as localised surface plasmon polaritons, and can be described with a point-dipole model. Using this model Bohren and Huffman [33] calculate the scattering and absorption cross sections of metal nanoparticles to be:

$$C_{scat} = \frac{1}{6\pi} \left(\frac{2\pi}{\lambda} \right)^4 |\alpha|^2, C_{abs} = \frac{2\pi}{\lambda} \text{Im}[\alpha] \quad (2.18)$$

Here, α is the polarisability of the particle and is given in the quasi-static limit by:

$$\alpha = 3V \left[\frac{\epsilon_p - \epsilon_d}{\epsilon_p + 2\epsilon_d} \right] \quad (2.19)$$

V is the volume of the particle, ϵ_p is the real part of the dielectric function of the particle and ϵ_d the dielectric function of the surrounding medium; this approximation is valid for particles with diameter $d \ll \lambda$. From equation (2.19) we can observe what is known as the surface plasmon resonance or Frölich condition; when ϵ_p approaches $-2\epsilon_d$, the polarisability becomes very large, in turn leading to large scattering and absorption cross sections. For a

spherical silver particle with diameter 100 nm the ratio of albedo: $\frac{C_{scat}}{C_{abs}+C_{scat}}$ is approximately 0.9 at visible wavelengths [16]. As an aside, dielectric nanoparticles have similarly high albedo and have found use in a wide range of light scattering applications, from solar cells to paints and sunscreens. Whilst still of active research interest, their scattering cross-sections are typically one to two orders of magnitude lower than plasmonic nanoparticles.

The plasmonic resonances of metal nanoparticles are currently being harnessed for application to solar cells - they are regularly deposited on solar cell surfaces to enhance absorption within the underlying material, further discussed in Section 3.1.

A similar approach to that of Mie can be applied to nano-voids. By making the substitution $\epsilon_p \leftrightarrow \epsilon_d$, the theoretical prediction of plasmonic resonances in spherical nanovoids can be made. In general, the Mie resonances of voids correspond to particle resonances of smaller diameter due to the field profile of voids being located more in the void than in the metal.

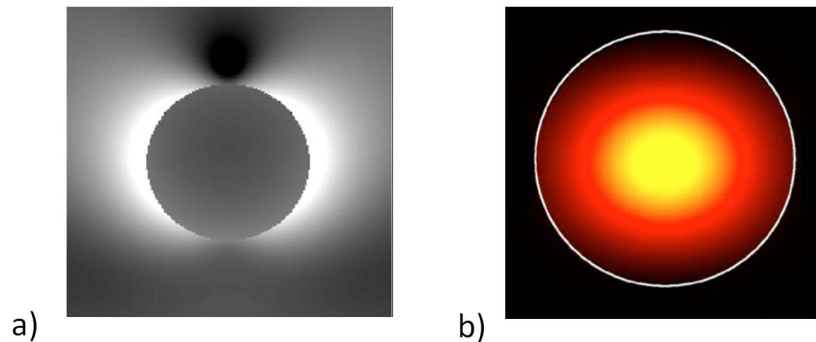


Figure 2.7: a) Boundary-element method simulation of a spherical silver nanoparticle of 100 nm radius. A factor of five enhancement of the $|E|^2$ intensity is found near the surface of the particles. b) Calculated Mie theory of the $(l,m)=(1,1)$ resonance of a sphere of air in a gold medium, from[20].

Analytical solutions can be found for particles and voids of regular shape. Beyond these few geometrically tractable solutions, computer modelling is employed to obtain an understanding of plasmonic resonant modes. Theoretical modelling is further discussed in Chapter 5, but we include here a graphical representation of field enhancements for a nanoparticle (Fig. 2.7a) and spherical metal void (Fig. 2.7b).

Just as plasmon resonances occur for non-spherical particles, they simi-

larly occur for non-spherical voids. In 2001 Coyle *et al.* demonstrated a technique for fabricating patterned gold surfaces with near-spherical nanovoid metallic cavities [18]. These cavities can be made with different diameters and scalable heights to create nano dimples, cups and cavities that exhibit strong plasmonic resonances.

A musical analogy of nanovoid plasmons can be found in Buddhist singing bowls (Fig. 2.8). Used by monks in the mountains of Nepal and Tibet as an aid to meditation, singing bowls resonate a beautiful musical tone when circularly driven by a wooden rod¹. This resonance is purely mechanical, but a similar effect is found with light for structures approximately 100,000 times smaller - localised plasmons in nanovoids.



Figure 2.8: A Buddhist singing bowl as a musical analogy of nanovoid plasmonic resonance¹.

Nanovoids can be made in a controlled, reproducible fashion [34] and have shown remarkable coupling to plasmon resonances [19, 20, 22]. Plasmonic responses of these and other cavity structures have been studied extensively within our group; reviews of the work in spherical voids can be found in Kelf *et al.* (2006) [20] and Cole *et al.* (2007) [22].

Techniques for fabricating nanovoid structures are discussed further in Chapter 4 and the analysis of plasmon modes is outlined in Chapter 5. Here we introduce plasmonic mode mixing.

In Figure 2.10 we see coupling to two different plasmon modes. In (a) we observe delocalised, propagating surface plasmons referred to as ‘Bragg’ modes. Here the array of shallow nanovoids act as a 2D grating which provides the additional momentum $n\mathbf{G}$ for incident light to couple to propagating surface plasmon modes, with n an integer and $\mathbf{G} = \frac{2\pi}{a}$ with a the period of the grating. Hence light at incident angle θ_{in} can couple to the surface

¹A physical demonstration of a singing bowl can be seen at purl.org/nnl/singingbowlplasmons

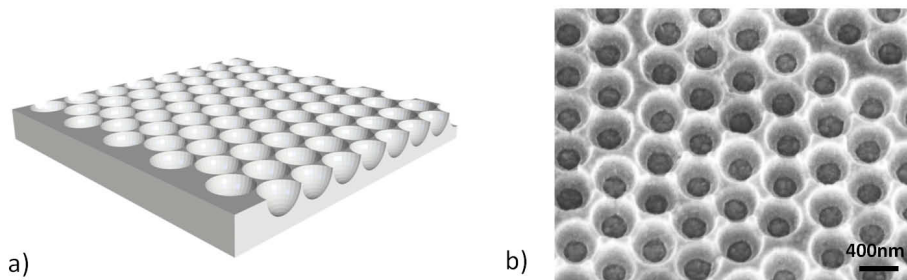


Figure 2.9: a) Schematic and b) scanning-electron microscope image of silver nanovoids of 400 nm grown to ‘half-height’.

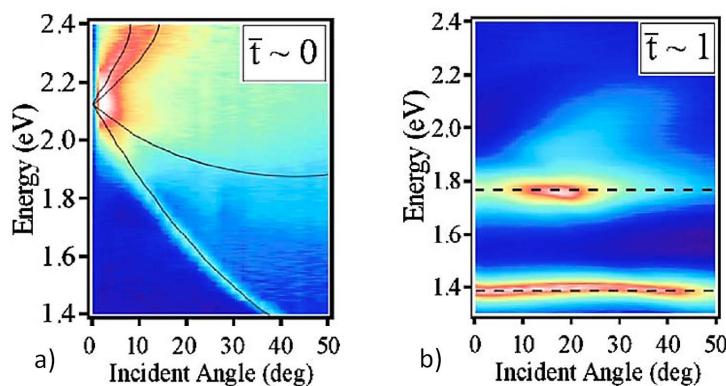


Figure 2.10: Angularly resolved reflectivity spectra of shallow spherical gold dishes (height \sim 0) (a), and fully enclosed spherical voids (b), from [20]. \tilde{t} refers to the ratio of metal height to void diameter t/d . Reflectance is normalised to flat gold, with blue indicating 0% plasmon absorption, and white indicating 80% plasmon absorption. The black lines in (a) indicate theoretical dispersion lines for Bragg scattering, those in (b) are theoretically calculated localised Mie plasmon modes.

plasmon polariton with wavevector $\mathbf{k}_{\text{spp}} = \mathbf{k}_0 \sin(\theta_{in}) + n\mathbf{G}$.

In Figure 2.10(b) the surface plasmon propagating around the nanovoid structure sets up resonant localised plasmonic modes similar to the localised modes for a metal particle surrounded by air. Using Mie theory and exchanging the dielectric functions $\epsilon_p \leftrightarrow \epsilon_d$ between the particle and surrounding dielectric, we arrive at the localised plasmonic modes for fully encapsulated metal nanovoids, shown by the black lines of Figure 2.10(b).

For real nanovoid structures with height between flat and fully enclosed, plasmonic resonances are mixed between the Bragg and Mie modes of Figure 2.10, and with modes that occur on the rim. Mode mixing is further discussed in references [20, 22, 35]. A graphical representation of plasmonic modes in

non-encapsulated void structures can be seen in Figure 2.11 with larger than $10\times$ field enhancements in distinct regions within the cavity.

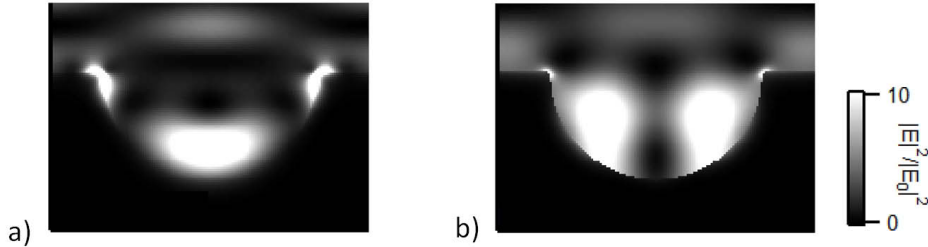


Figure 2.11: Spatial intensity distributions of plasmonic electric field enhancements at 3.3 eV (a) and 2.5 eV (b) in spherical silver nanovoids surrounded by a non-absorbing dielectric. Nanovoid plasmonic solar cells are placed on top of these silver structures, harnessing the electric field enhancements to increase light absorption, charge separation and carrier extraction.

Nanovoid surfaces have found application in surface-enhanced Raman spectroscopy (SERS) [21, 36] in which nano-scale field enhancements have been channeled to molecules lying above the substrate to increase their Raman scattering signal (of up to an order of 10^7). It is these field enhancements of metallic nanovoids which this project investigates for application to thin-film solar cells, finding strong enhancement of efficiency for both organic and amorphous silicon solar cells. The project continued to explore both near-field and scattering properties of various plasmonic substrates in addition to the effect of varying spacer layer thicknesses within devices; the results highlight key physical principles for optimal plasmonic photovoltaics.

2.2 Photovoltaics

Background

The photovoltaic effect was discovered in 1839 by the French scientist Edmond Becquerel who discovered that a platinum sheet covered in silver chloride generated electricity when light was shone upon it [37]. It took more than a century from Becquerel's discovery until the fabrication of the first commercially viable solar cell in 1956 when Chapin, Fuller and Pearson demonstrated a 6% efficient silicon solar cell with a p-n junction structure [38]. The cell still forms the basis of modern photovoltaics - more than 80% of the solar cell market today is dominated by silicon p-n diode devices. The industry itself is growing exponentially with world wide solar cell production reaching 24 GW in 2010-11 (Fig. 2.12).

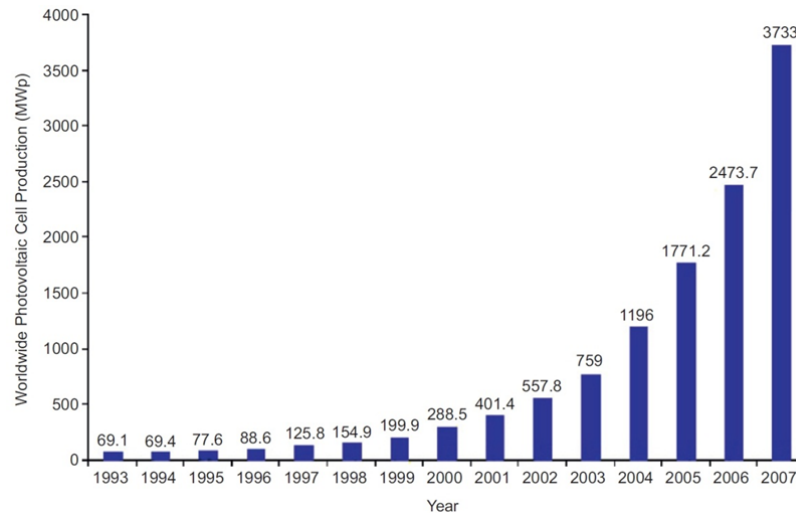


Figure 2.12: Growth of world wide solar cell production [39]. In 2010-11, cell production was 24 GWp [40], a six-fold increase on 2007. For reference a standard coal-fired power plant generates approximately 300 MW of power.

Solar cell physics is an area of rich scientific enquiry with novel materials and device structures proposed regularly. Reviews of the steady growth in the number of these materials and device designs can be found in references [39, 41] and [42]. A detailed review of the future possible directions of photovoltaics is provided in Martin Green's book *Third Generation Photovoltaics* [45]. The different generations of photovoltaics refer to device structure and maximum limits of efficiency. First generation cells are those based

on crystalline semiconductor structures, limited in efficiency to the Shockley-Queisser limit of 31% under normal sunlight [46]. Second generation solar cells are grouped as thin-film devices which can be produced for less cost than first-generation solar cells. Organic and amorphous silicon solar cells belong to this generation. Third generation solar cells are defined as those that move away from the standard single p-n junction structure and instead are limited only by the Carnot efficiency limit for solar energy conversion - the ‘Müser’ engine limit at 85.4% [10]. Examples include multijunction-cells, thermophotovoltaics, thermophotonics and hot-carrier solar cells [45].

The first applications of plasmonic-enhancement to solar cells have occurred for first and second generation devices. Later in this thesis we propose a possible mechanism of plasmonic wavelength-selective light-trapping for third-generation devices (Chapter 8). Here we briefly examine the physics behind solar cell operation, beginning first with the solar cell equation and Fermi-level matching that is common to all solar cell devices and materials, before discussing charge transport in different semiconductor materials.

2.2.1 Energy-level diagrams

The basis for solar cell operation is the connection of a semiconducting material to another material (either conducting or semiconducting) with different internal energy levels. Where the two materials connect, an electric field is set up between them. When light of sufficient energy is absorbed by the structure, charge-carriers are excited, separated due to the electric field and transported to opposite contacts of the cell where they can be used in an external circuit. This description is true for all solar cell materials and designs, though the electric field origin and nature of charge transport differs across materials.

The physics is perhaps most intuitively seen for solar cells designed with p and n -type inorganic crystalline semiconductors (Fig. 2.13). If we consider bringing an n and p type semiconductor into contact (an artificial situation, though it serves as a basis of understanding), majority carriers swim across the interface leaving behind ‘naked’ fixed charges that give rise to the electric field in what is known as the ‘depletion region’. The field across the depletion region is the basis of the rectifying barrier of the p-n diode [47] and charge

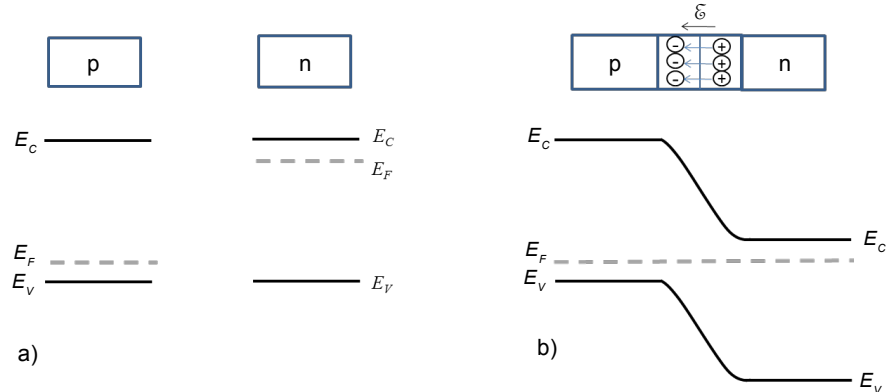


Figure 2.13: (a) *p*-type and *n*-type semiconductors before electrical contact. (b) Energy diagram of the connected p-n junction. E_V and E_C refer to the valance and conduction energy levels, respectively. E_F is the Fermi level.

separation in an inorganic crystalline solar cell device [47].

Similar bending of the conduction and valence bands occur at the interface between a semiconductor and metal. The direction of band-bending is caused by the relative positions of the Fermi levels, and gives rise to either blocking or non-blocking ohmic contacts (Fig. 2.14).

It should be stressed that Figures 2.13 and 2.14 are for crystalline semiconductor devices and are included to provide an intuitive description of the energy structures that give rise to solar cell operation. For organic solar cell materials the concept of definite energy bands is not as applicable, and charge transport does not occur in the same manner, discussed further below.

For a silicon solar cell, the built-in potential is typically $\sim 0.7\text{V}$ with a depletion region width of the order of hundreds of nanometres. The interested reader is referred to the texts of Kittel [13], Nelson [48] and Sze [47] for a more detailed analysis of semiconductor junctions and charge-transport physics.

2.2.2 Solar cell equation

When light is incident on a working photovoltaic cell connected to an external circuit, a current is present. For zero load, this current per cross-sectional unit area is known as the short-circuit current density J_{sc} with conventional units of A/cm^2 . The average number of carriers externally collected per incident photon is known as the external quantum efficiency (EQE) - it is the key measure of the spectral response of a solar cell. The equation gov-

2. Background theory

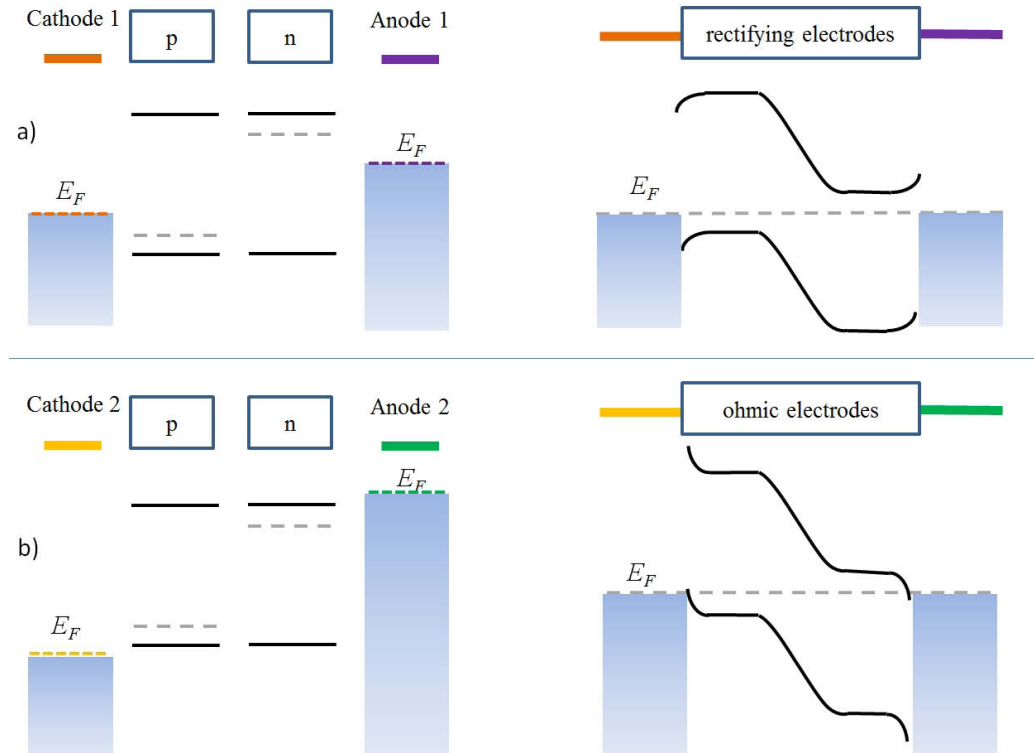


Figure 2.14: Diagram for a p-n junction device with rectifying (a) and ohmic (b) contacts. The direction of band-bending is set by the relative positions of the Fermi levels before contact. The band-bending structure at the contacts in figure (b) can be exploited for majority carriers in the fabrication of Schottky solar cells.

erning normal photovoltaic cell operation is the sum of the photo-induced current density and recombination current density components. The recombination or diffusion component is dependent on the voltage across the cell, the temperature of the cell, and a quantity known as J_0 , the reverse saturation current density. J_0 is dependent on the charge carrier density, carrier lifetimes and surface characteristics of the cell. Through the application of Poisson's equation and the balancing of drift and diffusion currents at thermal equilibrium, we arrive at the ideal solar cell equation:

$$J = J_0(e^{\frac{qV}{kT}} - 1) - J_{sc} \quad (2.20)$$

The left hand term is the ordinary diode equation governing the diffusion of carriers under forward bias. The right hand term is the current caused by illumination and is directed opposite to the diffusion current. The voltage at which no current flows across the cell is known as the open circuit voltage

V_{oc} .

$$V_{oc} = \frac{kT}{q} \ln \left(\frac{J_{sc}}{J_0} + 1 \right) \quad (2.21)$$

The relationship between voltage and current in a photovoltaic cell can be seen in Figure 2.15.

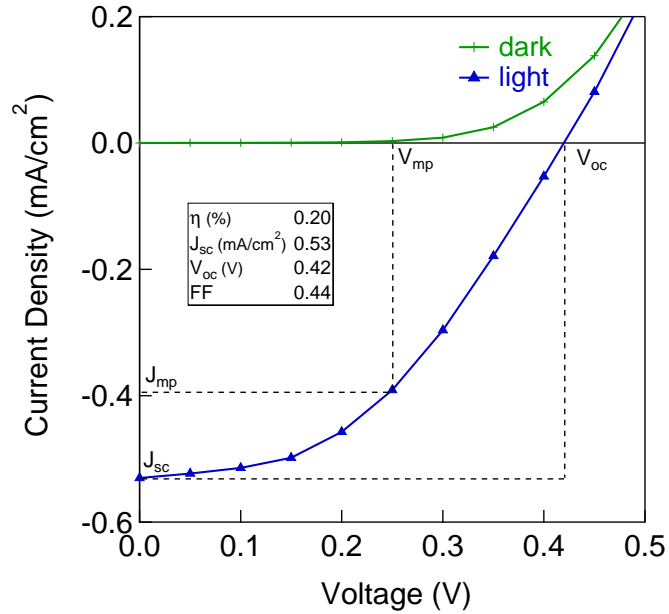


Figure 2.15: Current voltage (J-V) characteristics of an experimental solar cell both in the dark and under normal sunny conditions (0.1 W/cm^2). The fill factor (FF) relates V_{oc} and J_{sc} to the maximum power point (mp) of the cell.

In general, a solar cell will be affected by series resistances across the contacts of the device and shunt resistances that allow charges to recombine before extraction. The maximum power output of the cell is then $V_{mp} \cdot J_{mp}$, which are related to V_{oc} and J_{sc} through the fill-factor: a measure of the ‘squareness’ of the J-V curve shown in Figure 2.15. The fill-factor is dependent on these internal resistances and is calculated:

$$FF = \frac{V_{mp} \cdot J_{mp}}{V_{oc} \cdot J_{sc}} \quad (2.22)$$

The final efficiency of the cell is then given:

$$\begin{aligned}
 \eta_{cell} &= \frac{P_{out}}{P_{in}} & (2.23) \\
 &= \frac{V_{mp} \cdot J_{mp}}{P_{in}} \\
 &= \frac{FF \cdot V_{oc} \cdot J_{sc}}{P_{in}}
 \end{aligned}$$

The relationship between short-circuit current density and open-circuit voltage sets the theoretical limit of efficiency for a single-junction solar cell under normal sunlight to 31 % - the Shockley-Queisser limit [10]. The basis for this limit is the trade-off set by the energy of the band-gap: increasing the band-gap of the semiconductor raises the V_{oc} , but results in decreased J_{sc} since less photons are able to be absorbed from the solar spectrum. Lowering the band-gap allows the absorption of more photons, but decreases the voltage output. The optimum band-gap under normal sunlight is approximately 1.3 eV, while under concentration of sunlight the limit is raised to 41% for a single-junction device of bandgap 1.1 eV. For multi-junction devices and geometries that move away from a single band-gap, the limit is the Carnot limit for solar energy conversion at the earth's surface of 85 % [10] - the aim of third generation photovoltaics [45].

2.2.3 Charge transport

Charge carriers in crystalline inorganic semiconductors fill available states up to a Fermi level that rests between distinct conduction and valence bands. The same statement is not as precise for charge carriers in non-crystalline semiconductor materials. This section briefly outlines the nature of charge transport in organic and amorphous silicon solar cells - the two materials with which solar cells were made in this project.

2.2.4 Organic semiconductors

Organic semiconductors offer the exciting promise of low-cost wide-scale applications in electronics [49], photonics [50], display technologies [51] and lighting [52]. For electricity generation, organic semiconductors have the potential for large-area roll-to-roll production of solar cells based on inex-

pensive, non-toxic and abundant materials. The record efficiency for organic solar cells has steadily increased over the past decade and currently stands at 10.0% [53]; the understanding of photo-excitation and charge transport in organic semiconductors is still rapidly developing. Charge transport sensitively depends on molecular nanostructure, aggregation, orientation, and packing, alongside preparation and processing conditions. A detailed introduction can be found in the reviews of Hoppe [54], Koster [55], Kippelen [56], and Peumans [57], and in the text by Brabec et al. [58]. Here we briefly review photo-induced charge transfer for conjugated polymer and fullerene blends.

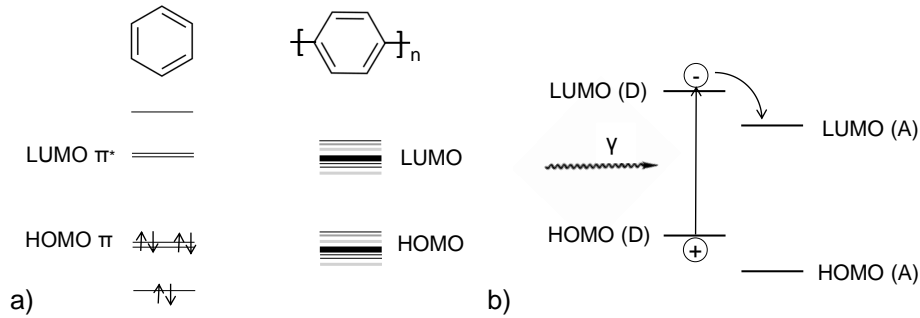


Figure 2.16: (a) Simplified description of the formation of HOMO-LUMO levels in an organic semiconductor. The left diagram refers to an individual monomer unit, whereas the right portrays the energy level picture for the repeating polymer chain. (b) Representation of the photo-induced charge transfer between the donor (D) and acceptor (A) organic polymer. After [54].

The physics behind organic semiconductor charge transfer is based on the overlapping π -orbitals of individual monomers along the polymer chain. The upper and lower energy levels are referred to as the ‘highest occupied molecular orbital’ (HOMO) and ‘lowest unoccupied molecular orbital’ (LUMO) respectively. Overlapping of these orbitals gives rise to bonding and anti-bonding ‘bands’ which are delocalised along the length of the polymer. The HOMO and LUMO are then considered to be analogous to the valence and conduction bands of a crystalline semiconductor (Fig. 2.16a). These bands for organic semiconductors can only be loosely defined; they are representative of the average distribution of energy states across each polymer and are in reality somewhat broader than the corresponding bands for inorganic crystalline semiconductors. In particular the tails of states extend significantly

from the quoted band edges. The values serve as useful terms for energy band diagrams, but must be remembered as being less sharply defined than their inorganic semiconductor analogues.

With the HOMO-LUMO picture, we can see that upon photo-excitation an electron is excited to the LUMO level and a bound electron-hole pair is formed. This charge-carrier pair then diffuses (via a ‘hopping’ style of motion) to the junction between two polymers (in a bulk heterojunction device) or a metal and polymer (in a Schottky barrier device), at which the charges separate due to relative electron affinities (Fig. 2.16b).

Four distinct processes are identified that create photo-current in this cell [54]: 1) photo-excitation of an organic molecule, 2) exciton diffusion to the boundary between hole/electron type semiconductors or the metal electrode, 3) charge separation at the interface, and 4) conduction to the external contact. Non-ideal conditions lead to efficiency losses for each step in this process - length scales for each are discussed further in Section 2.3.1. There are a myriad of polymer blends that are in use for organic solar cells - the choice of materials is further discussed in Chapter 4. The main limits to efficiency are low absorption, poor charge-carrier separation and high levels of recombination - each of which plasmonic-enhancement has the potential to address.

2.2.5 Amorphous silicon

Amorphous silicon is an attractive candidate for thin-film photovoltaics. With an absorption coefficient approximately two orders of magnitude greater than crystalline silicon, and with cheap, low-temperature deposition conditions, amorphous silicon solar cells have already found widespread use in providing electricity for low-energy portable devices such as calculators and watches. Amorphous silicon differs from crystalline silicon in its lack of long range order. Hydrogen is introduced to passivate silicon bonds that are not able to bond with other silicon atoms, creating ‘hydrogenated amorphous silicon’ (aSi:H) but there are still dangling bonds present within amorphous silicon. The deviation from the crystalline structure can be seen in Figure 2.17.

Charge conduction for amorphous silicon lies somewhere in between the

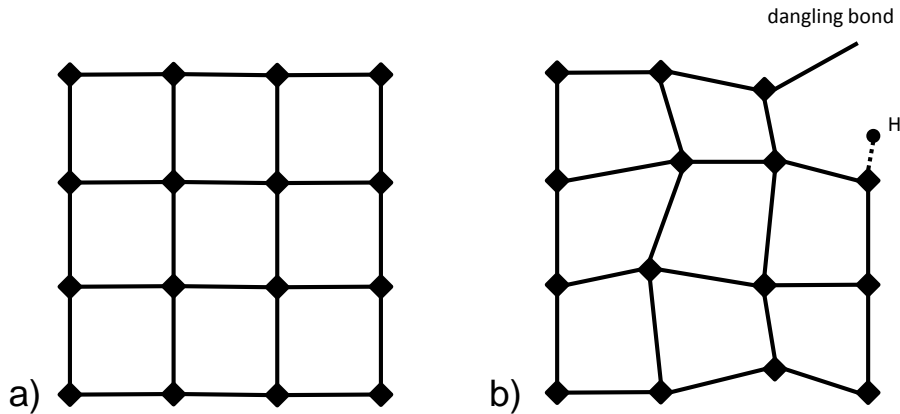


Figure 2.17: (a) Schematic 2-dimensional representation of a crystalline silicon lattice (a) and a disordered amorphous silicon lattice with the introduction of dangling bonds and passivating hydrogen [59].

long-range conduction of crystalline semiconductors and the hopping mechanism more prevalent in organic semiconductors. The lack of long-range order requires a different analytical approach to the standard Bloch theorem, but for the purposes of solar cell operation distinct conduction and valence bands can be identified. The relative position of the Fermi level can be adjusted through doping with phosphorous and boron to create n and p -type amorphous silicon respectively. In this way, amorphous silicon solar cells can be designed similarly to inorganic crystalline semiconductor devices. The typical a-Si:H device is made with a p-i-n junction structure where the central intrinsic (i) region is included to increase the absorption of the device without introducing the extra defects that arise from doping. Thorough reviews of amorphous semiconductor transport can be found in references [13] and [60]. For plasmonic solar cell design, amorphous silicon is considered as a direct band-gap semiconductor with higher absorption than crystalline silicon, larger bandgap (1.6 eV compared to 1.1 eV), and shorter diffusion lengths (100 nm compared with 100 μm) due to the lack of long-range order.

The maximum reported efficiency of amorphous silicon cells is 10.1% [9], again a figure limited by the balance between desiring thick cells for higher absorption and requiring thin cells for low recombination.

2.3 Plasmonic photovoltaics

This section reviews the physics of plasmonic photovoltaics and the key considerations for designing plasmon-enhanced solar cells. It begins with a summary of relevant length scales (Section 2.3.1), before discussing plasmonic interactions in thin films (Section 2.3.2), the balance of absorption between metals and semiconductors (Section 2.3.3), and material cost considerations (Section 2.3.4).

2.3.1 Summary of relevant length scales

We summarise the relevant length scales involved in plasmonic photovoltaics with Figure 2.18 and Table 2.1.

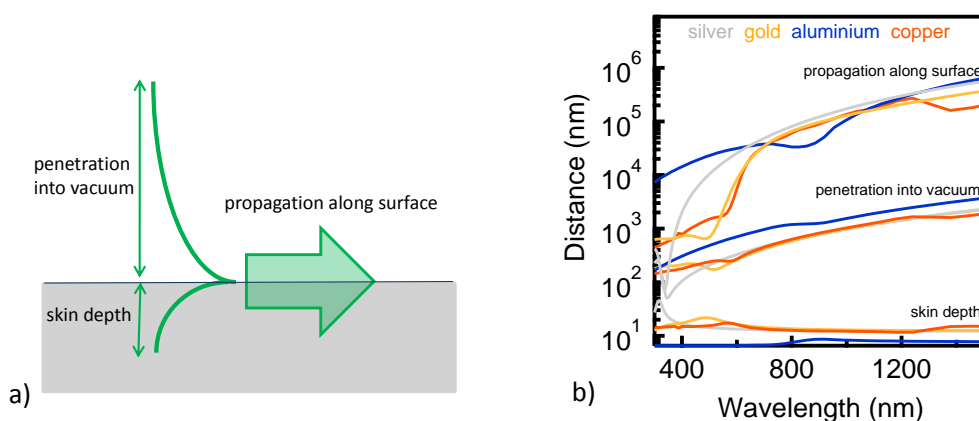


Figure 2.18: (a) Schematic of the length values presented in (b). (b) Skin-depth, penetration into vacuum and propagation along the surface for surface plasmon polariton modes excited at the metal/air interface for silver, gold, copper and aluminium.

Material property	Organic	a-Si	c-Si
Absorption thickness	300 nm	200 nm	2 μm
Diffusion length	5-15 nm	100 nm	100 μm
Transport length	3-50 μm	100 nm	100 μm

Table 2.1: Approximate length scales in photovoltaic materials. Absorption thickness refers to $\frac{1}{\alpha}$ at $\lambda = 600$ nm.

Figure 2.18 shows the optical length scales surface plasmons for Ag, Au, Al and Cu. In Table 2.1, ‘Diffusion length’ refers to length for which

charge carriers travel before recombining. For organic solar cells this refers to the *intra*-polymer diffusion length: that is, an exciton-pair (with its individual binding energy of ~ 0.4 eV) needs to reach an interface between donor/acceptor polymers within 5-15 nm. This is different to the diffusion length for a *single* charge carrier along a polymer (the charge transport length). The short intra-polymer diffusion length is the reason why bulk heterojunction structures are preferred for organic PV devices.

For amorphous silicon solar cells, the diffusion length presented is that for an electron in intrinsic aSi:H, lengths for holes are typically a factor of a third lower. Another important length scale for amorphous silicon solar cells is that of the depletion region. In a typical cell, the depletion region width is ~ 300 nm, designed to be greater than the cell thickness to allow good current collection in the presence of low mobility charge carriers [61].

2.3.2 Plasmonic interactions in thin films

Plasmonic structures enable light to couple to new optical modes that would otherwise be inaccessible in thin films. Thin planar films typically can only support the standard cavity or ‘Fabry-Perot’ type resonances that arise from multiple reflections within the structure. The additional modes made accessible by plasmonic structures are both ‘guided modes’ along the thin film, and ‘evanescent modes’ decaying from the metal-semiconductor interface (if a plasmonic substrate is present). In both instances they are affected by the layer profile of the constituent films and their individual optical thicknesses - often close to the wavelength of light. Whilst the modes subtly interact with each other, we broadly identify them as being either ‘plasmonic’ - when tethered to the surface, ‘Fabry-Perot’ - for modes with a standing wave profile, or ‘guided’ for modes travelling in-plane within the film, discussed further in Chapters 6, 7 and 8.

A further important consideration for plasmonic structures in thin-film solar cells is where they should be positioned within the device for optimal enhancement. Recent research [62, 63] indicates that placing plasmonic scatterers on the rear of the cell is beneficial for two reasons: firstly, to not impede the blue light that is usually strongly absorbed at the top of the cell, and secondly, to enhance absorption for the long-wavelength light that typically

passes through the device unabsorbed.

Further topics of current research in plasmonic photovoltaics includes the question of whether periodic structures provide greater enhancement than random structures (with initial research showing that they can in certain configurations [64, 65]), and what features should an optimal plasmonic structure possess [66]. The optimal geometry of a plasmonic feature has not yet been resolved, and before this project, solar cells had not been demonstrated *within* plasmonic structures. This thesis presents the first solar cells fabricated inside a concave plasmonic shape, directly benefiting from the enhanced field within metallic nanovoids.

In addition to these geometrical considerations, perhaps the biggest unresolved question is whether it is better to use plasmonic structures for their enhanced near-field or for their large scattering cross-sections [67]. This is a question we address in Chapter 8 of this thesis; it depends sensitively on the balance of absorption between a metal and a semiconductor when a plasmon is excited at the interface, introduced next.

2.3.3 Plasmon absorption balance

Light absorbed in the semiconductor of a solar cell generates charge-carriers and results in useful electrical output. Absorption in the metal results in joule heating and the loss of useful energy. The absorption in the metal is referred to as ‘parasitic’ since it does not contribute to photocurrent. As a result, the addition of extra absorbing metal features in a solar cell structure requires a significant enhancement in electrical efficiency to justify its inclusion.

Plasmonic structures can increase useful absorption in a solar cell via enhancing the near-field or by increasing scattering to trapped modes within the device, or both. The balance of absorption is an area of active research and is discussed in detail in Chapter 8, where we present a derivation for the balance of absorption of the plasmonic near-field at a flat interface between a metal and an absorbing dielectric. For spherical particles it can be calculated via the albedo: $\frac{C_{scat}}{C_{abs}+C_{scat}}$, and for various geometries it can be understood via the relevant timescales of the plasmon lifetime, quoted at ~ 50 fs [68] and the electron-phonon relaxation time of several picoseconds [69]. A statistical-mechanics description involving the local density of states is a subject of

Mineral	Crustal abundance (ppm)	Market price (US\$/kg)
Ag	0.08	380.50
Au	0.004	20909
Al	83000	2.44
Cu	60	6.19

Table 2.2: Mineral abundance and market price of plasmonic metals, from [71]

current research [70].

In general, each approach finds that the inclusion of plasmonic structures can greatly enhance device performance in thin-film solar cells, though the method of doing so - via increased scattering or enhanced near-field - depends sensitively on the dielectric function of the semiconductor, geometry of the metal nanostructure, and spacing of the multiple layers within a PV device. These effects are discussed in detail in Chapter 7 and 8.

2.3.4 Material considerations

Plasmonic photovoltaics is a rich field of physical enquiry that has led to new understanding of light-matter interactions at the nanoscale and discoveries of novel charge-transport dynamics at metal/semiconductor interfaces. The question is frequently asked however, if the inclusion of expensive metals such as silver and gold can ultimately be useful for solar cells where cost is such an integral performance indicator (Table 2.2). It is an important question, especially for solar cells that aim for significantly reduced costs of production such as organic solar cells with roll-to-roll processing. A possible response to this question is that we have only just started to understand the physical processes behind plasmonic enhancement in photovoltaics. The theoretical limits to absorption enhancement via light-trapping in the wave-optics regime are not yet established, and the potential for plasmonic structures is novel and exciting. Economic considerations of photovoltaic production expect that high-efficiency solar cells will dominate in a mature market [45], lending support for the investigation of the efficiency enhancements of plasmonic structures. This project investigates silver and gold plasmonic structures due to their low optical losses, but similar absorption enhancements are expected for structures made of less costly metals such as aluminium and copper (Fig. 2.18), though oxidation of these metals needs to be carefully controlled.

2. Background theory

Uncovering a physical understanding of light-matter interactions with plasmonic structures and absorbing dielectric layers is fascinating in itself, and has spurred vibrant research in the field with exciting results. It is this research that we next review.

Chapter 3

Literature review

This chapter reviews the literature of plasmonic-enhancement to solar cells. Section 3.1 reviews the nanoparticle plasmonic approach, Section 3.2 reviews nanostructured plasmonic surfaces, including the instances where plasmons have been found to degrade cell performance. Section 3.3 summarises the emerging literature regarding optimisation principles for plasmonic photovoltaics.

3.1 Particle plasmon enhanced solar cells

In 1996 Stuart and Hall [14] showed increased absorption in silicon photodetectors coated with metal nanoparticles. The approach has since been replicated for solar cells of almost all material classes. Particle plasmon-enhanced solar cells are reviewed in [16] and the motivation for the approach is summarised in Figure 3.1. When light at plasmon resonance frequencies radiates onto the surface of a metal nanoparticle there is an enhancement of electric field intensity surrounding the particle (Fig. 2.7) and a concurrent increase in the particle's scattering cross section (Equation 2.18).

For a silicon/air interface, approximately 96 % of radiation is directed into the silicon substrate (Fig. 3.1b). This is attributed to the high density of optical modes within the silicon compared to the air [72] and is understood in terms of Fermi's Golden Rule - that the transition probability is proportional to the local density of states. Providing additional states for light to couple into, due to the higher refractive index of the dielectric, preferentially directs the scattering into the cell.

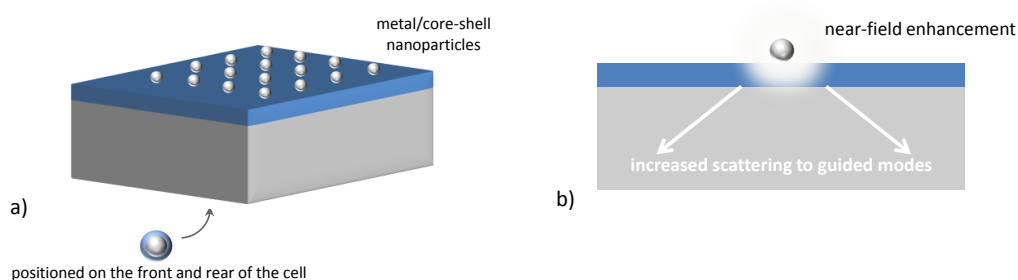


Figure 3.1: a) The nano-particle plasmon-enhanced approach: plasmonic particles (either bare or coated with a dielectric) are placed on the front and/or rear of the solar cell. b) Plasmonic resonances of the particles are utilised both for their near field enhancement and strong scattering into the underlying semiconductor.

The literature is rapidly growing and solar cells of a vast array of materials and cell design have shown enhanced efficiencies due to the application of plasmonic nanoparticles. Reviews of the particle plasmonic approaches can be found in Catchpole et al. 2008 [16] and Atwater and Polman 2010 [67]. We draw attention in the following section to selected examples for organic and inorganic photovoltaics.

Organic plasmonic solar cells

Organic solar cells benefit strongly from enhanced light collection. Greater absorption gives higher short-circuit current densities, but also allows thinner cells - with gains in open-circuit voltage from reduced recombination.

There have been a large number of studies of gold and silver nanoparticles applied to the surface of various organic solar cells [73–76] and almost all show an increase in photocurrent. The earliest work was presented by Rand, Peumans and Forrest [74], showing the enhancement of organic tandem solar cells that contained silver nanoclusters. Recent research has shown absolute efficiencies increasing from 3.05% to 3.69% (Fig. 3.2) due to the inclusion of silver nanoparticles by Kim et al. [75].

Morfa et al. (2008) [76] used a similar approach to Kim and observed an increase in efficiency from 1.3% to 2.2%. Duche et al. (2009) spun spherical silver nanoparticles from solution onto a cell made of MEHPPV:PCBM cell and observed an relative increase in efficiency of 50% [77]. We also note the approach of Chang et al. [78], in which the process of particle fabrication is

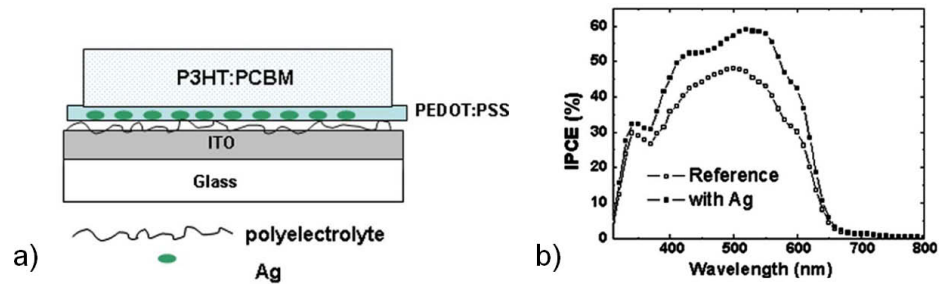


Figure 3.2: a) Geometry of organic solar cells fabricated by Kim et al. (2008) [75], with average Ag particle size of ~ 13 nm, b) Incident photon to current conversion efficiencies of a cell without plasmonic-enhancement to one containing Ag nanoparticles.

similar to the initial templating of spherical nanovoids described in Section 2.1.5. Chang deposited metal through self-assembled colloidal nanospheres to create plasmonic nanotriangles on top of a glass substrate, and found cells with silver nanoparticles had an efficiency of 2.42% compared to 1.68% for those with titanium particles. There continues to be strong investigation into particle-plasmonic enhanced organic solar cells. Significant challenges remain in tuning plasmonic resonances of the metal particles and in avoiding the quenching of excitons that occurs at particle-polymer interfaces, potentially alleviated by dielectric-coated core-shell nanoparticles, recently investigated by Brown et al. (2011) [79].

Inorganic plasmonic solar cells

The largest plasmonic enhancements for solar cells have occurred for inorganic devices. The best results to date are from thin silicon solar cells fabricated by Pillai et al. (2007) [15]. Here, 12 nm and 16 nm particles were deposited on a $1.25 \mu\text{m}$ thick silicon solar cell, with photocurrent enhancement of up to a factor of 16 observed at particular wavelengths (Fig. 3.3), and a 33% increase of current density for the whole device.

Enhancements of a factor of approximately 1.5 have been observed in thick ($\sim 200 \mu\text{m}$) silicon solar cells fabricated by Beck et al. (2009) [62], finding that placing the plasmonic scatterers on the rear of the device is beneficial - allowing blue light to enter the cell unimpeded and red light to be scattered at the back surface [63, 80]. Spherical particles have been also been deposited

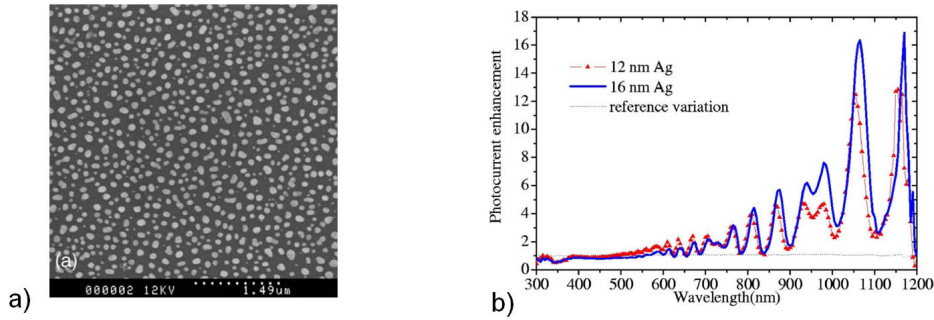


Figure 3.3: SEM (a) and photocurrent enhancement (b) from Pillai et al. [15], for a $1.25\ \mu\text{m}$ silicon-on-insulator solar cell with 12 nm and 16 nm silver nanoparticles deposited on the surface. Photocurrent enhancement of up to 16x is observed with a 33% increase in photocurrent generation across the whole spectrum.

on gallium arsenide solar cells by Nakayama et al. (2008) [81], with a resulting 8% relative increase in current density across the whole cell. Modelling by Mendes et al. (2009) indicates orders of magnitude enhancement is possible for intermediate-band inorganic solar cells made from hybrid crystalline semiconductor-quantum dot array structures, where the intermediate-band serves as an additional ‘quasi-junction’ to overcome the Shockley-Queisser limit [82].

The challenges with nanoparticle enhanced inorganic solar cells are the balance between particle coverage, parasitic reflection and particle-exciton electric interaction. With careful optimisation, the approach will continue to yield further real increases in device efficiency.

3.2 Plasmonic surface solar cells

In concert with the plasmonic-particle approach there is interest in the use of nanostructured *surfaces* to enhance solar cell performance. This section introduces the different geometries of plasmonic-surface texturing before summarising the current state-of-the-art for plasmonic back contacts. Detrimental effects from plasmonic surfaces are next reviewed before a discussion on the optimisation of surface profiles and cell layers.

3.2.1 Plasmonic rear-surface contacts

Utilising a plasmonic structure for the rear contact of a solar cell has a number of advantages: plasmonic enhancement of the field occurs precisely where an optical field null would normally be present, the absorption of short wavelengths is not compromised before encountering the resonant structure, and the rear-surface can be used simultaneously with light-trapping features at the front surface.

Various geometries have been investigated. Tvingstedt et al. in 2007 [83] modelled and fabricated a periodically nanostructured aluminium back contact for plasmonic enhancement in organic solar cells. The grating structure had a period of 280 nm and feature height of 50 nm (Fig. 3.4a). A thin layer of Ti/TiO layer was applied on top to overcome the charge blocking nature of the aluminium oxide that forms on top of the aluminium structure. The polymer:PCBM blend layer and PEDOT:PSS layer were then spin coated on top of the structures, with the PEDOT:PSS layer acting as the transparent top anode. Light of TM and TE polarisations were shone on the sample to distinguish between scattering effects and plasmonic effects (Fig. 3.4b). The surface plasmon resonance is clearly distinguished in the photocurrent measurement.

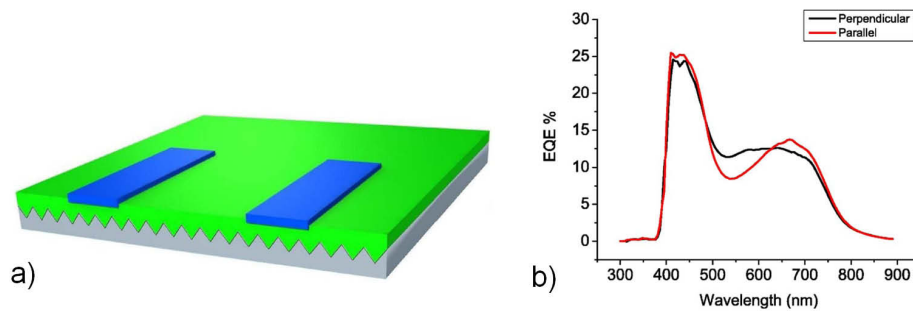


Figure 3.4: a) Schematic cell of Tvingstedt et al. [83] with the nanostructured Al bottom cathode (50 nm height, 280 nm periodicity, 150 nm thick active absorber), and semi-transparent PEDOT:PSS top anode. b) External quantum efficiency measurements for TE (parallel) and TM (perpendicular) modes of incident light.

Since then, solar cells have been investigated with a broad variety of rear-surface plasmonic structures including sinusoidal gratings [84], rectangular gratings [85, 86], nanocones [87], nanodomes [64, 66, 88] and nanoholes [89, 90], with all showing enhanced absorption and photocurrent over identically

prepared flat cells. Imprinted nanohole arrays fabricated by Ferry et al. (2009) [90] increased amorphous silicon cell efficiency by 37% from 4.49-6.16% (Fig. 3.5) with the majority of the active silicon layer in these cells *above* the textured surface.

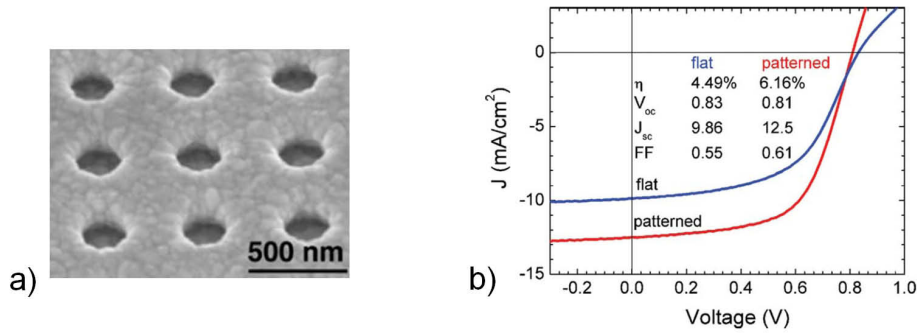


Figure 3.5: a) Imprinted nanohole arrays by Ferry et al. [90], showing enhanced efficiency under solar illumination compared to flat cells (b).

A natural choice for another texturing geometry was that achieved by random etching of glass substrates. Commercial substrates of known roughness are readily available and in 2011 Ferry et al. [91] compared periodic dome structures to randomly arranged structures and chemically roughened glass coated with silver, finding a periodic array of mediumly textured bumps with 400 nm diameter and spacing to have higher photocurrent generation than randomly arranged surfaces, or randomly textured silver-coated glass (Fig. 3.6). The enhancement is attributed to both the roughness power-spectrum of the substrates and the excitation of Bragg-like diffraction modes from the ordered nanodomains.

3.2.2 Detrimental plasmonic absorption

The inclusion of plasmonic structures in solar cells does not always result in enhanced photocurrent. As early as 1991, research had shown that rough metal near an active silicon layer of a solar cell led to parasitic absorption [92]. Franken et al. in 2007 [93] examined the effect of roughness of a silver back contact for a thin microcrystalline silicon solar cell. Rough silver with 100 nm of ZnO:Al was used as the back-reflector of the device, and excitation of the surface plasmon resonance at short wavelengths led to decreased reflectance from the silver (Fig. 3.7). Haug et al. in 2008 [94] investigated ZnO:Al

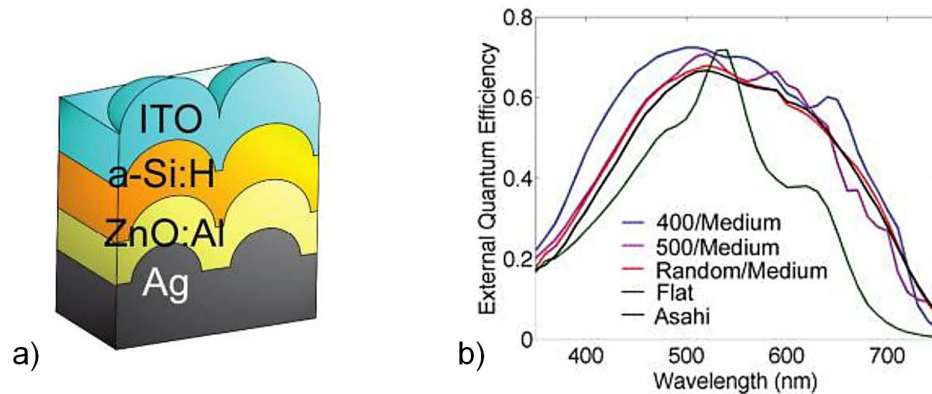


Figure 3.6: a) Nanoimprinted dome structure of cells by Ferry et al. [91] with 130 nm ZnO:Al, 115 nm aSi and 80 nm ITO top contact. b) External quantum efficiency measurements of domes of various diameter in a square lattice compared to randomly arranged and randomly textured Asahi glass.

coated silver films on a sinusoidal polymer grating with period of 890 nm and height of 70 nm, and found similar detrimental plasmonic absorption leading to lower reflectances of the surface and reduced cell performance.

3.3 Summary

In 2010, a review article in Nature Materials [67] summarised the various approaches of plasmonics for improved photovoltaic devices at the time (Fig. 3.8).

What was not yet clear at the time the review was written was how to identify which plasmonic process was most beneficial for each photovoltaic material, nor had the spacer layer been identified as a key mediator of light coupling to various modes within the device. Solar cells had also not yet been fabricated *inside* plasmonic cavities - utilising the strong localised plasmon resonances within nanovoids. This thesis demonstrates the first solar cells fabricated within nanovoid arrays (Chapter 6), yielding a four-fold (400%) enhancement in efficiency for organic solar cells compared to identically prepared flat solar cells. The first nanovoid amorphous silicon solar cells are also demonstrated (Chapter 7), showing 20% greater efficiency than flat solar cells, with 50% enhancement over flat cells found with randomly textured silver substrates and carefully optimised spacer layer thickness. The importance of the spacer layer is examined through spectral and computational

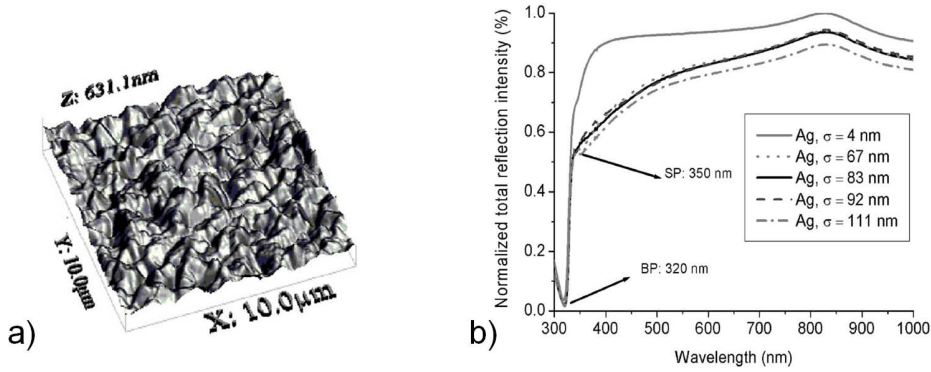


Figure 3.7: (a) AFM measurement of the textured Ag layer that leads to reduced absorption (b) and ultimately reduced cell performance in a $2 \mu\text{m}$ thick $\mu\text{c-Si}$ solar cell, by Franken et al. [93]. Roughness is represented by σ . The absorption peaks of the bulk plasmon resonance (BP) can be seen for all layers, absorption at the surface plasmon resonance (SP) is observed for rough Ag layers.

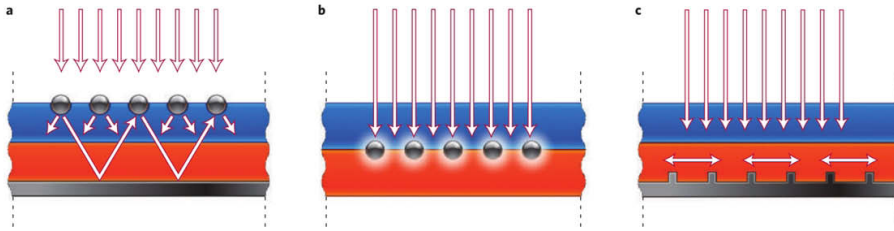


Figure 3.8: Summary of plasmonic light-trapping geometries for thin-film solar cells from Atwater and Polman 2010 [67]. a) Plasmonic resonances of metal nanoparticles preferentially scatters light into the semiconductor thin film. b) The enhanced near-field of localized surface plasmon resonances of metal nanoparticles directly generates increased numbers of electron-hole pairs in the semiconductor. c) Excitation of surface plasmons by a corrugated metal back surface couples light into trapped modes that propagate in the plane of the semiconductor layer.

analysis. The analytical expression for the balance of absorption between metal and semiconductor is identified for each of the leading thin-film solar cell materials, leading to clear design principles for plasmonic enhancement in thin-film photovoltaic devices (Chapter 8).

It is the design and fabrication of these devices that we now present.

Chapter 4

Nanovoid solar cell design and fabrication

This chapter presents the motivations for the nanovoid photovoltaic approach. It then discusses factors influencing cell design and describes the techniques of fabrication.

4.1 Motivations

The key motivations for investigating nanovoid structures as the plasmonic rear-contact of thin-film solar cells are:

- Nanovoid fabrication allows controllable tuning of resonant plasmon wavelengths through the parameters of void diameter, height and material.
- Plasmonic enhancement of the electromagnetic field occurs precisely where an optical field null would normally be present - allowing thinner cell fabrication and larger electric fields within devices.
- Nanovoid substrates allow tuning of the *spatial* location of light absorption - an effect that can be exploited to increase exciton generation, separation and collection.
- Absorption enhancement at the rear surface allows conventional light trapping techniques to be employed at the top surface

- Nanovoids can be consistently and reproducibly fabricated, and allow large-area scalability.

4.2 Nanovoid photovoltaics

Using the above principles, nanovoid plasmonic photovoltaics are designed to harness the enhanced fields to increase light absorption in solar cell materials deposited on top (Fig. 4.1 and 4.2).

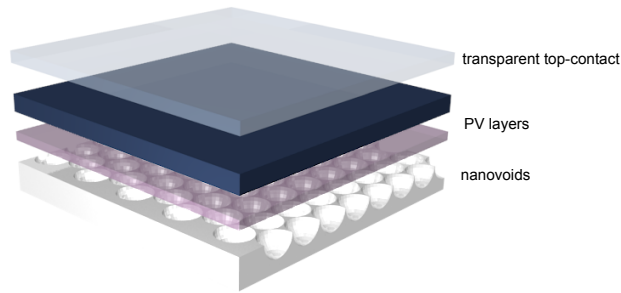


Figure 4.1: Schematic diagram of solar cells fabricated on a nanovoid substrate.

A challenge of the approach arises from the nanovoids acting as the opaque substrate on which cells are fabricated. Organic solar cells are typically fabricated on transparent indium tin oxide (ITO) substrates. PV layers are subsequently deposited on top, with the metallic rear contact made by thermal evaporation of a thick, opaque aluminium layer. For nanovoid photovoltaics, having a metallic substrate which is then coated with device layers, requires us to fabricate devices in an ‘upside-down’ configuration. This forces careful selection of an appropriate transparent top-contact. For organic solar cells it must be a material that conformally deposits over a structured surface without leading to shorting, whilst still maintaining high-transparency.

For amorphous silicon solar cells the challenge is preventing the diffusion of metal into the amorphous silicon layer during deposition. Amorphous silicon is typically deposited on thin chromium layers which allows smooth conformal deposition. The work function of chromium also provides good electron extraction for amorphous silicon. Substituting chromium with plasmonic metals requires the selection of an appropriate buffer layer to prevent diffusion into the active layer and careful design of device architecture to ensure good carrier-extraction.

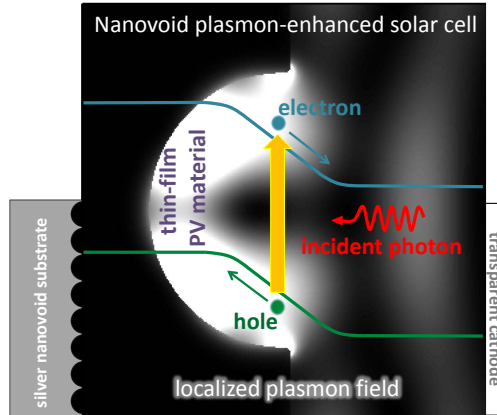


Figure 4.2: Schematic diagram of the energy structure of a nanovoid plasmon-enhanced solar cell. Plasmonic enhanced absorption occurs in close proximity to the hole contact at the region of highest electric field, allowing efficient carrier separation and extraction.

For both solar cell materials, with the above considerations and the inherent challenges of designing a new working PV device, materials are selected with detailed attention to electrical, optical and material properties, reviewed next.

4.3 Device design considerations

The design of nanostructured substrate plasmonic-enhanced solar cells requires consideration of various factors:

- Absorption spectrum and refractive index of photovoltaic material
- Energy levels of conduction and valence bands within PV materials
- Work function of electrodes
- Plasmonic resonance of nanostructured substrate, and
- Length scales of plasmonic resonance, PV absorption and transport

In addition to these are device engineering considerations including material morphology within nanostructures, contact geometry, temperature and oxidation sensitivity, and perhaps most significantly, deposition techniques

of PV and electrode materials. In general, the most robust method for developing new cell architectures is to start from a working device structure and change a single parameter at a time. This is the approach of our project, outlined in the following section, however, it is instructive to examine the matrix of design considerations. We start with the two most important parameters to match for PV design: absorption spectra and energy levels of the PV materials.

4.3.1 Material choice

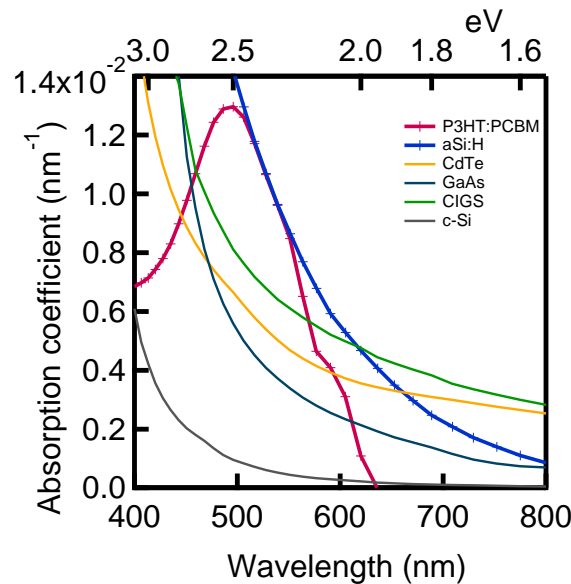


Figure 4.3: (a) Absorption coefficients (α) for poly(3-hexylthiophene):phenyl-C69-butyric acid methyl ester (P3HT:PCBM), hydrogenated amorphous silicon (a-Si:H), CdTe, GaAs, copper-indium-gallium-selenide (CIGS) and crystalline silicon (c-Si), from [95].

The absorption spectral profile of a semiconductor is critical for designing the plasmonic features for enhancing absorption in a solar cell. Semiconductors typically absorb strongly at shorter wavelengths with an exponential drop towards the band-edge (Fig. 4.3). It is in this near band-edge region that cells often stand to benefit most from enhanced absorption, and light-trapping features should be designed accordingly.

Alongside the absorption profile we need a knowledge of both the valence

Semiconductor	HOMO/valence band	LUMO/conduction band
PCBM	6.1	3.7
P3HT	5.2	3.5
MEH-PPV	5.1	2.9
F8BT	5.9	3.5
a-Si:H	5.7	4.0
c-Si	5.1	4.0
CIS	4.8	5.8
Ru dye N3	6.1	4.2
CdTe	6.2	4.7
GaAs	5.5	4.1

Table 4.1: Summary of energy levels for selected PV semiconductors (in eV). The values above, especially for organic polymers, are approximate representations of average orbital energies. They are each affected by deposition/growth conditions, material purity and surface preparation. Values are from references [96], [97], [98] and [99] for the organic materials respectively and [100] for the inorganic materials.

Work functions	
Au: 5.1	Ag: 4.4
Al: 4.2	Cu: 4.7
Cr: 4.5	Ca: 2.9
ITO: 4.8	FTO: 4.4
ZnO: 4.5	TiO ₂ : 4.2
LiF: 3.7	pedot-pss: 5.0

Table 4.2: Work functions of various conductors (eV). Presented values are found to vary up to ~ 0.3 eV with deposition/growth conditions and surface preparation.

and conduction band energies (or HOMO/LUMO levels for organic polymers) and work functions of candidate electrode materials in order to appropriately design a device (Tables 4.1 and 4.2).

Work functions can change significantly with the conditions of deposition and processing, reference [13] provides a thorough introduction into the relevant physics, and the range in values for conducting oxides is also affected by the ratio of the metal/oxide blend. Interestingly, a shift in work function up to 0.3-0.5 eV can be achieved through the adsorption of particular molecules [101] on the metal surface. For this project, we quote the generally accepted values, but keep in mind their possible shift.

The approach of nanovoid-plasmonic enhancement for solar cells sets the

substrate of the device to be either gold or silver. Requiring transparency of the top contact leads us to choose either conducting oxides or thin (< 20 nm) layers of metal for the opposite electrode. Recent research has also shown promising potential for silver nanowire meshes [102, 103], discussed further in Chapter 6.

Alongside considerations of absorption, energy levels, work functions and transparency, are the critical considerations of deposition technique, substrate temperatures required for material deposition, material strengths and impact energies during deposition processes. We next review the deposition techniques used for this project.

4.4 Deposition techniques

After various attempted cell designs of different materials, four thin-film deposition techniques were used in fabricating the majority of solar cells for this project: plasma-enhanced chemical vapor deposition (PECVD), spin-coating, sputter coating and metal evaporation.

4.4.1 Plasma-enhanced chemical vapour deposition

Chemical vapour deposition allows the production of high-purity conformal thin solid films via the reactance of one or more precursor gases moved through a reaction chamber. Flowing precursor gases in the presence of a plasma enhances the chemical reaction rates and allows deposition at lower substrate temperatures [104, 105]. For the deposition of intrinsic (i-type) hydrogenated amorphous silicon, the reactive gas silane (SiH_4) is flowed through the chamber in the presence of hydrogen gas. To form n-type a-Si:H, phosphine (PH_3) is added to the gas flow. A high frequency plasma at 50 MHz is struck between a top plate and the substrate, and reactants deposit amorphous silicon conformally along the substrate surface. The particular recipe for amorphous silicon layers fabricated for this project in the Plasmalab μP system is to heat the substrate to 200°C , with plasma at 50 MHz running at 23 W. Throttle pressure is held at 400 mT and silane gas is introduced for the i-type layer at a ratio of 1:9 with hydrogen gas. For n-type a-Si:H, diluted phosphine gas is introduced at ratio of 3:2:5 with silane and hydro-

gen, giving the ratio of pure phosphine to silane of 0.5%. p-type a-Si:H, though highly beneficial for solar cell performance, is not fabricated within Cambridge due to the toxicity and instability of diborane gas (H_6B_2). This requires us to fabricate Schottky-type devices with reduced charge-carrier separation and collection than p-i-n a-Si:H solar cells (Section 2.2.5), though we find adequate performance to allow examination of photonic and plasmonic effects.

4.4.2 Spin-coating

Spin-coating allows the controlled deposition of thin soluble polymer films onto a substrate. A droplet of solution containing the dissolved polymer is deposited onto a sample which is then spun at speeds between 500 - 8,000 revolutions per minute. The solution experiences a centrifugal force in its spinning frame of reference and is spread across the substrate. As the spinning continues, the solution flattens, excess material is flung off and the solvent starts to evaporate, leaving a thin polymer film on the substrate. This film is then typically post-annealed on a hot-plate under nitrogen to ensure the remaining solvent is evaporated.

Final thicknesses of polymer films can be sensitively controlled through the choice of solvent, the concentration of the polymer within this solvent, and the spin speed of the spin-coater [106, 107]. By using solvents that are mutually orthogonal, different polymer layers can be spun on top of one another. Within this project, polymer films of thicknesses between 50 - 200 nm are typically spun.

4.4.3 Sputter-coating

Sputter-coating is the deposition of thin films of metals and metal oxides from the surface of a target onto a substrate. Two systems were used for the sputtering of indium tin oxide and aluminium-doped zinc oxide in this project, both located in the Centre for Advanced Photonics and Engineering cleanrooms at the University of Cambridge. Each system generates a plasma at 50 MHz in the presence of argon. High-energy argon ions strike the material target and eject molecules from surface. These are then transported to the substrate where they condense to form a thin film. Sputter-

deposition typically operates at higher pressures (~ 3 mT) than those for evaporation (discussed further below), lowering the mean free-path and allowing more conformal deposition onto structured features of a substrate [108, 109]. Al:ZnO and ITO films between 30-200 nm were sputtered for the fabrication of solar cells in this project. It is important to note that impact energies of sputtered molecules on the substrate surface are high compared to other thin-film deposition techniques. Sputtering ITO onto devices made from thin polymer films routinely results in the ITO penetrating through the polymer layer resulting in shorting of the device, discussed further in Chapter 6.

4.4.4 Metal evaporation

Metal evaporation allows smooth deposition of thin metallic films onto a substrate. A chamber is pumped to pressures of approximately 5×10^{-3} mT and a small amount of metal held in a crucible or evaporation boat is heated to its melting point. Heating is achieved by either passing a current through the metallic boat containing the material to be evaporated (for thermal evaporation) or by locally heating the metal by rastering an incident electron beam across the material (e-beam evaporation). As the metal vapourises, molecules travel ballistically towards the substrates held above the metal. For smooth deposition, substrates are rotated above the source. By controlling the planar angle at which the substrates are held, we are able to selectively evaporate on either high or low-aspect ratio parts of a nanostructured substrate, discussed further in Chapter 8. E-beam and thermal evaporation systems in the Nanoscience Centre at the University of Cambridge were used for this project for the evaporation of silver and gold thin films at thicknesses of 15-200 nm at typical deposition rates of 1-5 Å/s.

4.4.5 Dye-sensitized solar cells

A significant research effort of this project was devoted to the fabrication of dye-sensitized solar cells on gold nanovoids with collaborators in the Thin Films and Interfaces research group at the Cavendish Laboratory. Dye sensitized cells are a different design of solar cell from both inorganic and organic semiconductor devices. Instead of absorption within a bulk semiconductor,

they rely instead on the absorption of light by a photosensitive dye which rapidly transfers its excited charge to an adjacent titanium dioxide surface. The circuit is completed by an electrolyte in contact with the dye.

At present, the high temperature required for the annealing of TiO_2 prevents ready fabrication of solar cells on Au nanovoids that are found to blister and degrade for temperatures higher than 250°C .

4.5 Nanovoid fabrication

The final fabrication technique we describe is the formation of ordered arrays of metallic nanovoids. By selecting the size and height of these nanovoids we are able to tune the energies at which localised plasmon resonances are excited. This allows us to target where in the spectrum we would like absorption enhancements in thin film PV devices. We first describe the templating of ordered arrays of spheres, followed by the electrochemical plating that forms the metallic voids.

4.5.1 Template deposition

The formation of ordered 2-dimensional crystal arrays of latex spheres was first examined by Denkov et al. in 1992 [110]. Nanovoids for our project are fabricated according to the procedure outlined in references [19] and [18]. For simplicity we describe the process for gold, though it is equally applicable to silver and a variety of other metals.

A bonding layer of 10 nm of Cr is thermally evaporated onto a glass microscope slide which has been cleaned by sonication in de-ionised water, acetone and isopropanol, followed by 10 minutes of plasma etching. Gold is then thermally evaporated on top of the chromium layer to a thickness of 200 nm. The metal-coated slides are then again extensively cleaned by further sonication in isopropanol (for 1.5hrs), followed by successive rinsing with de-ionised water. These substrates are then immersed in an ethanolic solution of mercaptopropanol for three days to allow a monolayer to adsorb on the gold surface. The mercaptopropanol layer reduces the contact angle of water on the substrate due to its hydrophilicity, and helps to form the close-packed array of spheres. After the mercaptopropanol soaking, substrates

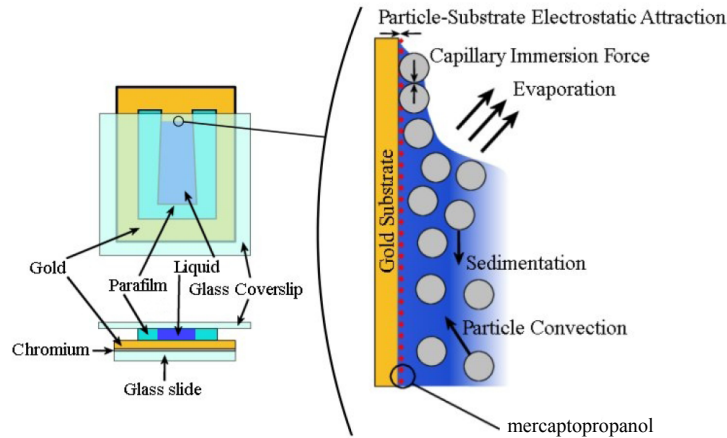


Figure 4.4: Schematic of the evaporation cell used for template assembly and formation of the close packed array of spheres. From [111].

are covered with a clean coverslip to form a small fluid cell by means of an intermediate thin layer of Parafilm (Pechiney Plastic Packaging). The cell is approximately $100\ \mu\text{m}$ thick with an area of $1\ \text{cm}^2$ (Fig. 4.4). The solution of latex spheres is dropped into this thin cell with a syringe, and the substrate is held vertically in an incubator at 25°C for a week.

In solution, the latex spheres are negatively charged and do not aggregate. As the water evaporates from the top edge of the cell, the meniscus tail draws spheres out of the solution, leaving behind a close-packed monolayer array of spheres on the gold surface (Fig. 4.5).

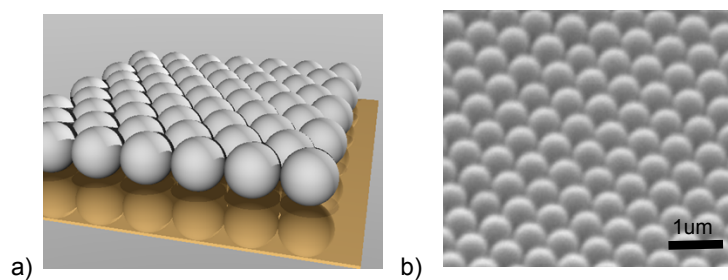


Figure 4.5: a) Schematic of sphere template and (b) SEM of an array of 500 nm diameter polystyrene spheres on gold [19].

4.5.2 Electrochemical plating

Having formed the ordered array, the next step in nanovoid fabrication is the electroplating of metal from the rear substrate through the sphere array.

Deposition is performed using three electrodes - the sample substrate acts as the working electrode, the counter (platinum) electrode supplies the charge to complete the circuit and the reference (Calaman) electrode monitors the charge passed through the circuit (Fig. 4.6a).

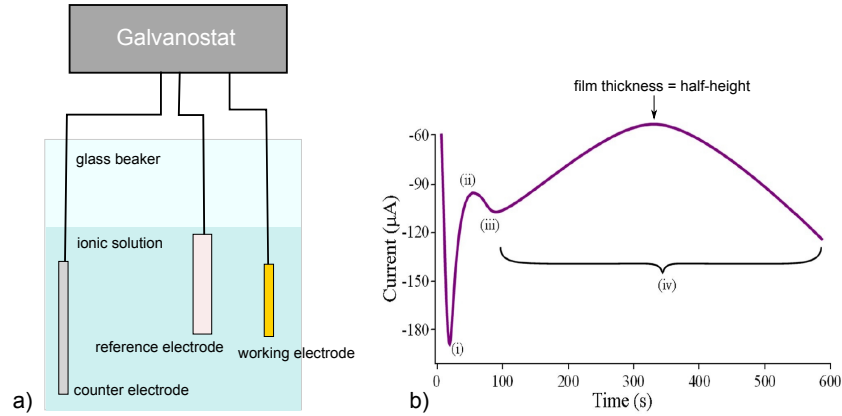


Figure 4.6: (a) Setup of electrochemical deposition. b) Graph of current vs time for the deposition of gold through a close-packed sphere template, adapted from [111]. Labelling discussed in text.

The deposition occurs when the working electrode becomes negatively charged (point (i) in Figure 4.6b). Positive ions in the solution (Au^+) are drawn towards the negative electrode and when the voltage is sufficiently high to overcome the Coulomb potential, undergo the reaction: $\text{Au}^+ + e^- \rightarrow \text{Au}$. After nucleation, individual metal islands are formed (up to point ii), which eventually coalesce to form a metallic film. At this point, the speed of deposition is limited by the rate at which ions can diffuse out of solution and onto the substrate. This steady-state of diffusion-limited current (point iii) allows us to monitor the thickness of the film in relation to sphere height. During this stage the voltage is held constant at -0.75 V . As the cross-sectional area of growth changes with height, the rate of metal deposition decreases, and reaches a minimum at minimum cross-section area - the point at which the film has grown to half the sphere height. Continuing further past this point results in further encapsulation of the spheres. With continuing deposition, the nanovoid arrays resist complete connection at the top and instead form pillow-like structures. The fabrication and characterisation of these structures is discussed in detail in references [22] and [20].

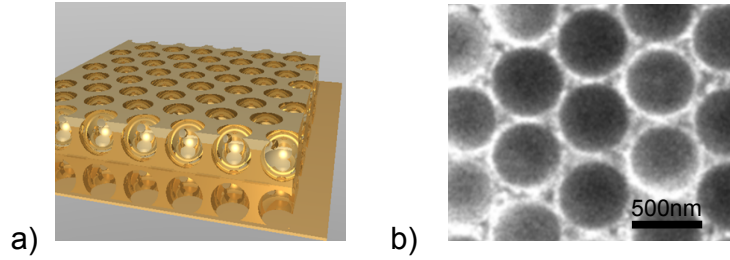


Figure 4.7: (a) Schematic of metallic nanovoids and (b) SEM of an array of 500 nm gold nanovoids grown to half-height.

Once the electrochemical templating is complete, the spheres are dissolved by sonicating in dimethylformamide for two hours, leaving behind an ordered array of metallic nanovoids (Fig. 4.7). Throughout this project, nanovoids made of gold were fabricated by myself, with silver nanovoids fabricated by our collaborator Jatin K. Sinha in the School of Chemistry at the University of Southampton.

4.6 Nanovoid plasmon control

Creating nanovoid arrays with varying size and height allows control of the spectral position of localised plasmonic resonances.

In theory these can be tuned between $\omega = 0$ and $\omega = \omega_{\text{sp}}$ the surface plasmon frequency - located in the UV for both gold and silver. In practice, absorption due to interband transitions prohibits plasmon resonances for wavelengths shorter than 530 nm in gold and 330 nm in silver. Nanovoid resonances are able to be tuned across the visible spectrum by adjusting void height (Fig. 4.8a) and diameter (Fig. 4.8b).

The maps presented in Figure 4.8 are for Au voids surrounded by air. In the presence of a dielectric with higher refractive index, plasmon resonances red-shift in energy approximately proportionally to n . The red-shift for a planar surface plasmon polariton is given by:

$$\omega_{\text{sp},2} = \omega_{\text{sp,air}} \left(\frac{1 + \epsilon_{\text{air}}}{1 + \epsilon_2} \right)^{1/2} \quad (4.1)$$

Here $\omega_{\text{sp},2}$ is the surface plasmon frequency for the metal/dielectric interface with dielectric function ϵ_2 . For *localised* plasmons of nanoparticles and

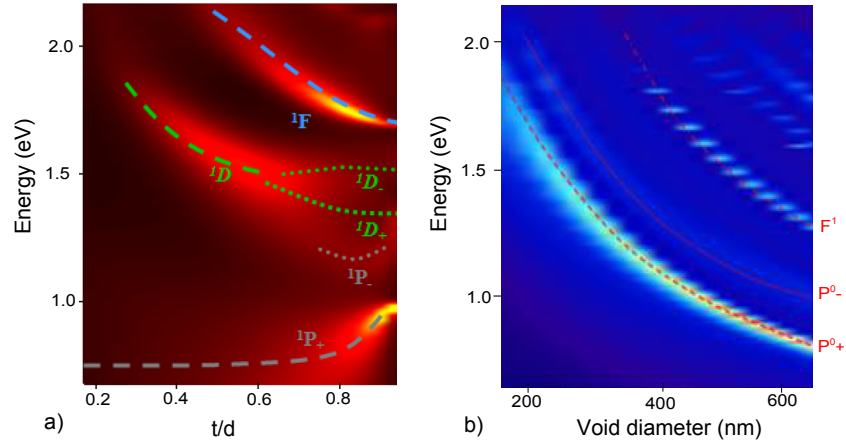


Figure 4.8: (a) Theoretical modelling map of plasmonic resonances for gold 500 nm diameter voids with changing \bar{t} , the ratio of film thickness to void diameter (t/d). Dotted lines are a guide to the eye indicating the theoretical energies of resonance for spherical Mie modes. (b) Modelling of plasmonic resonances for gold nanovoids with $\bar{t} = 0.95$ and varying diameters. Dotted lines are guides to the eye for the corresponding Mie modes. From [112].

nanovoids, resonances shift further due to the field profile being positioned more in the surrounding dielectric than in the metal [112]. This red-shift is an important consideration for the design of nanovoid geometry for amorphous silicon with $\text{Re}(\epsilon_{\text{a-Si:H}}) \approx 15$ and, though not as extreme, for organic polymers with $\text{Re}(\epsilon_{\text{polymers}}) \approx 1.5 - 4$.

4.7 Summary

The design and fabrication of nanovoid solar cells relies on an interdependent mix of parameters that include:

- Absorption and refractive index of the photovoltaic material
- Conduction and valence band energy levels of the semiconductor
- Work function of electrodes
- Charge transport length scales
- Temperature, impact-energy and conformality of deposition; and
- Plasmonic resonance of the nanovoid substrate

Various geometries and substrates were investigated, here we summarise the two systems that served as model devices for the exploration of plasmonic-enhanced absorption.

4.7.1 Organic nanovoid solar cell

The solar cells that form the backbone of results presented in Chapter 6 have the device layer structure as presented in Figure 4.9.

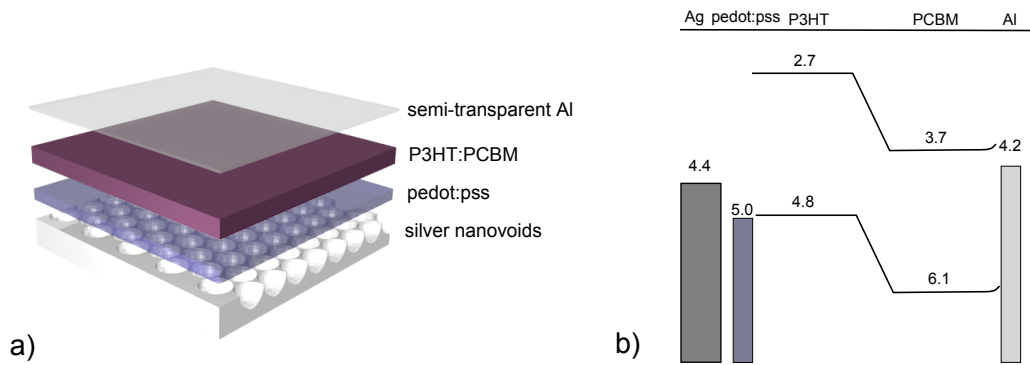


Figure 4.9: (a) Schematic diagram of organic nanovoid cell layers. (b) Energy level diagram of the device.

The design is similar to the standard ITO-pedot:pss-P3HT:PCBM-Al organic solar cell fabricated by collaborators in the OptoElectronics Group at the Cavendish Laboratory and more widely across the organic solar cell community. It is a robust cell with excellent efficiency ($> 5\%$) and has been extensively studied in the literature [54, 58]. The only material changed with our design is the ITO layer - replaced with a plasmonic silver substrate. This change is not trivial however, since this forces our aluminium contact to be thin and semi-transparent, discussed further in Chapter 6.

Silver nanovoids of 400 nm diameter grown to half-height form the substrate, on which pedot:pss (poly(3,4-ethylenedioxythiophene):poly(styrenesulfonate), Cambridge Display Technologies) is spin-coated to form the hole-conducting layer. A 1:0.8 (by weight) blend of regioregular poly(3-hexylthiophene) (P3HT, Merck) and phenyl-C61-butyric acid methyl ester (PCBM, Nano-C) dissolved in dichlorobenzene at a concentration of 20 mg/mL, and spin-coated to form the active polymer layer. A thin (15 nm) layer of aluminium forms the semi-transparent contact. Further fabrication details are discussed in Chapter 6.

4.7.2 Amorphous silicon nanovoid solar cell

The solar cells that are presented in Chapter 7 have the device layer structure presented in Figure 4.10.

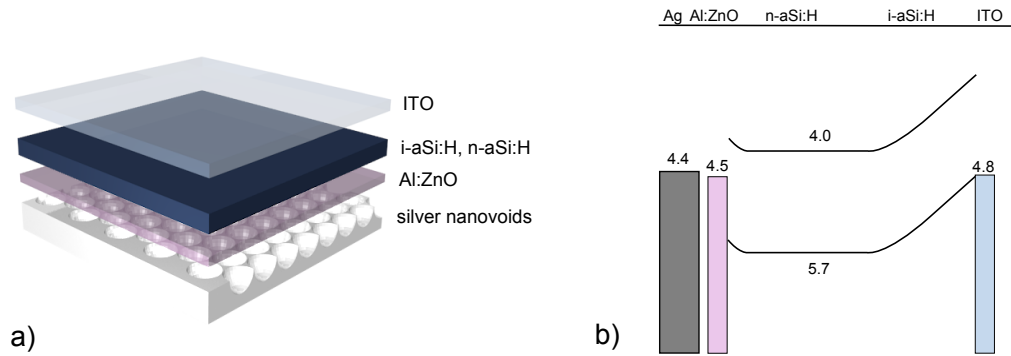


Figure 4.10: (a) Schematic diagram of amorphous silicon nanovoid cell layers. (b) Energy level diagram of the device.

The device is based on the Schottky-junction between the a-Si:H layer and the ITO. A transparent conducting layer of aluminium doped ZnO (1 %wt., Testbourne) is included as a buffer to prevent diffusion of silver into the a-Si:H during PECVD. Silver nanovoids of 200-500 nm are used as the substrate with varying Al:ZnO thicknesses between 30 - 200 nm. ITO (80 nm) is sputtered on top of the a-Si:H layer to form the transparent contact.

Chapter 5

Characterisation and simulation

This chapter presents the techniques of characterisation and simulation. Sections 5.1 and 5.2 describe the optical and electrical experimental rigs used for measurement, and Section 5.3 discusses the methods of computational simulation of the electromagnetic field within nanostructures.

5.1 Optical characterisation

Alongside standard optical microscopy and electron-microscopy, characterisation of the voids is undertaken using angle-resolved reflectivity in a purpose-built goniometer setup (Fig. 5.1), originally developed at the University of Southampton. From this rig, analysis of broadband angularly-resolved reflectance allows direct access to the energy-momentum dispersion relation of optical modes within structured devices. A fibre-coupled supercontinuum white light sources is used for illumination; for Chapter 6 we use a passively mode-locked 1064 nm, 1 nm, microchip laser (JDS Uniphase) passed through a holey fibre (Blaze Photonics) to deliver a continuous spectrum from 480-1500 nm, and for Chapters 7 and 8 we use a Fianium, SC450-6 at 4 W quasi-continuous that delivers a spectrum from 380-1500 nm. In each case, the light source is attenuated via beam-samplers, collimated and passed through a linear polariser. The beam is then guided and focused onto the sample at a beam power of 0.1 mW, spot size 0.2 mm^2 and power density 50 mW/cm^2 . The sample can be moved both in-plane (x and y) and rotated

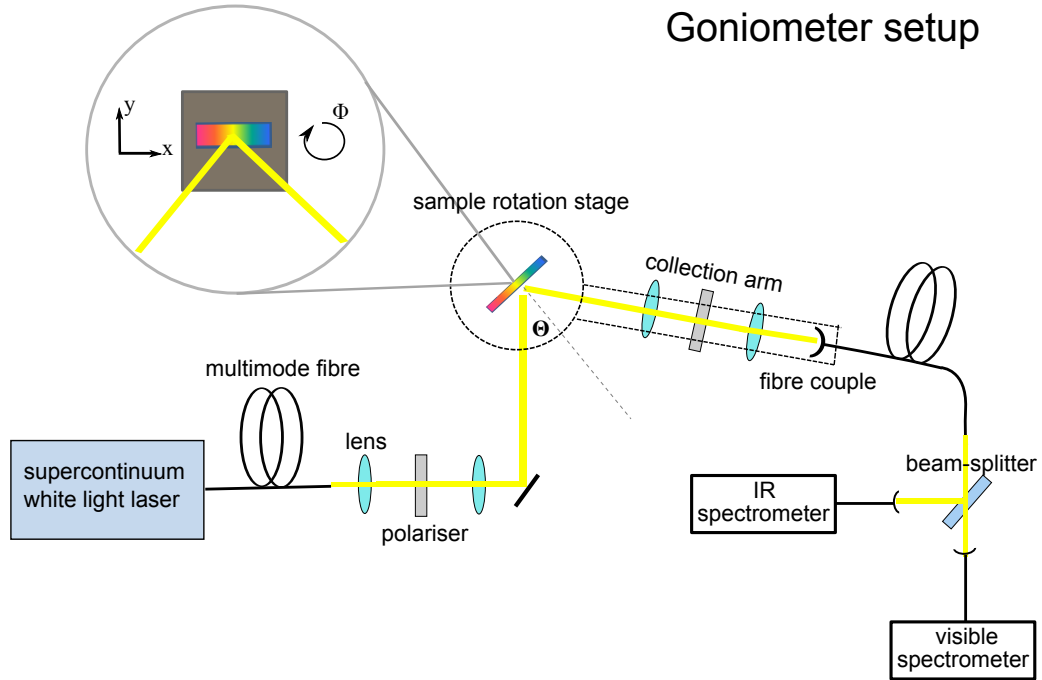


Figure 5.1: Schematic diagram of angularly-resolved reflectance setup. The sample rotation stage and collection arm are independently moved, allowing full automated control of light incidence in x, y, θ and ϕ directions on the sample.

in the θ and ϕ directions. To enable these degrees of freedom, the laser beam must be incident on the sample at the centre of both planes of rotation, with the sample precisely aligned in the same plane. This alignment is sensitive and requires a high degree of precision to ensure reflected light is focused to precisely land on the $500\ \mu\text{m}$ diameter fibre-couple in the collection arm. The collection fibre leads to a spectrally-flat polka-dot beam-splitter which sends light through visible and IR filters within a cage-optics system before coupling to visible (Ocean Optics QE65000) and near-infrared (Ocean Optics NIRQuest) spectrometers respectively. Both spectrometers are connected to a software package (Igor, Wavemetrics) that allows simultaneous control of goniometer motors and spectra-recording in the same interface. This setup allows fully-automated scans in each of the x, y, θ and ϕ directions. The final system is able to record reflectance spectra from $\lambda=380\text{--}1500\ \text{nm}$ across incident angles $0\text{--}70^\circ$, producing the graphs presented in Chapters 6 and 7.



Figure 5.2: Custom experimental photovoltaic set-up allowing microscopic control of prober tip location and simultaneous electrical and optical characterisation.

5.2 Electrical characterisation

To measure the electrical response of nanovoid solar cells a custom-made electrical measurement rig was developed. A Keithley 4200 Semiconductor Characterisation System (K4200) is connected via triax cable to a prober station mounted underneath the objective of an optical microscope (Olympus BX50). The prober tip consists of fine steel needles wrapped with thin gold wires (0.5 mm diameter) that serve as the final contact to the electrical device under test. The prober station rests on a stepper motor (Newport SMC100) allowing automated micron control over the height of the prober tip. For illumination, light from a 75 W Xenon lamp (Bentham IL75e) is passed through a double-turret mounted monochromator (Bentham DTMc300) and fibre-bundle-coupled into the optical microscope. An 800 nm short-pass filter is loaded into the microscope to ensure second-order illumination is blocked, before final focusing through a 10x objective onto the sample (at an average power density of 1 mW/cm^2). Reflected light is fibre-coupled through the microscope to a visible spectrometer (Ocean Optics QE65000). Each of the components - K4200, stepper motor, monochromator and spectrometer - are computer-controlled via Igor allowing simultaneous optical and electrical measurement (Fig. 5.2) with micrometer precision of the prober tip location.

5.3 Modelling

Alongside experiments we undertake theoretical modelling to understand the behaviour of light in our nanostructures. Computational simulations allow an understanding of the fate of light within such devices and provide a framework for predicting optimal design features for absorption enhancement.

There are various approaches to model the behaviour of light in nanostructured geometries including finite-difference time-domain techniques (FDTD), discrete dipole approximations and boundary-element methods. Each approach has a suited class of problems for which it is most efficient. For this project we use boundary-element methods and FDTD simulations to analyse the behaviour of light in nanovoids and randomly textured substrates. This section reviews these two methods, the geometries for which they are suited, and the features of each that must be considered to ensure the optical physics is realistically modelled.

5.3.1 BEMAX

Analytical solutions to Maxwell’s equations exist for spherical particles through Mie theory, but are not able to be extended to irregular structures such as the truncated spherical cavities of nanovoids. The spherical symmetry of nanovoids does, however, allow for more efficient computation of electrodynamics than with non-symmetric structures. We use a boundary-element method developed by our collaborator F. J. Garcia de Abajo at the Instituto de Optica CSIC in Spain. The model, named ‘BEMAX’ for Boundary Element Method for AXial symmetry, is able to efficiently calculate the full electromagnetic field within cylindrically symmetric structures by reducing the exact solutions of Maxwell’s equations to integrals over surface charge and current [113]. These surface charges and currents define the vector and scalar potentials $\bar{\mathbf{A}}$ and ϕ , which then allow calculation of the \mathbf{E} and \mathbf{B} fields. The approach is able to calculate axially symmetric structures (such as nanovoids) in full 3D with greater efficiency than both electromagnetic solvers and discrete dipole approximations. Extensive testing of BEMAX was carried out, both by Prof Abajo and our research group. The first such validation is done via comparison with Mie theory and the publicly available Mie calculator MiePlot (Fig. 5.3). A difference of less than 0.1 % is observed

in absorption cross-section - representative of a wide range of tests for the code.

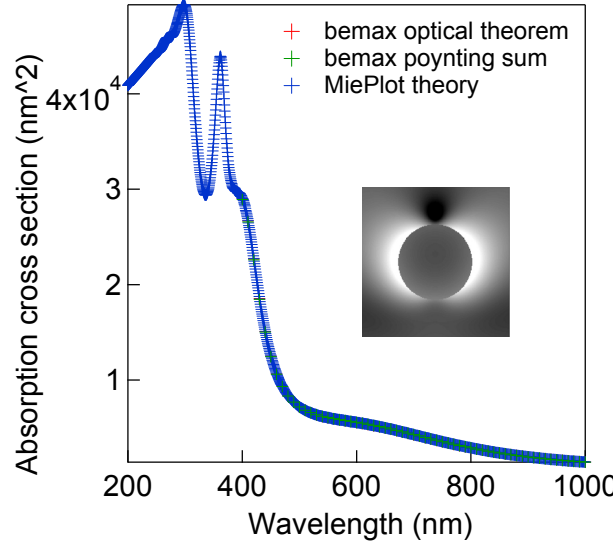


Figure 5.3: Absorption cross-section calculations with BEMAX and Mie theory for a 100 nm radius silver nanoparticle. Two independent calculations of the cross-section are used in BEMAX - one via the integration of the Poynting vector over the surface of the sphere, and one through the optical theorem. Results are compared with MiePlot - three data points are present in the graph with the difference between them less than 0.1%. The inset shows the $|E|^2$ field spatial profile at $\lambda=600$ nm.

For structures that cannot be calculated with Mie theory, the test of BEMAX is through comparison with experiment. Previous research has extensively studied BEMAX calculations of spherical nanovoid arrays and found close agreement of experimental and simulated reflectance at a wide range of angles and void parameters [22]. Similar calculations are published of coupled spherical particles [114] and particle-in-void arrays [115].

The geometry input for BEMAX is generated by defining a closed surface separating two materials. This approach is suited for solid closed objects such as nanoparticles, but poses a challenge for modelling semi-infinite *surfaces* that instead form a boundary between two half-planes. To surmount this problem, surfaces are closed by a ‘virtual’ structure that allows the definition of material regions, but does not support surface charge or current (Fig. 5.4a). In practice, this works efficiently for surfaces where the surrounding material is either air or another non-absorbing dielectric. Coating

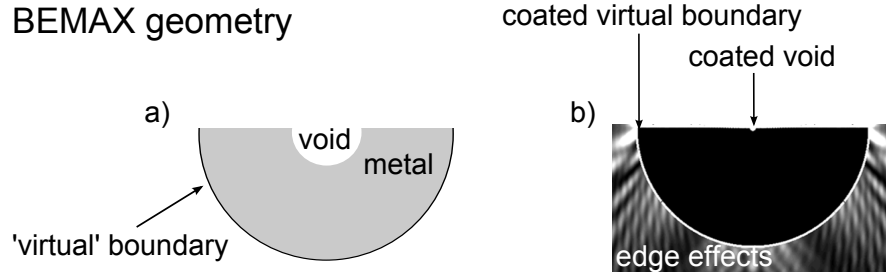


Figure 5.4: Typical input geometry for voids in BEMAX showing the position of the virtual structure (a). Calculated $|E|^2$ fields for a 400 nm diameter Ag void coated with silicon, with large ($10 \mu\text{m}$) coated virtual boundary (greatly zoomed out) showing unphysical edge effects (b).

a surface with discrete layers on top (such as a nanovoid with solar cell layers) leads to light being guided through the virtual structure to the rear of the simulation region, resulting in unphysical simulation of absorption cross sections for the void region. A significant research effort was devoted to eliminating this artifact by myself, Part III student Mathias Arens and Prof. Abajo. We introduced radial artificial absorption profiles, outcoupling structures and tapered guiding layers with coated void structures, but each proved unable to limit the coupling of light into guided modes in the virtual structure - resulting in unphysical simulations of the optical field (Fig. 5.4b). A strategy for overcoming this is to include periodic boundary conditions in the boundary-element method, currently being developed by Prof Abajo. In summary, BEMAX is found to be a fast and suitable tool for the simulation of localised plasmons in single nanovoid structures. For the simulation of layer-coated nanovoid arrays and the inclusion of surface plasmons from the hexagonal lattice, we developed finite-difference time-domain approaches, discussed next.

5.3.2 Lumerical

Finite-difference time-domain modelling discretises space into cells of finite volume. A broadband pulse of light is incident on the system where the frequency span of the pulse is directly related to its narrowness in time through Fourier transform. The essence of FDTD modelling arises from the consideration that the time derivative of the E-field is proportional to the curl of B (Equation 2.3). At a particular timestep the curl of B is evaluated across the

discretised cell (known as a Yee cell), which allows calculation of the change in E . This is repeated for the B -field, and the simulation leapfrogs through time until the simulation reaches a steady-state once the pulse has passed. This approach is well suited to a system for which the broadband frequency response is desired (such as a solar cell). The limitations to FDTD modelling arise from the need for fine discretisation in space, with the cell size needing to be smaller than both wavelength and nanostructure feature size. A further complication arises from the internal requirement that the broadband pulse is defined with a single wavevector for all frequencies. For normal incidence this is not an issue, but for light incident at a set oblique angle it means that each wavelength of light, whilst having the same in-plane component of momentum, will have an incident angle different from the set angle.

Example Lumerical Input Geometry

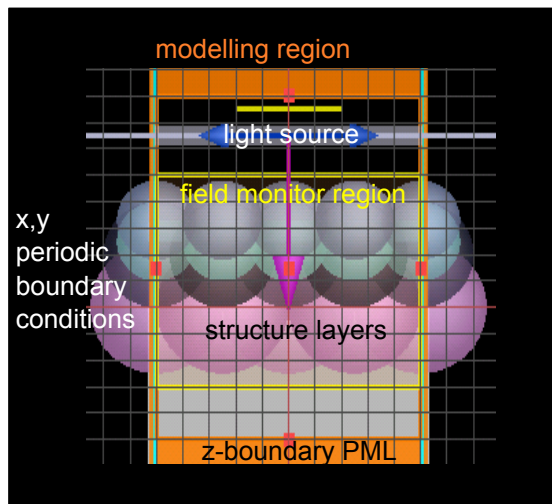


Figure 5.5: Example input of Lumerical FDTD software showing the geometry of simulated objects and the modelling region.

We installed and the developed simulations with the commercially available software Lumerical [116], where a typical input geometry (Fig. 5.5) defines regions graphically or through script to allow detailed control over source, monitor and feature parameters. The software is routinely used in the broader optics research community with published validation [116], though we carry out further validation by comparing simulations and reflectance measurements on planar surfaces, alongside tests between scattering cross-sections for spherical particles and those obtained from analytical Mie solu-

tions. With reference to planar layers and simple transfer matrix calculations (presented in Chapter 7), these comparisons provide the ‘sanity tests’ for our use of this software.

5.4 Summary

We harness each of optical, electrical and computational approaches to understand plasmon-enhanced absorption in nanostructured solar cells. Angularly-resolved reflectance measurements provide direct access to the energy-momentum dispersion relation of optical modes within nanostructures. Spectrally-resolved photocurrent measurements allow electrical characterisation of devices and a means to separate parasitic absorption in metal and absorption in the active material that contributes to photocurrent. Computational simulations allow both an understanding of optics within nanostructured devices and a tool to predict optimum structures for maximum absorption enhancement. We utilise all of these in examining solar cell performance in the next two chapters.

Chapter 6

Organic plasmon-enhanced nanovoid solar cells

6.1 Introduction

This chapter presents the performance of organic solar cells fabricated on nanovoid substrates. Cell design is discussed first followed by the presentation of results. Localised plasmon resonances of spherical nanovoid arrays are found to strongly enhance solar cell performance by a factor of 3.5 in external quantum efficiency at plasmonic resonances, with a four-fold enhancement in overall power conversion efficiency. This design represents a new class of plasmonic photovoltaic enhancement: localised plasmon-enhanced absorption within nanovoid structures. Our novel nanovoid cell geometry (Fig. 6.2) [117] simultaneously increases absorption while using the plasmonic substrate for electrical contact. As with all rear-surface plasmonic designs, the absorption of short wavelengths is not compromised before reaching the resonant plasmonic structures [63, 118], and enhancement can be achieved in concert with top-surface light trapping techniques, including that of plasmonic nanoparticles. Our nanovoid structures additionally display strong dewetting properties [119] and have significant capacity for omnidirectional absorption [120]. Angularly-resolved spectra demonstrate strong localised Mie plasmon modes within the nanovoids. Theoretical modelling suggests a possible route towards spatial separation of colour on the nanoscale for third generation plasmonic photovoltaics.

6.2 Methods

Metallic nanovoids are formed by electrochemical deposition through a template of close-packed self-assembled latex spheres [34] as presented in Chapter 4. The spheres are subsequently dissolved leaving an ordered array of sphere segment nanovoids. Here we fabricate hemispherical silver nanovoids of 200 nm radius and height.

To include a transparent cathode for organic devices on silver nanovoids, various device geometries were examined. We first attempted to fabricate a cell with the same standard device geometry of those regularly fabricated in the Optoelectronics Group at the Cavendish Laboratory. This consists of an ITO substrate, followed by polymer layers with evaporated Al contacts at the rear of the cell. Contact ‘legs’ are attached to the device enabling electrical measurements in a standardised photocurrent rig (Figure 6.1a).

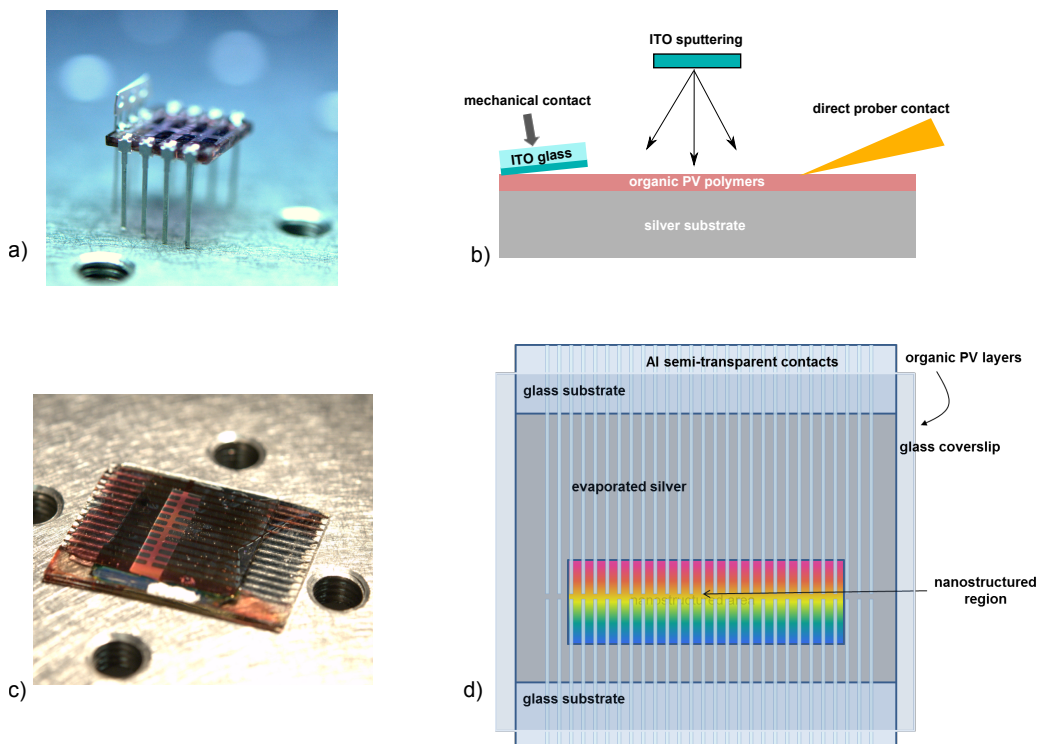


Figure 6.1: (a) Standard polymer solar cell design. b) Attempts at forming the top contact of nanovoid solar cells. c) Nanovoid solar cell. d) Schematic top-view of nanovoid cell design. For scale, the optical bench in the photographs’ background has holes of 6mm diameter.

Since silver forms the opaque substrate this led to an exploration of fabri-

cating an ITO substrate on the top of the polymer layer. Direct sputtering of ITO was examined alongside mechanical ‘sandwiching’ of ITO glass onto the substrate. Both led to repeated shorting of devices. Sputtered ITO was found to punch through the polymer layer, and sandwiching led to ITO directly touching the silver substrate. In addition, we explored using an automated gold prober tip (Chapter 5) to directly contact to the polymer layer. This too led to scratching of the sample and subsequent shorting. A successful contact geometry was found with semi-transparent aluminium forming the top contact (Figures 6.1c and d). A schematic top-view of the cell is shown in Figure 6.2 alongside SEM images of the nanovoid cell. The nanostructured region is typically of 1 cm in width and 0.5 cm in height. The width of each active solar cell is typically 2 mm, with finger length approximately 1 cm. Illumination is provided through the microscope, with spot size of 0.5 mm diameter, preventing cross talk between devices. Devices are fabricated with the structure

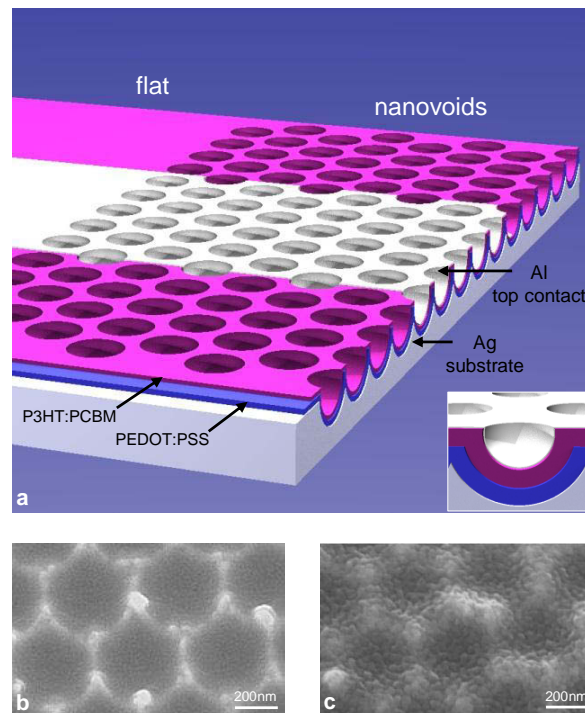


Figure 6.2: (a) Schematic representation of the cell geometry with separate flat and nanovoid regions sharing the same top electrode. Inset: Side-on view of the nanovoid cell. (b) Scanning electron microscope images of polymer-coated nanovoids and (c) polymer-coated nanovoids with evaporated Al top contact.

presented in Chapter 4. A 115 nm hole-conducting PEDOT:PSS layer is

spun on top of the hemispherical nanovoids at 1500 rpm for 1 min with 0.3% (FSO Zonyl) surfactant and annealed at 180°C for 30 min under nitrogen. An organic photovoltaic polymer blend of P3HT (Merck) and PCBM (Nano-C) is dissolved in ratio 1:0.8 (by weight) at a concentration of 20 mg/mL in dichlorobenzene. The solution is spun at 1000 rpm for 1 min and annealed at 115°C for 15 min under nitrogen to form a 90 nm active layer. Finally, 15 nm of aluminium is thermally evaporated through a mask to conformally pattern the semi-transparent top contact (Fig. 6.2c) and the device encapsulated with a thin glass coverslip.

6.3 Results

6.3.1 Angularly-resolved reflectance

Angularly-resolved reflectance of (a) polymer on flat silver, (b) uncoated silver nanovoids, and (c) polymer-coated nanovoids (Fig. 6.3) provides direct access to the energy-momentum dispersion relation of plasmonic resonances. Measurements are taken with the goniometer presented in Chapter 5 and are normalized to a flat silver mirror (NewFocus 5103).

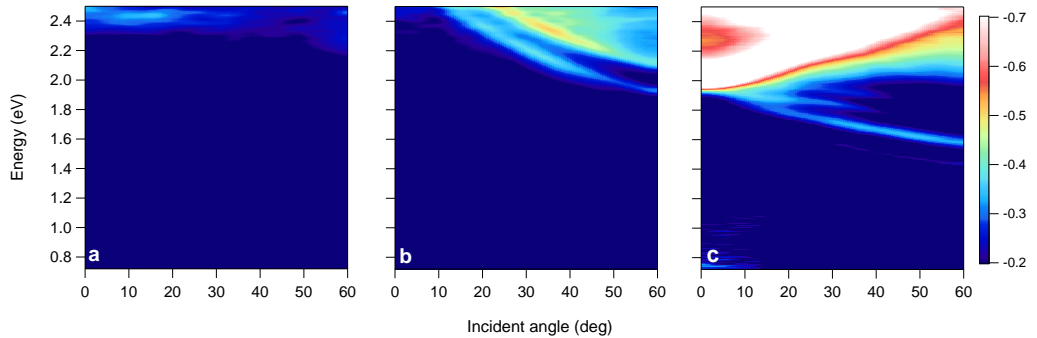


Figure 6.3: Angularly-resolved reflectance of (a) polymers on flat silver, (b) bare silver nanovoids, and (c) polymers on silver nanovoids. Colour scale is $\log(\text{reflectance})$ with blue indicating high reflectance and red-white indicating low reflectance.

The angularly-independent absorption of P3HT:PCBM polymer blends on flat silver (Fig. 6.3a) shows the typical onset of absorption from 2.2 eV. For uncoated silver nanovoids (Fig. 6.3b) propagating Bragg surface plasmon

modes are seen, coupled via the ordered hexagonal lattice of the nanovoid substrate [20, 22]. These provide a similar absorption enhancement mechanism to the back-surface-grating-like structures reported previously [83, 84, 87, 88, 90, 121]. These Bragg modes for the silver/air interface red-shift in the polymer-coated silver nanovoids (Fig. 6.3c) due to the increased refractive index of the polymer relative to air, appearing at 2 eV.

For a silver nanovoid/air interface, *localised* modes only appear above 3 eV. These also red-shift when polymer layers ($n=1.59$) encapsulate the void, as observed in our theoretical simulations (Fig. 6.4a). This red-shift is sensitive to the polymer thickness inside the void and indicates the successful conformal coating of the 115 nm PEDOT:PSS and 90 nm P3HT:PCBM layers (Fig. 6.2b). Enhanced absorption is observed over a wide range of angles, favourable for real environments with significant diffuse sunlight [120].

6.3.2 Theoretical simulation

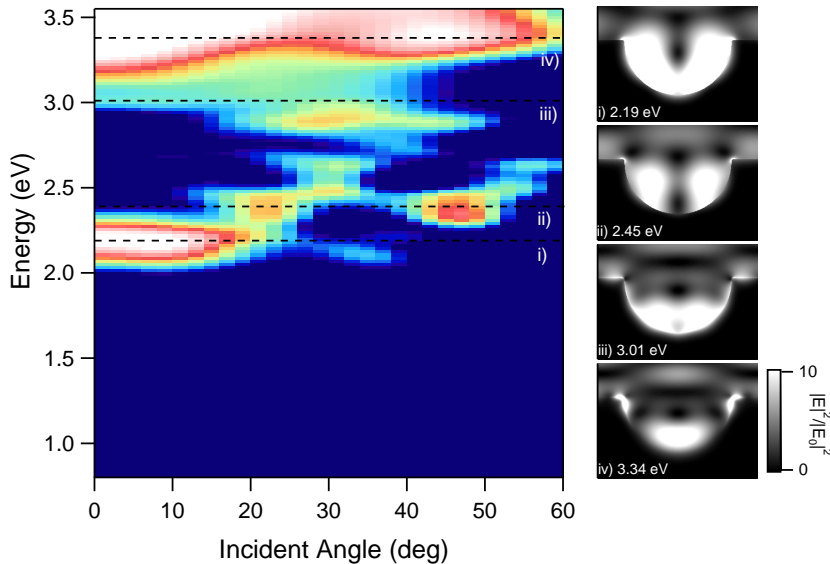


Figure 6.4: Boundary element simulations of angularly resolved absorption of a silver nanovoid structure embedded in a dielectric of refractive index $n = 1.59$. Red-white indicates higher absorption and blue indicating low absorption. (i-iv), Electric field intensity profiles at plasmon resonances (positions marked by black lines).

Silver nanovoids are modelled with BEMAX (Chapter 5) and are embedded in a non-absorbing dielectric with weighted refractive index matching the solar cell layers. Localised (*i.e.* non-dispersive) Mie plasmons within the cavity are seen above 2 eV, with specific momentum matching required for the different modes [22], agreeing well with experimental results (Fig. 6.3).

Simulations of the $|E|^2$ field intensity at these resonances (Fig. 6.4) demonstrate the significant field enhancements within the void structure. It is these regions of concentrated field that elicit enhanced absorption within the polymer-coated nanovoids. Different spatial distributions for higher energy localised modes are observed within the void geometry [22].

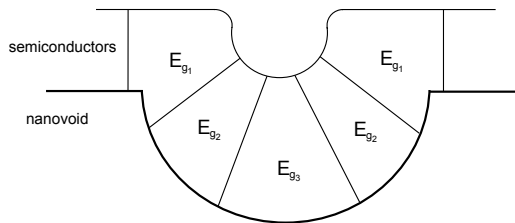


Figure 6.5: Schematic of a speculative third generation PV geometry using the spatial separation of colour on the nanoscale found with plasmonic nanovoids. Placing semiconductor materials at spectrally matched regions of plasmonic concentration allows selective enhancement of absorption suited to each material’s bandgap E_g . Whilst there would be significant difficulties in fabricating such a device, we uncover here a novel route towards separating colour in the subwavelength regime.

This spatial tuning suggests a first step towards plasmonic enhancement for third generation thin-film PV devices, with nano-cavity plasmonic resonances at different wavelengths tailored to selectively enhance absorption in matched materials at targeted device locations (Fig. 6.5). By locating semiconductor materials where localised plasmons concentrate a particular wavelength range of light, absorption enhancement can be selectively targeted for each material’s bandgap, discussed further in Chapter 8. Possible geometries include hot-carrier cells or multiple quantum dot cells, and whilst future devices using this effect will require control of deposition far beyond that achievable today and is purely speculative at present, we discover here one of the first possible routes for spatially separating colour on the nanoscale for PV enhancement, recently identified as a key mechanism for next generation photovoltaics (Polman and Atwater (2012) [122]).

6.3.3 Photocurrent measurements

For the uncapped nanovoid/polymer structures a peak in absorption is observed at 590 nm (Fig. 6.6a), rising again towards 500 nm. These absorption enhancements correspond to the localised plasmon resonances near 2.2 eV and 2.5 eV. The peak at 590 nm is due to a mixed mode [20] between the localised mode and the propagating surface plasmons seen in Fig. 6.3(c). Transfer matrix simulations (green lines) of the planar devices (with P3HT:PCBM optical constants from Hoppe et al. [123]) match the flat data well.

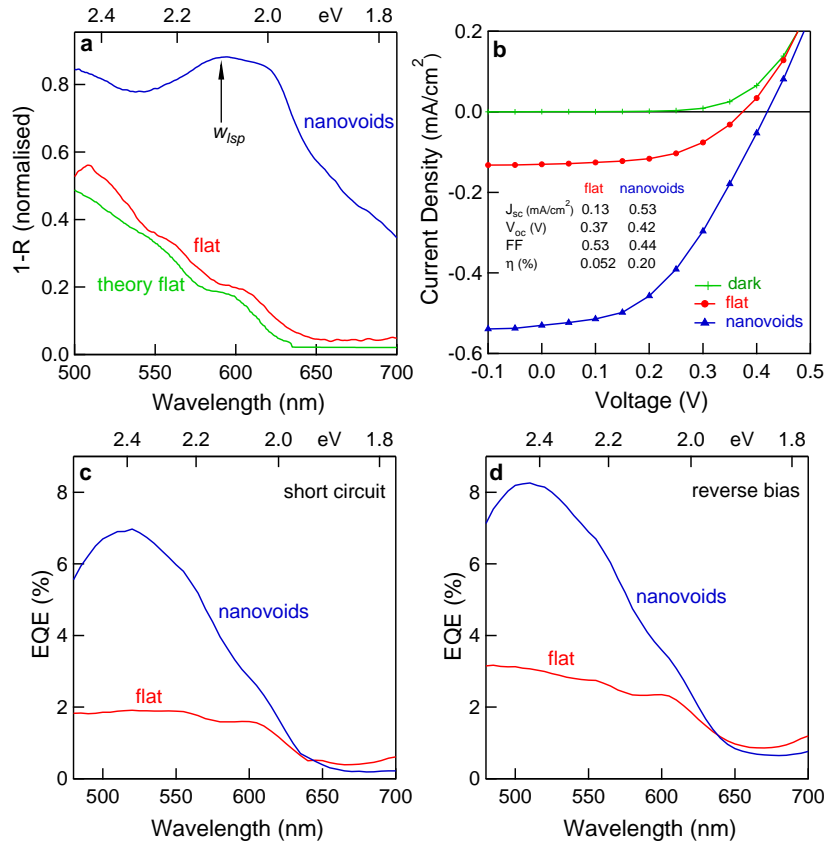


Figure 6.6: a) Extinction spectra, $A(\lambda) = 1 - R$, at normal incidence for polymer on silver nanovoids (measured, blue) and flat silver (measured, red) with transfer matrix simulations for the planar structures shown in green. b) J-V curves under xenon lamp illumination comparing nanovoid cells to flat cells. The dark J-V curve is common to both. c) External quantum efficiency at zero bias and reverse bias -1 V (d) of nanovoid cells *vs.* flat cells.

The enhanced optical absorption in the nanovoid geometry improves the

PV performance. External quantum efficiency (EQE) at zero bias and a reverse bias of -1 V are measured with a monochromated xenon lamp. The measurements at reverse bias extract nearly all of the light-generated carriers, separating effects of absorption enhancement and carrier transport. Nanovoid and flat cell measurements are taken from the *same* cell-pixel containing separate nanovoid and flat sections of the silver substrate (Fig. 6.2b). The measurements are representative across a range of cell pixels and cell batches.

A strong peak at 520 nm in charge-carrier generation is observed for the nanovoid cell compared to the planar cell (Fig. 6.6c). The position of the peak corresponds closely to the expected localised plasmon resonance of the polymer-coated silver nanovoid, with the spectral shift from Fig. 6.6 due to the red-shifting of the plasmon resonance by the inclusion of the Al top contact and the sensitivity of resonance to thickness. We find that plasmonic field enhancements for the Ag nanovoid/organic semiconductor system contribute directly to enhanced photocurrent with proportionally higher absorption in the semiconductor than in the silver, highlighting the importance of active material absorption for plasmonic cell design [121]. Little difference is found between EQE at short circuit (Fig. 6.6c) and at -1 V (Fig. 6.6d) measurements, indicating that the significant differences between nanovoid and planar cells are due to light absorption and not charge-carrier extraction. The nanovoid cell shows higher EQE across large spectral bandwidths from $\lambda = 450 - 650\text{ nm}$. The slight improvement in planar device performance for $\lambda = 650\text{ nm}$ is due to the Fabry-Pérot mode between the flat Ag and Al layers. Overall efficiencies are however limited by the excessive reflectivity of the 15 nm Al top contact, with a maximum EQE of 7% from all devices. Transfer matrix simulations indicate $< 8\%$ of incident light from $400 - 800\text{ nm}$ is transmitted through the Al so that $> 90\%$ of visible light is reflected, implying effective internal efficiencies are really in excess of 50% . In addition, layer thicknesses of the active polymer and PEDOT:PSS have not been optimised for absorption and carrier extraction. The flatter EQE of the planar cells from $\lambda=460 - 550\text{ nm}$ compared to Kim et al. [124] is also due to these microcavity spectral effects, as well as contributions from wavelength dependent carrier-extraction (seen from the EQE at -1 V). Despite this, we clearly show here that absorption is enhanced over $460 - 650\text{ nm}$ for

a nanovoid cell compared to an identically prepared flat cell sharing the same electrode.

6.4 Discussion

Three key features give rise to absorption differences between a flat cell and a nanovoid cell: i) localised and surface plasmon coupling, ii) PV material volume and morphology, and iii) light scattering from the textured back surface. Fabricating cells within sphere segment voids increases the Ag substrate area. Replacing flat substrates with textured nanovoids increases the average optical path within the cell. While both increased active semiconductor area and enhanced scattering from the textured nanovoid substrate are significant advantages to the nanovoid geometry, both are largely wavelength independent. Neither can account for the strong increase in EQE at 520 nm. We thus explain this enhancement by localised plasmonic resonances of the polymer-coated silver nanovoid substrates.

The overall enhancement in charge-carrier generation for the nanovoid cell compared to flat cells is expressed in the short-circuit current density (J_{sc}) of the J-V curves (Fig. 6.6b, dark J-V curve common to both) under white light (Newport Xenon Lamp 96000, AM1.5G spectral mismatch factor 2.0) at an intensity equivalent to 0.5 suns at AM1.5G after spectral mismatch correction. A sharp increase in J_{sc} from 0.13 to 0.53 mA/cm² is observed in the nanovoid cell, with a corresponding increase in open circuit voltage (V_{oc}) from 370 mV to 420 mV. The fill factor of the nanovoid cell is slightly decreased from 0.53 to 0.44 for the nanovoid cell, possibly due to the increased resistance of the now textured aluminium top-contact.

Overall, nanovoid cells show four-fold enhancement in total cell efficiency from 0.052 % to 0.20 %. We refer to these organic plasmonic solar cells as *orgasmonic* when showing enhancement ([125]). Absolute efficiency values are currently limited by the significant reflection from the 15 nm Al top contact. There are various routes by which this can be overcome. Through optimisation of pressures during sputtering we can reduce the impact energy of ITO molecules as they strike a polymer surface allowing gentle fabrication of a top contact without shorting. Further possibilities include using conducting polymer films [83], and Ag nanowire meshes [102, 103]. These

are the subject of next generation designs in progress - as typical for the first demonstration of a new physical phenomena further optimisation is required to achieve technology-compatible results, however we find here clear evidence for plasmonic enhancements to photovoltaics from this localised plasmon configuration.

It is instructive to consider the efficiency enhancements that would be possible with a present day record-efficiency cell. Whilst four-fold enhancement is not possible - single-junction devices will always be constrained by the Shockley-Queisser limit - we expect gains of 5-10% in relative efficiency with careful optimisation of device fabrication. This enhancement would be primarily through increases in EQE in the near-IR regions of the spectrum, close to the bandgap edge where semiconductors absorb poorly. Further enhancements are expected with the application of plasmonic structures to solar upconversion [126], and other third generation concepts currently under research [122].

6.5 Conclusions

In conclusion, we have fabricated solar cells *within* plasmonically-resonant nanostructures to enhance absorption, demonstrating a new class of plasmonic photovoltaic enhancement available to all solar cell materials. Significant PV enhancement is observed in our nanovoid organic solar cells compared to identically-prepared flat cells, with a four-fold enhancement of overall power conversion efficiency, due largely to an increase in J_{sc} . This enhancement in nanovoid cells is primarily due to the strong localised plasmon resonances of the nanovoid geometry. A possible route towards separating colour on the nanoscale is observed, suggesting future third-generation devices that harness the spatial distribution of the plasmonic field. Our results indicate the significant potential for enhanced photovoltaics utilising localised plasmon resonances within nanostructured geometries. We next explore this potential for amorphous silicon solar cells and compare the plasmonic enhancement from nanovoids to randomly textured silver, identifying key design features for plasmon-enhanced thin-film solar cells.

Chapter 7

Amorphous silicon plasmonic solar cells

7.1 Introduction

This chapter presents ultrathin amorphous silicon solar cells fabricated on three different substrate geometries (Fig. 7.1): nanovoids, randomly-textured glass and flat silver. Angle-resolved reflectance, external quantum efficiency measurements and finite-difference time-domain simulations demonstrate the importance of the spacer layer in determining mode profiles to which light can couple. While 20 % enhancement of cell efficiency is observed for nanovoid solar cells compared to flat, we find that with careful optimisation of the spacer layer, randomly textured silver allows for an even greater enhancement of up to 50 % compared to flat. Coupling mechanisms differ between periodic silver nanovoid arrays and randomly textured silver substrates. Tailoring the spacer thickness tunes the coupling between the near-field and trapped modes with enhanced optical path-lengths. The balance of absorption for the plasmonic near field at the metal/semiconductor interface is discussed for a-Si:H solar cells.

Section 7.2 introduces the fabrication of devices. Section 7.3 examines angularly-resolved reflectance and electrical measurements for each geometry. Section 7.4 discusses the optical physics within each device, and Section 7.5 explores the balance of absorption between a-Si:H and the underlying Ag plasmonic substrates.

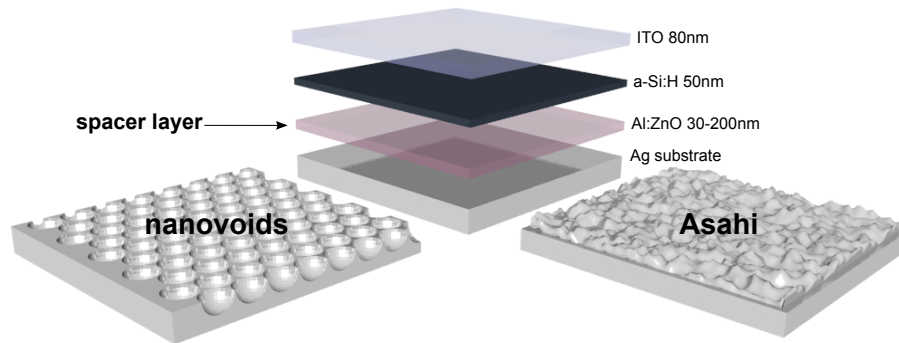


Figure 7.1: Schematic representation of substrate and layer structure for amorphous silicon solar cells.

7.1.1 Introduction to spacer layers

Spacer layers are often included in solar cell devices as a transparent conducting layer between the rear-reflector and active semiconductor. Their role is to prevent diffusion of the metal into the semiconductor, enhance reflection from the rear surface, act as selective electron/hole-transporter, or a mix of the above. For a-Si:H solar cells fabricated on silver contacts, a spacer layer is necessary to prevent the diffusion of metal into the semiconductor. The dielectric layer between the plasmonic feature and active absorber has been examined to understand the distance dependence of plasmonic nanoparticles from thin crystalline Si solar cells [127] and dye-sensitised cells [128]. With plasmonic substrates, previous research has investigated the optical response of a-Si:H solar cells with plasmonic gratings [94, 129], numerically simulated the dependence of buffer thickness on waveguide modes [130, 131], and examined the buffer layer effect on performance for randomly textured reflectors for thick a-Si:H solar cells [92]. The optical, electrical and computational study of thin solar cells presented in this chapter, with only 50 nm of a-Si:H active layer, provides detailed access to understanding the absorption-enhancing properties of the underlying nanostructures. Device performance can be understood in terms of Fermi's Golden Rule; by adjusting the local density of states to which light can couple, the absorption enhancement in the active semiconductor layer can be optimised.

7.2 Methods

Three substrate geometries were investigated: sphere-segment silver nanovoids of radius 100-250 nm grown to half-height, silver-coated randomly-textured glass (150 nm Ag thermally evaporated onto Asahi VU-type [132]), and flat cells (Fig. 7.1), each providing a framework for the investigation of different light-coupling mechanisms within the ultrathin solar cell. Flat cells serve as the reference for scattering-unassisted absorption within the device, with the support of standing-wave Fabry-Perot (FP) type modes for thicker cell layers. Sphere-segment nanovoids harness strong plasmonic resonances weakly tethered to the metal surface [20, 22] allowing the tracking of plasmonic mode-shifts with different material coatings. Asahi VU type glass is a commercially available glass with known roughness and serves as a quantitative, reproducible representative of a randomly textured plasmonic substrate (Fig. 7.2).

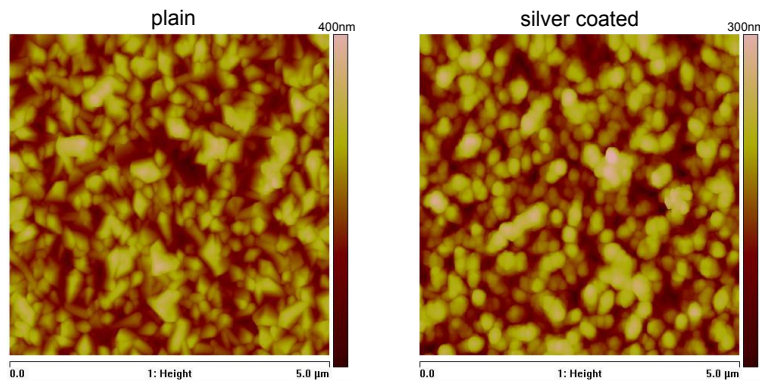


Figure 7.2: AFM measurements on Asahi VU type uncoated glass (a) and coated with 10 nm Cr and 150 nm Ag via thermal evaporation. RMS roughness values are 56 nm and 49 nm for plain and Ag coated substrates respectively.

Silver nanovoids are grown via self-assembly and subsequent electrochemical deposition (Chapter 4), while Asahi VU type glass and flat glass substrates are treated with 10 nm Cr and 150 nm Ag via thermal evaporation.

Fabricating working a-Si:H solar cells on plasmonic substrates proved to be a significant experimental challenge. Amorphous silicon devices typically use a chromium substrate as the rear-electrode, followed by a-Si:H deposition and an ITO top-contact. Depositing a-Si:H directly onto Ag or Au leads to metal diffusion into the semiconductor, causing nanocrystallisation and non-

conformal coating (Fig. 7.3a). To eliminate this we systematically explored a broad range of throttle pressures, gas compositions, substrate temperatures and plasma powers during a-Si:H deposition, but continued to find persistent nanocrystallisation. As a result we next investigated the use of a buffer layer to allow smooth deposition. A range of materials were investigated including a thin layer of evaporated chromium and an adsorbed monolayer of APTMS ((3-aminopropyl)-trimethoxysilane, Fig. 7.3b). Chromium led to smooth coatings but was found to severely quench the plasmonic response of nanovoids; APTMS coatings resulted in non-uniform deposition of silicon over the sample.

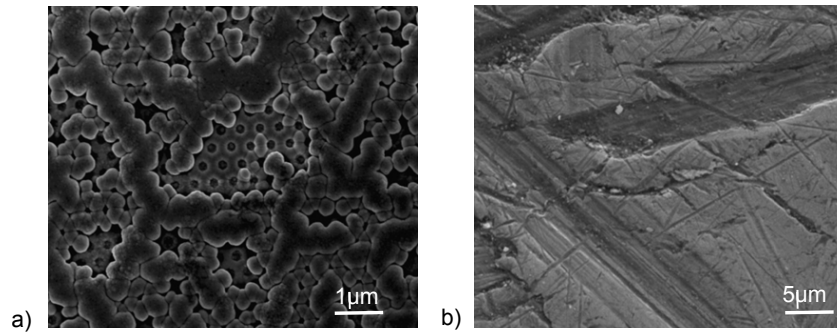


Figure 7.3: a) Amorphous silicon solar cell fabrication directly on Au nanovoids showing nanocrystallisation of a-Si:H and subsequent uneven ITO coating. The unconformal deposition without a buffer layer results in shorted cells. b) a-Si:H deposited on an APTMS monolayer adsorbed onto a flat Au substrate.

A suitable buffer layer was found in aluminium-doped zinc oxide, deposited via RF magnetron sputtering (Al:ZnO, 1-99% wt, Testbourne Ltd.). Aluminium doped zinc oxide is highly transparent in the visible spectrum and at 1-99% wt doping ratio has resistivity of $< 10^{-3} \Omega\text{cm}^{-1}$ and carrier concentrations in excess of 10^{20}cm^{-3} . It is an ideal material for the spacer layer in a-Si:H solar cells and supports conformal coating (Fig. 7.4). Thicknesses of $\delta_{AZO} = 30, 100$ and 200 nm were sputtered onto each substrate and overcoated with 50 nm of a-Si:H (15 nm n-type, 35 nm i-type) via plasma-enhanced chemical vapor deposition (RF Plasmalab μP), before RF sputtering 80 nm of indium tin oxide (ITO) as the top contact. Gradual smoothing of nanoscale features is observed with increasing layer thickness (Fig. 7.4). External quantum efficiency (EQE) measurements are performed using a 250 W tungsten halogen lamp (Newport, Simplicity QTH) dispersed through

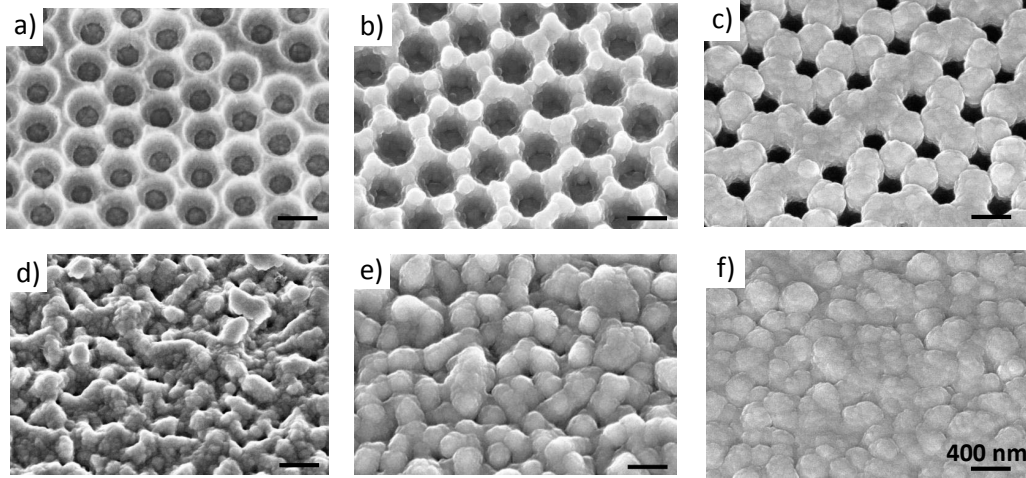


Figure 7.4: (a,d) Scanning electron micrographs of silver nanovoids (top) and silver coated Asahi glass (bottom) with plain silver (a,d), 30 nm of Al:ZnO and 50 nm of a-Si:H (b,e), and 200 nm of Al:ZnO and 50 nm a-Si (c,f).

a monochromator (Oriel Cornerstone 130) used with a filter wheel to block higher spectral orders. Current is measured with a Keithley 2635 source measure unit. Short-circuit current density measurements are obtained via integrating the external quantum efficiency response: $J_{sc} = \int N(\lambda) \times EQE(\lambda) d\lambda$, with $N(\lambda)$ the photon flux of the AM 1.5 G spectrum. J_{sc} measurements are further separated for wavelengths above and below 600 nm to elucidate detail from short and near band-gap edge regions of the spectrum.

7.3 Geometry

7.3.1 Nanovoids

We first examine the optical modes of the nanovoid cells in angle-resolved reflectance with the goniometer described in Chapter 5. The light source is a supercontinuum white-light laser (Fianium, $\lambda = 410 - 1500$ nm), and measurements are normalised to a flat silver mirror.

With 30 nm coating of aluminium doped zinc oxide (Al:ZnO), we can identify distinct plasmonic modes with Mie theory [22] that red-shift due to the higher refractive index compared to air (Fig. 7.6a compared to 7.5a). These

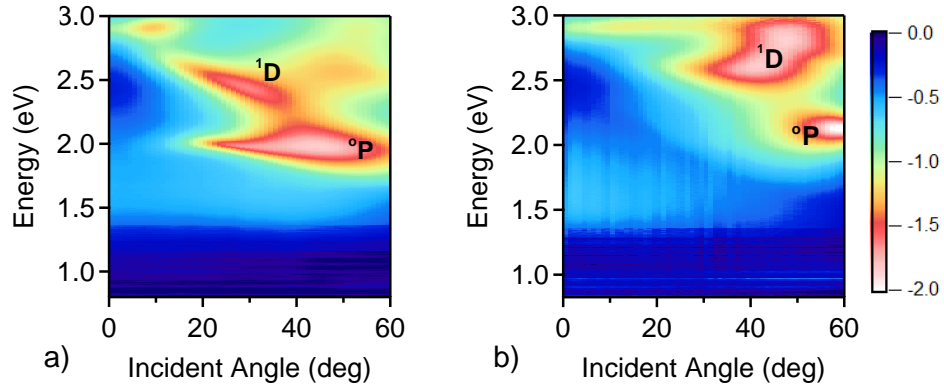


Figure 7.5: Angle reflectance measurements of silver nanovoids of 250 nm radius in a) TM and b) TE polarisation. Color scale is $\log(\text{reflectance})$ with blue indicating high reflectance and red-white indicating low reflectance. Modes are labelled according to [22].

resonances retain sharp linewidths and high intensities indicating strong confinement and long plasmon lifetimes which prove significant in the contribution to active semiconductor absorption in the a-Si coated device, discussed further below. Higher-order modes tune into the visible spectrum for 200 nm of Al:ZnO coating (Fig. 7.6b,d) alongside interaction with standing wave modes within the curved Al:ZnO cavity.

Optical absorption modes of nanovoids coated with the complete cell structure of Al:ZnO/a-Si/ITO exhibit strong dependence on the thickness of the spacer layer. Bragg-scattering surface plasmon modes in TM (black lines in Figure 7.6e) alongside photonic crystal like modes (white lines) arising from the hexagonal lattice of nanovoids are present in the solar cell with thin Al:ZnO coating [20]. Strong extinction is observed for energies $> 2.3 \text{ eV}$ owing to both scattering from the structure and absorption in the metal layer. For solar cells with thick Al:ZnO coating the absorption is dominated by non-dispersive localised plasmon modes within the voids structure (Fig. 7.6f,h), where the broad spread of each mode in wavevector (angle) shows localisation in real space.

These optical interactions within the device manifest in the electrical response of the solar cells (Fig. 7.7). Whereas optical extinction includes scattering, parasitic absorption in the metal and photocurrent generated in the active semiconductor, spectrally-resolved *electrical* measurements highlight

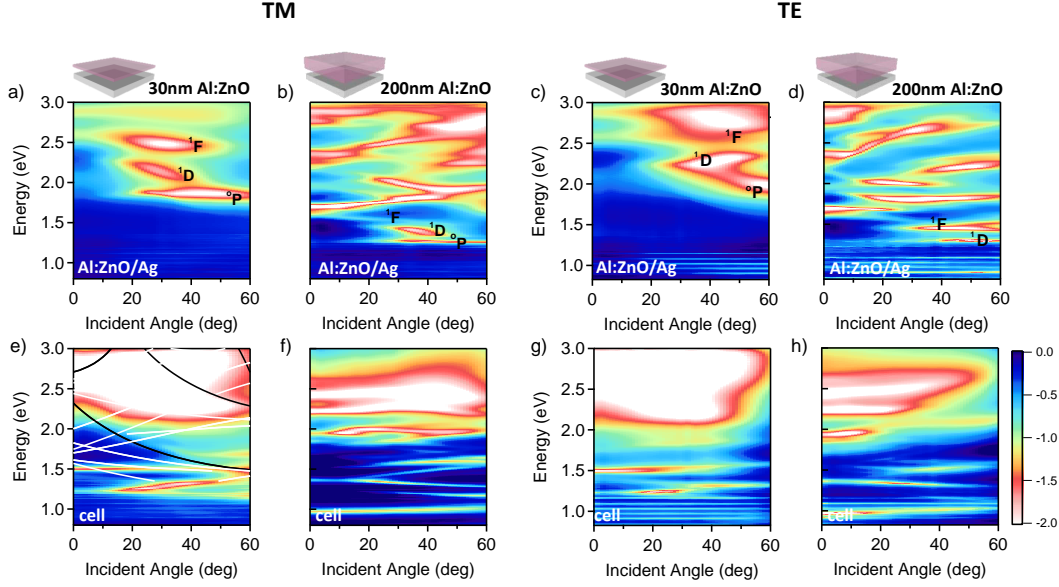


Figure 7.6: Angle reflectance of Ag nanovoids coated with Al:ZnO (top) and complete cell layers (bottom) in TM (left) and TE (right). Labelling discussed in text.

the optical modes that contribute directly to enhanced efficiency.

From the reduction in optical extinction at high-energies alongside the corresponding increase in extracted photocurrent (Fig. 7.7a), we infer that parasitic absorption in the silver substrate for 30 nm Al:ZnO coated cells is reduced once the Al:ZnO spacer thickness increases to 100 nm, in agreement with measurements on thin Ag gratings [94], causing the sharp doubling of J_{sc} from 3 to 6 mAcm^{-2} . The enhancement is primarily produced at shorter wavelengths where the tightly-confined localised surface plasmon resonances (LSPRs) are allowed to occupy more of the nanovoid cavity. The vertical surface plasmon decay length for a flat Ag/Al:ZnO interface ($|k_z|^{-1}$ where $k_z = \sqrt{k_{||}^2 - \epsilon_{AZO}(\frac{\omega}{c})^2}$) is 90 nm for light of 600 nm wavelength and hence, for the 30 nm Al:ZnO coated cell, the plasmon mode still strongly overlaps with the a-Si:H layer. Here, $k_{||}$ is the surface plasmon wavevector and ϵ_{AZO} is the dielectric function for Al:ZnO. For amorphous silicon this overlap leads to significant absorption in the silver layer and hence suppressed photocurrent at shorter wavelengths, further discussed in Section 7.5.

We find the main effect of localised plasmons in silver nanovoids with

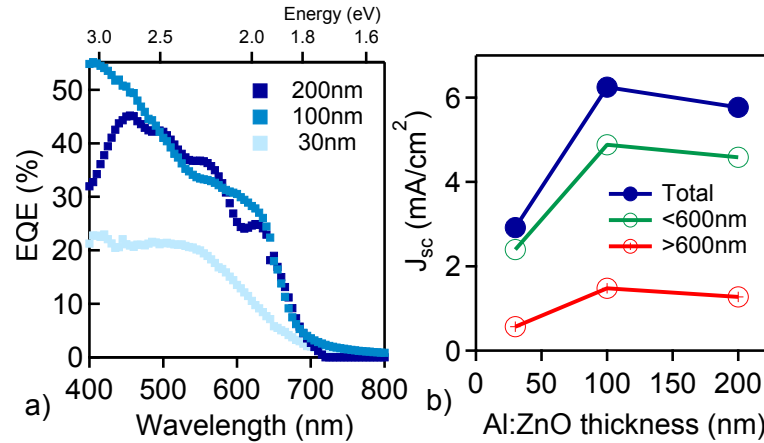


Figure 7.7: a) EQE measurements for a-Si:H nanovoid solar cells with varying spacer thickness. b) Short-circuit current density for nanovoids cells versus Al:ZnO thickness, decomposed for $\lambda < 600$ nm and $\lambda > 600$ nm.

30 nm of spacer layer to be quenching of optical modes leading to absorption in the metal. With 100 nm of the Al:ZnO spacer layer, the optical thickness of the entire device (now 560 nm) is able to support modes that are a mix between localised plasmons and standing-wave modes within the cavity. The good overlap of this field profile with the active semiconductor layer contributes to the strong increase in J_{sc} . With 200 nm of Al:ZnO, less absorption is present between 1.5-2 eV and above 2.5 eV (Fig. 7.6f,h). This decrease in overlap of optical mode with the absorption spectrum of the a-Si layer especially for shorter wavelengths is responsible for the decrease in photocurrent within the device (Fig. 7.7a).

7.3.2 Randomly textured

Silver-coated randomly textured glass displays the broad plasmonic resonances expected from an agglomeration of silver nanoparticles of assorted size between 50-200 nm (Fig. 7.8). The resonances red-shift from the quasi-static dipole peak for silver nanoparticles at 400 nm (3.1 eV), and broaden when coated with 30 nm of Al:ZnO (Fig. 7.9a,c) due to its higher refractive index. When coated with a-Si:H and ITO layers, the 30 nm Al:ZnO cell shows further red-shift and broadening of the localised resonances along with absorption from the a-Si layer (Fig. 7.9e,g). For the textured silver coated with 200 nm of Al:ZnO distinctly different reflectance response is observed with

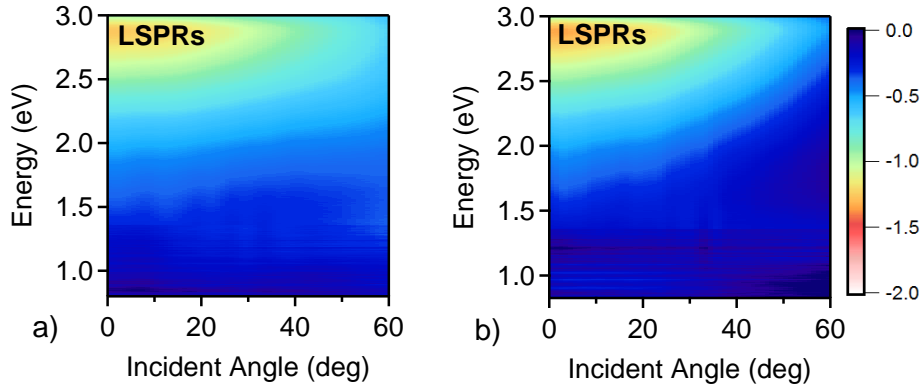


Figure 7.8: Angle reflectance measurements of silver coated Asahi glass with a) TM and b) TE polarisation. Labelling discussed in text.

strong extinction at Fabry-Perot (FP) resonance $\lambda = 2n\delta_{AZO}$ (Fig. 7.9b,d), where n and δ_{AZO} are the refractive index and thickness of the Al:ZnO layer. When coated with cell layers (Fig. 7.9f,h) this increased optical thickness enables the plasmonic resonances of the textured silver to resonantly scatter light in-plane within the device. The longer optical path lengths arising from this scattering accounts for the difference between the Asahi and flat cells.

These optical features again manifest in the electrical response of each cell. For the 30 nm Al:ZnO cell, localised surface plasmon resonances (LSPRs) arising at the tips and cavities of the textured silver substrate generate absorption in the silver layer (shown by the large absorption at short wavelengths, but low EQE), suppressing the photocurrent for shorter wavelengths similarly as for the nanovoid solar cell (Fig. 7.10a). As the spacer thickness increases to 100 nm and the silicon layer spatially moves away from the strong near-field at the Ag/Al:ZnO interface, the increased optical thickness now supports scattering in-plane generating enhanced absorption across the spectrum and contributing to a 30% increase in photocurrent from 5.2-6.7 mA/cm².

With 200 nm of Al:ZnO further enhancement to scattered optical path lengths is supported, with field-profiles that overlap with the a-Si layer both spatially and spectrally at approximately 2 eV, as shown with finite-difference time-domain simulations in Section 7.4.1. This field profile generates increased photocurrent within the device (Fig. 7.10b) to 7.9 mA/cm², 50%

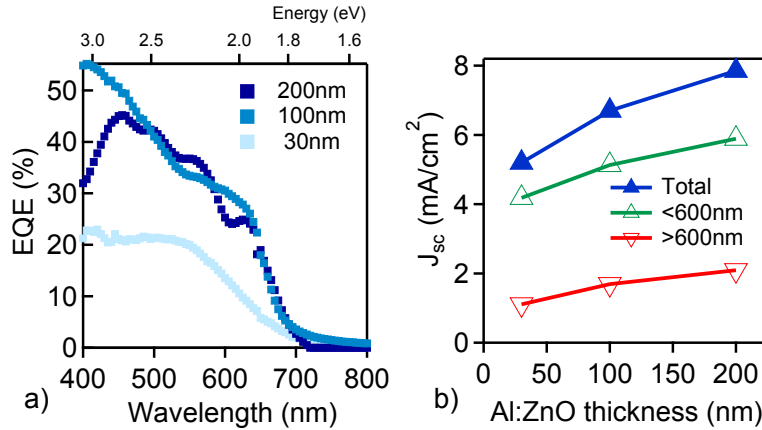


Figure 7.10: a) EQE measurements for a-Si:H Asahi solar cells with varying spacer thickness. b) Short-circuit current density for nanovoids cells versus Al:ZnO thickness, decomposed for $\lambda < 600$ nm and $\lambda > 600$ nm.

with non-absorbing cladding layers [134].

7.3.3 Flat

Whilst a practical reference architecture for industry is solar cells fabricated on randomly textured metal, cells fabricated on flat silver provide a baseline for device performance unassisted by both plasmon near-field and enhanced scattering. As expected, angle resolved reflectance of flat silver coated with 30 nm of Al:ZnO (Fig. 7.11a,c) shows little change from flat silver, with the 200 nm coated silver (Fig. 7.11b,d) showing the faint onset of Fabry-Perot (FP) resonance at 2.6 eV.

The spectral overlap of the FP resonance with the absorption spectrum of a-Si proves important for producing sufficient absorption in the ultrathin a-Si layer. The strong absorption at 2.7 eV (460 nm) due to the FP resonance at short wavelengths (Fig. 7.11e,g) for the 30 nm coated cell is the reason for the major contribution to J_{sc} of light with $\lambda < 600$ nm (Fig. 7.12b). As the spacer layer thickness increases to 100 nm, the FP resonance peak shifts spectrally towards the red whilst spatially being now located inside the a-Si layer (see Section 7.4.1), contributing to a 25% increase in photocurrent from 4.2-5.3 mA/cm². From EQE measurements (Fig. 7.12a) we see the spectral position of the FP peak red-shifts out of the region of strong absorption from a-Si:H at shorter wavelengths. Alongside the spectral overlap, the *spatial*

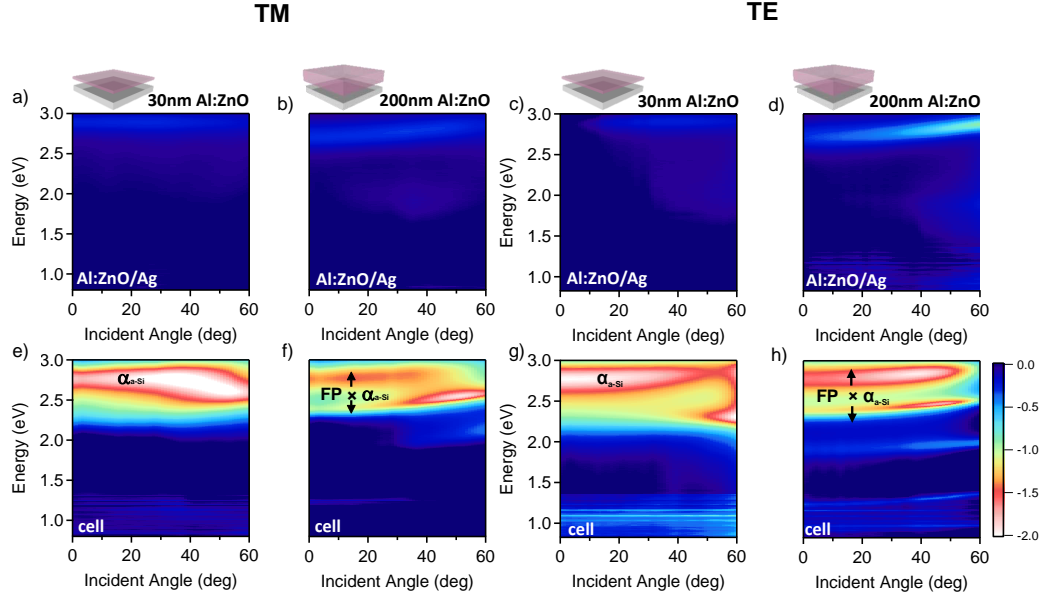


Figure 7.11: Angle reflectance of flat silver coated with Al:ZnO (top) and complete cell layers (bottom) in TM (left) and TE (right). Labelling discussed in text.

overlap of the field profile with the absorbing layer proves important, and we observe this via FDTD simulations discussed below.

7.4 Discussion

7.4.1 Simulations

We find the role of the spacer layer to vary for each cell geometry. FDTD simulations [116] highlight the changing field profiles across each device with changing spacer thicknesses (Fig. 7.13). Simulations are in 3D, dielectric constants for Ag [31], Al:ZnO [135], a-Si:H [95] and ITO [95] are taken from the literature. We present field profiles for $\lambda = 600$ nm to serve as a qualitative representative of optical profiles within each device. Finite difference time-domain simulations are undertaken with Lumerical FDTD Solutions software. Surface parameters for the randomly textured silver profile are imported from AFM measurements. Illumination is via a plane wave at normal incidence. The simulated region is $2 \mu\text{m}^2$ in area, boundary conditions are perfectly matched (100 layers) in the z direction and periodic in x, y .

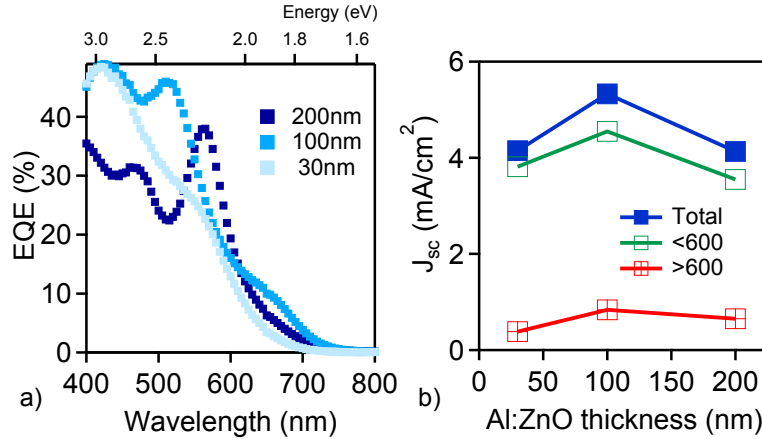


Figure 7.12: a) EQE measurements for a-Si:H flat solar cells with varying spacer thickness. b) Short-circuit current density for nanovoids cells versus Al:ZnO thickness, decomposed for $\lambda < 600$ nm and $\lambda > 600$ nm.

Though the introduction of periodic boundary conditions is not physical for randomly textured surfaces, having illumination at normal incidence, a large simulation area, and with reference to previous modelling [64], the errors arising from this assumption are expected to be $< 5\%$. For nanovoid cells, increasing the spacer thickness changes the localised plasmon profile within the device. For thin spacer thickness (Fig. 7.13i), weak excitation of plasmon field is observed with the strongest localisation found for Al:ZnO thickness of 100 nm (Fig. 7.13ii). With 200 nm of Al:ZnO (Fig. 7.13iii), the resonant field is again reduced in strength, qualitatively matching the response found in photocurrent (Fig. 7.7). For each void geometry the field profile is strongly tethered to the surface and has only weak overlap with the amorphous silicon layer. This contrasts with the field profiles found previously for organic solar cells fabricated in silver nanovoids (Chapter 6 and [125]), highlighting the strong material dependence on plasmon absorption enhancement via the near-field, discussed further in Section 7.5.

Asahi cells retain strong field enhancements for each spacer layer (Fig. 7.13iv-vi). For 30 nm spacing, strong fields are observed across the Ag/Al:ZnO interface. For 200 nm spacing we see more localised field at the metal interface, but also an increase of field inside the a-Si:H layer with optical nulls either side in the lower- n ITO and Al:ZnO layers (Fig. 7.13vi). This guided mode profile agrees with photocurrent measurements (Fig. 7.10) and the

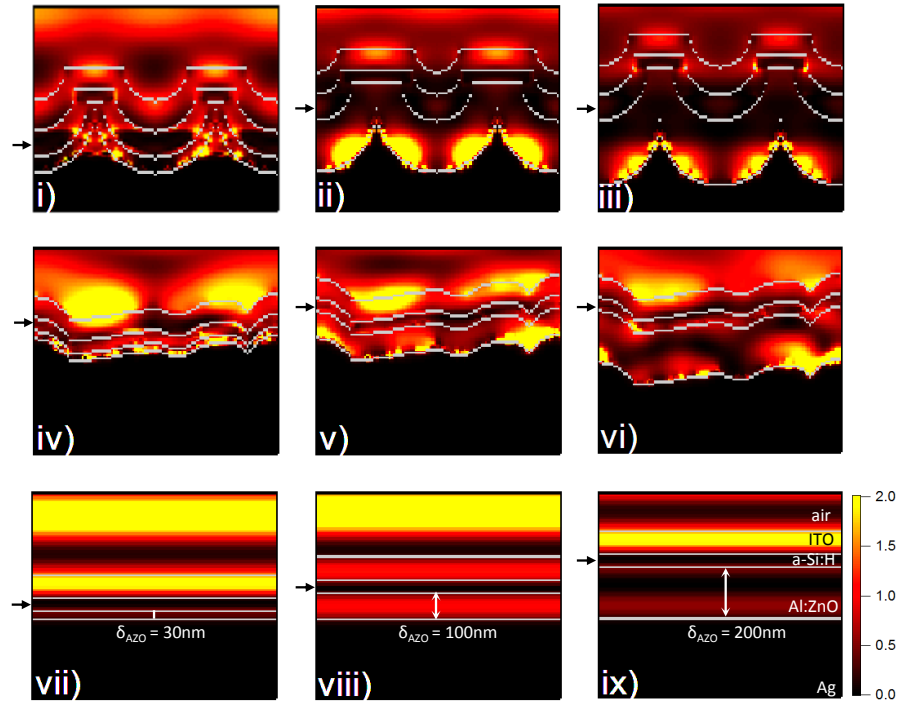


Figure 7.13: FDTD simulations of $|E|^2$ intensity at 600 nm with increasing Al:ZnO spacer thicknesses of 30,100 and 200 nm (left to right) for (i-iii) nanovoids, (iv-vi) Asahi and (vii-ix) flat solar cells. Arrows mark the position of the a-Si:H active layer.

strong field in the a-Si:H layer highlights the role of scattering when compared with the null observed in the a-Si:H layer for the flat cell with same spacer thickness (Fig. 7.13ix). Field profiles for flat cells show minimal overlap with the a-Si:H layer at 600 nm, highlighting the need for scattering features to couple incoming light to guided modes within the higher- n layer.

7.4.2 Spectral analysis

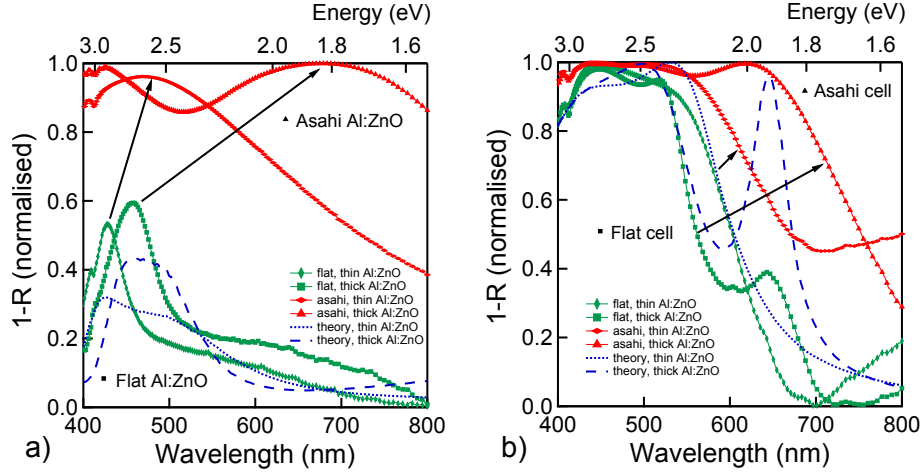


Figure 7.14: Extinction = (1-Reflectance) spectra for flat and Asahi substrates coated with a) Al:ZnO and b) additional cell layers. Transfer matrix calculations (blue lines) show the position of Fabry-Perot peaks for flat substrates. Arrows mark the shift in peak extinction wavelength, indicating the increased path length for Asahi substrates.

The effect of scattering features on absorption is observed through normal-incidence extinction measurements (Fig. 7.14) of Asahi and flat cells. Peaks of absorption in Al:ZnO coated flat silver broaden and red-shift when deposited on the randomly textured substrate (Fig. 7.14a), showing the detuning of LSPRs. For the complete cell structure (Fig. 7.14b), both substrates retain a FP type spectral profile with the Asahi substrate displaying both stronger and broader absorption. This is explained by the Asahi substrate providing scattering in multiple directions, allowing a broad range of optical paths that couple to trapped modes within the a-Si:H which is clad with the lower- n layers of ITO and Al:ZnO. EQE spectra for solar cells with 200 nm Al:ZnO spacer layer (Fig. 7.15) reveal characteristics for each physical process. Scattering from localised plasmons and FP resonances which couple to guided modes result in enhanced optical path lengths within the device, contributing to increased photocurrent across the spectrum for Asahi cells. The sharper localised plasmon resonances of nanovoid cells (Fig. 7.6f,h) are visible in the EQE spectrum, though little photocurrent is observed at short (<450 nm) wavelengths. This is the primary cause of the reduced J_{sc} of the nanovoids compared to the Asahi cells. EQE spectra of the flat solar cell

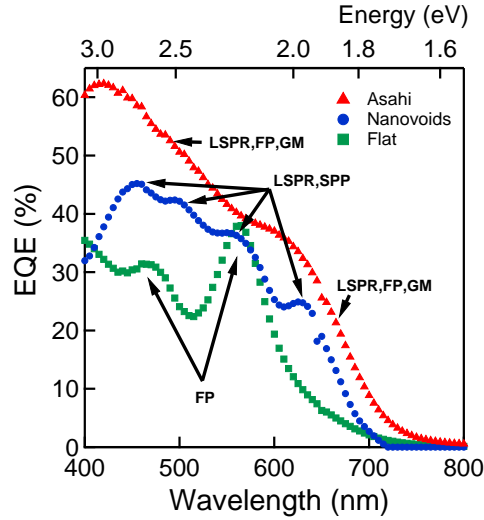


Figure 7.15: External quantum efficiency of a-Si solar cells fabricated with 200 nm of Al:ZnO on Asahi VU type glass, Nanovoids, and Flat silver substrates. LSPR = localized surface plasmon resonance, FP = Fabry-Perot resonance, GM = Guided mode.

highlight the importance of matching FP modes spatially with the active absorbing layer for ultrathin devices. With the 50 nm thickness of the a-Si layer being much less than the absorption length (190 nm at $\lambda = 600$ nm) and in the absence of in-plane coupling, photocurrent generation relies significantly on light-trapping within the active absorbing layer (Fig. 7.12b). The dependence on scattering geometry is apparent when we compare the effect of spacer layer thickness for each device type (Fig. 7.16). With broad scattering resonances, randomly textured glass benefits monotonically from increased spacer layer thicknesses. The optimum thickness for this ultrathin device expected when decreasing charge-collection due to the thick Al:ZnO layer counteracts the optical enhancement gained from greater scattering into guided modes. Nanovoid cells with strong narrow plasmon resonances generate absorption in the Ag for shorter wavelengths suppressing photocurrent for thin Al:ZnO thicknesses. Optimum photocurrent arises for 100 nm Al:ZnO when the spatial distribution of plasmon modes overlaps most with the a-Si:H layer. For 200 nm spacers the narrow linewidths of the plasmon coupled modes now red-shift below the region of strong a-Si absorption, resulting in reduced photocurrent from shorter wavelengths and lower J_{sc} . The effect of Al:ZnO thickness on flat cells is to shift the spatial intensity distri-

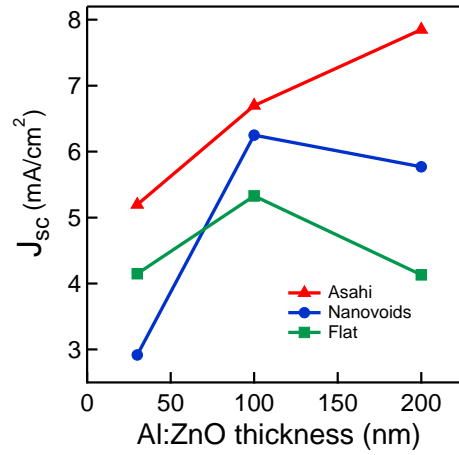


Figure 7.16: a) Short-circuit current density versus Al:ZnO thickness for each substrate.

tribution across the device. For 100 nm thickness, an FP peak in the a-Si:H layer contributes most to give maximum J_{sc} .

7.4.3 Geometry and curvature

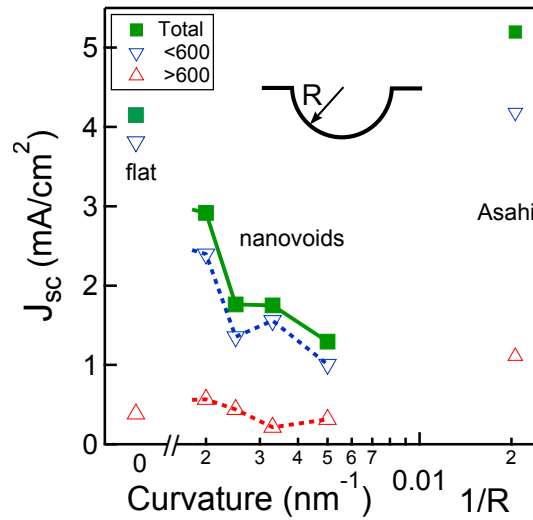


Figure 7.17: J_{sc} vs curvature for cells with 30 nm Al:ZnO on flat silver, nanovoids with radius 100, 150, 200 and 250 nm and silver-coated Asahi glass.

To examine the dependence of geometry on the effect of the near-field plasmon resonance, solar cells are fabricated on nanovoids with radii of 100, 150, 200 and 250 nm (Fig. 7.17), each with thin (30 nm) Al:ZnO layer. Angle

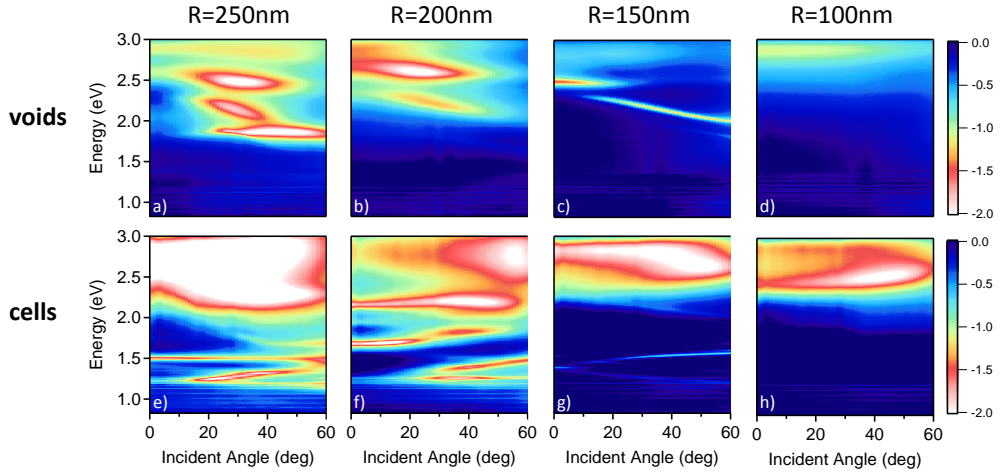


Figure 7.18: Angle reflectance scans of nanovoids with varying radius coated with 30 nm of Al:ZnO (top) and complete solar cell layers (bottom) in TM. Left to right: R=250 nm, 200 nm, 150 nm and 100 nm.

resolved reflectance shows the position of localised plasmon modes shifting to the visible for voids of increasing radius (right to left, top section Figure 7.18)[22]. For nanovoid cells (bottom section Figure 7.18) the spectral overlap of plasmonic effects with the region of a-Si:H absorption leads to enhanced photocurrent.

J_{sc} of each is plotted against the curvature of the voids ($1/R$) with flat and Asahi provided for comparison. Nanovoid J_{sc} decreases with increasing curvature (decreasing radius) of the nanovoid. That is, as the radius of the nanovoid decreases localised plasmon resonances are excited at higher energies [22] and are unable to generate enhanced photocurrent in the a-Si:H layer.

The effect of plasmonic geometry is found to be different for randomly textured silver. Asahi cells do not match the trend of reduced J_{sc} for increased curvature. This highlights a key optical difference between the confined localised plasmons of nanovoids and the plasmon-enhanced scattering of the Asahi substrate, with the scattering proving more beneficial for solar cells made with a-Si:H active layers.

7.5 Amorphous silicon near-field absorption

To understand the differences in plasmonic enhancement between these amorphous silicon solar cells and the organic solar cells of Chapter 6, we analytically examine the balance of absorption for the $|E|^2$ intensity field for surface plasmon polaritons at a planar interface between silver and an absorbing semiconductor. Using a simple expression comprising only dielectric functions of the materials we can identify the wavelength regions where the near-field is expected to contribute to absorption enhancement in the semiconductor and when it can be expected to lead to undesired absorption in the metal layer. This is a question that has not yet been resolved satisfactorily in the literature.

In Chapter 8 we analytically derive this result and discuss its implications for a wide range of photovoltaic materials. We present here the ratio for a-Si:H cells (Fig. 7.19) and observe decreasing semiconductor absorption both for short wavelengths (<500 nm) and longer wavelengths approaching the band-edge at 950 nm. This indicates that for a-Si:H solar cells, plasmonic substrates should be harnessed primarily for increased scattering and not near-field enhancement, since the metal strongly absorbs both short and long wavelengths where absorption is needed for the semiconductor. These two plasmonic mechanisms can be mediated via the thickness and refractive index of the spacer layer, with thicker high- n dielectrics suited for enhanced scattering, further discussed in Chapter 8.

7.6 Conclusions

Ultrathin amorphous silicon solar cells are fabricated with varying Al:ZnO spacer layers on two different plasmonic substrates alongside flat silver as a reference. Angle-resolved reflectance and photocurrent measurements allow identification of the coupling mechanisms of light with varying spacer layer, highlighting the importance of this separation of absorbing and plasmonic layers. A 20% enhancement in cell efficiency is observed for nanovoid solar cells compared to flat, but with optimisation of the spacer layer, randomly textured silver allows for an even greater enhancement of up to 50%. The coupling to optical modes is found to sensitively depend on substrate geome-

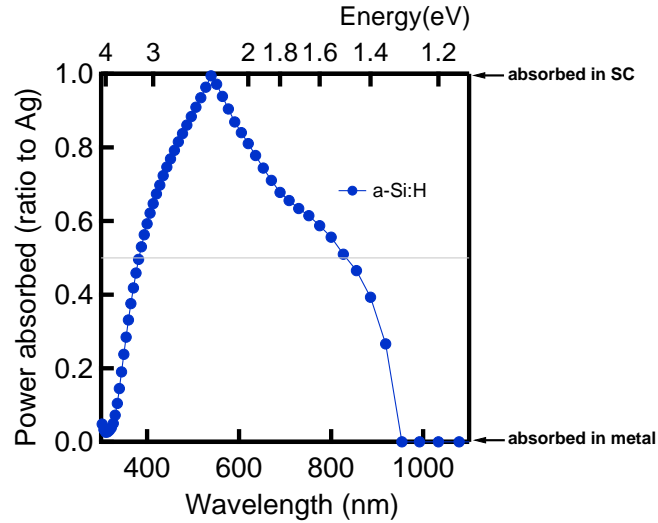


Figure 7.19: Ratio of power absorbed in a-Si:H to an Ag substrate with a surface plasmon polariton excited at the interface. A ratio of 1 corresponds to absorption purely in the semiconductor (SC), 0 to absorption in the metal.

try; the broad plasmonic resonances of silver-coated randomly textured glass benefit from larger optical thicknesses supporting enhanced scattering within the device.

Classical analysis of power absorbed at the interface between a metal and a dielectric provides guidance for choosing the role of a plasmonic rear surface for a-Si:H solar cells. Absorption in the metal substrate can be suppressed through the inclusion of a thicker high- n dielectric as the spacer layer, allowing greater coupling of plasmonic scattering to guided modes within the active layer. For ultrathin solar cells, controlling the Al:ZnO spacer thickness generates an increase in J_{sc} between 50-100%. The spacer is found to be a significant mediator between plasmonic excitation of the near-field, absorption in the metal and coupling to guided modes within the device, and identified to be a critical and useful parameter for device design.

We next discuss how the spacer can be utilised in thin film solar cells of varying materials alongside general design principles and candidate geometries for plasmon-enhanced photovoltaics.

Chapter 8

Design principles and ongoing research

This chapter discusses design principles for plasmonic solar cells and ongoing projects towards enhanced light trapping for photovoltaics. It begins with the analytical derivation of the absorption balance between a semiconductor and a metal with a surface plasmon excited at the interface. It then discusses this ratio for a wide range of leading photovoltaic materials and outlines design principles for plasmonic surfaces and dielectric spacers in thin-film solar cells. Section 8.3 presents solar cell geometries of ongoing and future research that use these design principles.

8.1 Plasmon absorption balance

Plasmonic structures are included in thin-film solar cells for two reasons: enhanced scattering of light into solar cell layers leading to longer optical path lengths, and enhanced optical near-fields leading to higher rates of charge-carrier generation in an adjacent semiconductor [16, 67, 136]. Metal nanostructures also contribute to parasitic absorption losses in solar cells [93, 94]. What has not yet been satisfactorily resolved in the literature is whether the scattering action of plasmonic nanostructures is to be preferred over exciting a strong near field in the adjacent active layer, or if plasmonic enhancement occurs via the same mechanism for various PV materials.

To address this question we analytically derive the ratio of absorption between a general absorbing dielectric and a metal when a surface plasmon

polariton is excited at the interface. This ratio gives valuable insight into the nature of plasmonic enhancement and allows clear identification of design principles for plasmonic photovoltaics. Consider an electromagnetic wave at

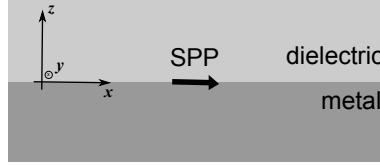


Figure 8.1: Plasmon geometry

the $z = 0$ plane travelling in the x direction with imaginary wavevector in the z direction. The $z = 0$ plane separates a dielectric ($\tilde{\epsilon}_1$) and metal ($\tilde{\epsilon}_2$) (Fig. 8.1). The general expression for the electric field is given:

$$\vec{\mathbf{E}} = (E_x, E_y, E_z) e^{i(\tilde{k}_x x + \tilde{k}_z z)} \tag{8.1}$$

with $Re(k_x)$ and $Im(k_z)$. For a surface plasmon propagating at the metal dielectric interface the wavevectors are $\tilde{k}_x = k_0 \sqrt{\frac{\tilde{\epsilon}_d \tilde{\epsilon}_m}{\tilde{\epsilon}_d + \tilde{\epsilon}_m}}$ and $\tilde{k}_{z_j} = \sqrt{k_0^2 \tilde{\epsilon}_j - \tilde{k}_x^2}$, with $k_0 = \frac{\omega}{c}$ (Chapter 2). We then identify each component of the electric field:

$$E_x = C_1 e^{i(\tilde{k}_x x + \tilde{k}_z z)} \tag{8.2}$$

$$E_y = 0 \tag{8.3}$$

$$E_z = iC_1 \frac{\tilde{k}_x}{\tilde{k}_z} e^{i(\tilde{k}_x x + \tilde{k}_z z)} \tag{8.4}$$

This allows calculation of the field intensity:

$$|\vec{\mathbf{E}}|^2 = (\tilde{\mathbf{E}} \cdot \tilde{\mathbf{E}}^*) \tag{8.5}$$

$$= C_1^2 \left(1 + \frac{|k_x|^2}{|k_{z_j}|^2} \right) e^{-2 Im(k_{z_j}) z} \tag{8.6}$$

By considering the expression for energy dissipation in a lossy medium $P = \int d\mathbf{r} 2\omega\epsilon_0 Im(\tilde{\epsilon}_j) |\vec{\mathbf{E}}|^2$ we can form the integral for power absorbed as a function of height:

$$P = \int d\mathbf{r} 2\omega\epsilon_0 Im(\epsilon_j) C_1^2 \left(1 + \frac{|k_x|^2}{|k_{z_j}|^2} \right) e^{-2 Im(\tilde{k}_{z_j}) z} \tag{8.7}$$

Integrating in the half-plane then yields the expression for plasmon absorption for each material:

$$P = \frac{\omega}{k_{z_1}^i} \epsilon_0 C_1^2 \text{Im}(\epsilon_1) \left(1 + \frac{|\tilde{k}_x|^2}{|\tilde{k}_{z_1}|^2} \right) \quad (8.8)$$

From which we obtain the ratio of absorption in a dielectric (d) to the metal (m):

$$\frac{P_d}{P_m} = \frac{k_{z_m}^i \text{Im}(\tilde{\epsilon}_d) (1 + |\tilde{k}_x|^2/|\tilde{k}_{z_d}|^2)}{k_{z_d}^i \text{Im}(\tilde{\epsilon}_m) (1 + |\tilde{k}_x|^2/|\tilde{k}_{z_m}|^2)} \quad (8.9)$$

8.2 Design principles

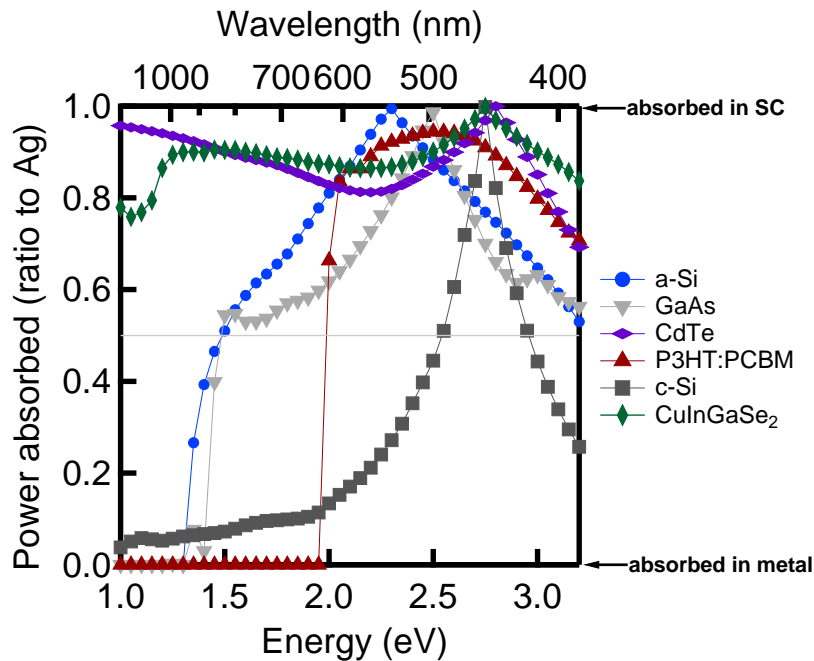


Figure 8.2: Ratio of power absorbed in various photovoltaic semiconductors (SCs) and silver with a surface plasmon polariton excited at the interface.

For solar cells with plasmonic surfaces adjacent to the rear of the semiconductor layer, a high absorption ratio close to the band-gap edge is desired. Since light of shorter wavelengths is preferentially absorbed near the front surface, plasmonic surfaces at the rear of the cell should be optimally designed to increase absorption of light of longer wavelengths near the band-gap edge

[63]. For ultrathin solar cells with thickness at or below the absorption depth, a high absorption ratio in the semiconductor is desired across the spectrum. For cells made on Ag substrates we see that each of a-Si:H, GaAs, and c-Si ratios show decreasing semiconductor absorption for both short wavelengths and longer wavelengths approaching their respective bandgaps (Fig. 7.19), crystalline silicon showing particularly strong parasitic metal absorption for much of the visible spectrum.

On the other hand, CdTe, CIGS and P3HT:PCBM are found to absorb more than $\sim 80\%$ of the plasmonic near-field across their absorbing spectrum. These results enable us to predict the materials for which plasmonic near-field excitation will be beneficial to absorption enhancement (CdTe, CIGS and organic polymers), and where plasmonic substrates should be harnessed more for increased scattering (a-Si:H, GaAs and c-Si).

It is instructive to place the plasmonic metal losses in context of the total optical losses for a cell without plasmonic structures. For thin devices fabricated with highly reflecting substrates (such as flat Al or Ag), metal absorption in the rear reflector is typically lower than 5%. However, the *total* reflection losses for thin devices - where conventional anti-reflective coatings are ineffective, alongside the weak absorption of semiconductors especially near the band edge are typically larger than 10% and hence warrant the inclusion of carefully designed plasmonic structures. The nature of optimum enhancement is seen to be sensitively dependent on semiconductor material - a feature previously not identified in the literature.

Both near-field and scattering enhancements can be mediated via the thickness and refractive index of the spacer layer. Thin low- n dielectrics are suited for near-field coupling, thicker high- n dielectrics allow enhanced scattering into guided modes by generating greater optical thicknesses.

The balance for crystalline silicon and GaAs indicate that structures should be as scattering as possible. For these crystalline wafer-based materials a simple array of nanoparticles deposited on the rear surface of the cell is expected to provide large enhancements, as confirmed in recent literature [62, 127]. Since amorphous silicon solar cells are not wafer-based they are able to be deposited on top of textured substrates, and hence can benefit from having the plasmonic structure as a rear electrode. With the plasmonic substrate required to be as scattering as possible, amorphous sili-

con solar cells are expected to benefit from deposition on randomly textured silver-coated glass such as those presented in Chapter 7. For near-field enhancement of solar cells we desire surface plasmons to be excited for as long as possible at wavelengths where the semiconductor absorbs weakly before re-radiating at another scattering object, allowing the semiconductor the greatest chance to generate a charge-carrier from the enhanced field. Nanovoids and nanogroove geometries are expected to be beneficial where they include smooth areas across which SPPs can propagate. The ongoing research into these structures is discussed in the next section.

8.3 Ongoing research

There are various ways the results presented in this thesis can be taken forward, we present three in this section: multiply-plasmonic and next-generation nanovoid cells, optimisation of random substrates, and silicon cells based on inverted-pyramid void structures.

8.3.1 Advanced nanovoid photovoltaics

Nanovoid geometries have shown four-fold enhancement for thin organic solar cells (Chapter 6) and have promising potential for CdTe and CIGS devices where near-fields can contribute strongly to enhanced absorption. For organic cells, developing techniques to fabricate a transparent top contact on nanovoid devices will allow further detailed probing of void geometry. It will also allow better the study of organic cells fabricated on randomly textured plasmonic substrates - a geometry not yet demonstrated in the literature. Candidate transparent electrodes include conducting polymers [83], Ag nanowire meshes [102, 103] and ITO sputtered at higher pressure, reducing the impact energy of molecules as they diffuse from the sputter target to the substrate. The optimisation of transparent electrodes is an ongoing research area for device electronics.

Nanovoids geometries also allow the fabrication of multiply-plasmonic structures and show potential for third generation PV, concepts that we describe as ‘advanced nanovoid photovoltaics’.

Evaporating plasmonic metals at high incident angles onto semiconductor-

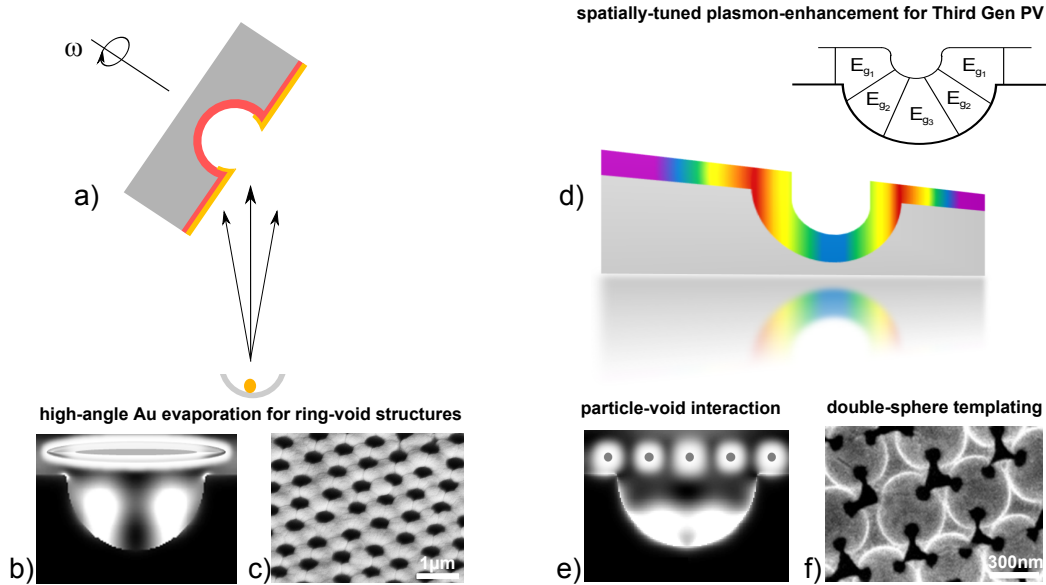


Figure 8.3: a) Geometry for the fabrication of a ring array on the top of nanovoids via high-angle evaporation. b) Schematic illustration of the field in ring-void structures. c) SEM of a gold ring-array on top of silver nanovoids separated by a dielectric. d) Schematic for spatial separation of wavelengths in nanovoids for Third Generation PV. e) Illustration of fields for nanovoid-particle structures. f) Three-fold symmetric Au structures formed by electroplating through double-layer templates of nanospheres.

coated nanovoids forms an interconnected array of plasmonic rings on the rims of nanovoids that can also serve as the top contact for the device (Fig. 8.3a, b, c). Extraordinary transmission of light through sub-wavelength holes was one of the first experiments that led to the modern field of plasmonics [17], and there is considerable potential for interaction between these holes and the strong fields inside nanovoids.

With collaborators at the University of Southampton, we have previously examined the effect of multiple plasmonic structures for enhanced SERS, finding an increase of two orders of magnitude in signal at molecular resonance when Ag nanoparticles (with average radius of 9 nm) are deposited on the surface of 300 nm radius gold nanovoids [137]. Strong field enhancements are similarly expected for nanovoid solar cells with plasmonic particles placed on the front surface (Fig. 8.3e).

Further novel geometries to explore with nanovoids include the intricate three-fold symmetric structures formed via electroplating through a double layer of close-packed spheres. Figure 8.3f shows gold structures where the self-

assembly of latex spheres has led to a double-layer of close-packed spheres. Subsequent electrodeposition of Au grows around the first layer of spheres (as for normal nanovoids), and then continues to grow around the second layer with intricate three-fold symmetric templating provided by the underlying sphere layer. Exciting possibilities for novel PV design lay with multi-step electrodeposition of gold or silver (to form nanovoids around the first sphere layer), with CdTe PV layers subsequently electroplated around the second sphere. This geometry provides optical enhancement from the nanovoids with a rear contact geometry that is templated by the first layer of spheres.

The final concept for nanovoids that we outline here is their application for spatial *and* spectrally-resolved plasmonic enhancement, first introduced in Chapter 6. Whilst prisms and diffraction gratings spatially disperse light with ease, they do so with structures much larger than the wavelength of light. Separating colours in the *sub*-wavelength regime is significantly more difficult. Silver nanovoids display varying spatial distribution for different localised plasmon resonances within the void geometry (conceptual illustration in Figure 8.3d). These spatial distributions have been extensively studied by our group [22] and are understood through the framework of Mie resonances and spherical harmonics within the cavity; they provide a unique method of spectrally separating colours in the sub-wavelength regime. By matching semiconductor materials to the specific locations of plasmon resonance for each wavelength range, absorption enhancement can be selectively targeted for each material bandgap. Multiple quantum well cells or the selective contacts of hot-carrier cells would have enhanced absorption of each wavelength occurring precisely at the optimal location in the device (Fig. 8.3d). Whilst the material control required to fabricate such devices is in the far future and only speculative at this time, we identify here one of the first possible concepts to separate colour with subwavelength structures, suggesting a possible route towards absorption enhancement for devices with thicknesses on the nanometre scale and efficiencies beyond the Shockley-Queisser limit.

8.3.2 Optimising random textures

Asahi VU type glass (Chapter 7) is a commercially available substrate with known roughness and serves as a quantitative, reproducible representative of

a randomly textured plasmonic surface. Previous research has investigated rough silver substrates with either thin Al:ZnO coatings only [138, 139] or no overlying cell layers [140], parameters we have found to be critical for determining the coupling of optical modes. Future work will systematically explore the size, sharpness and density of scattering features on a plasmonic substrate (Fig. 8.4) with varying thicknesses of the overcoated dielectric spacer. This can be readily achieved both experimentally and computation-

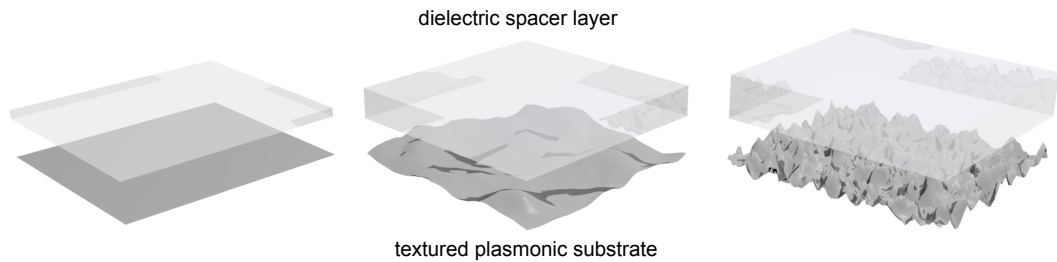


Figure 8.4: Illustration of plasmonic substrates with varying roughness and spacer layer thicknesses for the optimisation of plasmonic-enhanced scattering.

ally. Using Asahi VU-type glass as a template, we can either etch the glass before silver deposition or additionally deposit larger thicknesses of silver to gradually smooth the scattering features before depositing varying thicknesses of a dielectric spacer. In simulation the smoothing can be achieved simply by artificially broadening the surface profile in Lumerical calculations. These investigations in concert will serve as a valuable guide for the tailoring of plasmonic substrates for amorphous silicon solar cells and are ongoing.

8.3.3 Pyramid plasmonics for silicon PV

The metal-coated randomly textured surfaces outlined above are suitable substrates for amorphous silicon solar cells, but cannot be similarly applied to crystalline wafer-based materials that are more constrained in the range of available surface geometries. What can be achieved with crystalline silicon however, is the etching of pyramidal and honeycomb structures [141, 142]. Chemically etching the (100) surface of silicon to expose the (111) crystal faces results in pyramidal surfaces; by defining a square mask before the etch a regular array of pyramids can be formed. Gold-coated *inverse* pyramid structures (called Klarite™) have recently been investigated for plasmonic-enhanced Raman scattering, showing strong reproducible enhancements of

Raman signals by factors of up to 10^6 (Fig. 8.5a) [21, 36].

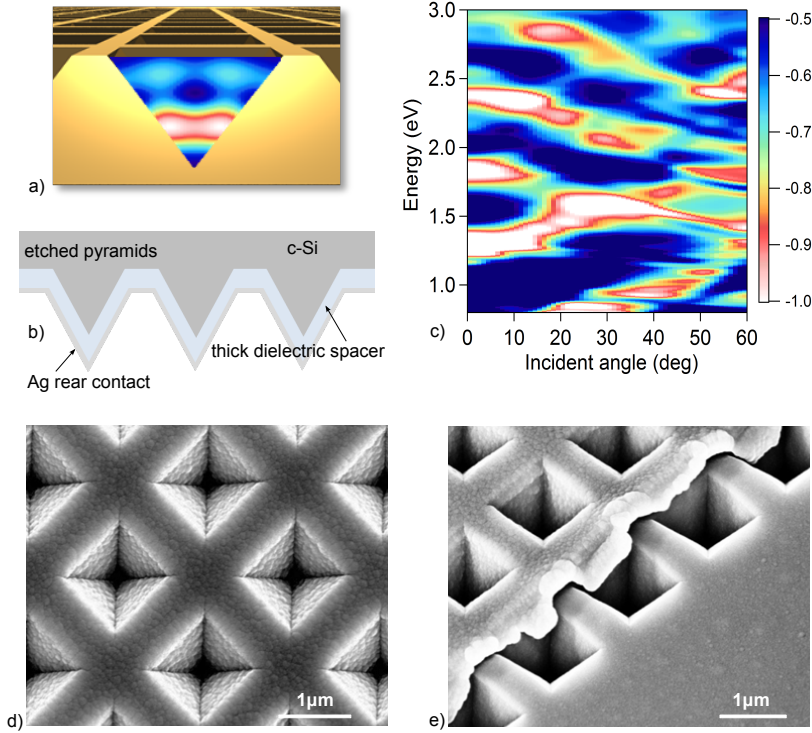


Figure 8.5: a) Illustration of Klarite with BEMAX modelling inside the pit. b) Schematic of pyramid plasmonics for c-Si cells. c) Angle-resolved reflectance of silver coated Klarite 1.4 μm pitch. (d,e) SEM of a-Si:H and ITO layers on Ag-coated Klarite. Klarite illustration adapted from [143].

We propose here a method for fabricating plasmonic substrates on the rear of crystalline silicon solar cells by pyramidally etching the silicon surface and overcoating with a thick dielectric spacer (SiO_2) and Ag (Fig. 8.5b). Pyramidal structures have had a long history of use in c-Si solar cells. Initially demonstrated in 1987 [141], they are still employed in today’s record efficiency 25.0% PERL crystalline silicon solar cells for light trapping on the front surface [9]. Plasmonic structures investigated for the *rear* of c-Si solar cells have typically been Ag nanoparticles [62, 63, 80, 144]. The fabrication of pyramidal plasmonic surfaces that additionally serve as the rear electrode of a thin crystalline silicon solar cell has exciting potential.

As a preliminary investigation we have fabricated amorphous silicon solar cells on top of silver-coated Klarite (Fig. 8.5d,e). Uncoated Klarite substrates were obtained from Renishaw Diagnostics Ltd and thermally evaporated with 150 nm of silver. Localised and Bragg plasmonic modes are observed in an-

gular reflectance from the silver structures (Fig. 8.5c) [36] and are expected to provide strong light-trapping enhancements via scattering into the overlying cell layers. These solar cells are the subject of ongoing research in collaboration with Renishaw Diagnostics.

8.4 Summary

The analytical expression for the balance of surface plasmon absorption between a semiconductor and metal yields practical design principles for thin film solar cells. Amorphous silicon, GaAs, and c-Si ratios show decreasing semiconductor absorption at both short and long wavelengths; crystalline silicon shows particularly strong parasitic metal absorption for much of the visible spectrum. CdTe, CIGS and P3HT:PCBM are found to absorb more than $\sim 80\%$ of the plasmonic near-field across the spectrum, maintaining high absorption ratio near the bandgap edge. These results enable us to predict the materials for which plasmonic near-field excitation will be beneficial to absorption enhancement (CdTe, CIGS and organic polymers), and where plasmonic substrates should be harnessed more for increased scattering (a-Si, GaAs and c-Si). This strong material dependence is a feature not yet established in the literature and can be mediated via the thickness and refractive index of the spacer layer.

Using design principles from this analysis, we describe three areas of ongoing research: advanced nanovoid PV concepts, optimising random surfaces concurrently with spacer thickness, and plasmonic pyramid structures for the rear contact of silicon solar cells.

Chapter 9

Conclusions

This thesis has explored the use of plasmonic nanovoids for enhancing thin-film solar cells. Cells were fabricated *within* plasmonically-resonant nanostructures, demonstrating a new class of plasmonic photovoltaics. With detailed consideration of the matrix of design parameters, novel cell geometries were developed for both organic and amorphous silicon solar cell materials (Chapter 4). An external-quantum efficiency rig was set up to allow simultaneous microscope access and micrometer-precision probe-tip control for optoelectronic characterisation of PV devices. An experimental setup for angle-resolved reflectance was extended to allow broadband illumination from 380 - 1500 nm across incident angles 0 - 70° giving detailed access to the energy-momentum dispersion of optical modes within nanostructured materials. Theoretical techniques were developed to examine optical field profiles within thin-film devices using a range of methods including boundary element simulations, finite-difference time-domain, and classical analysis (Chapter 5).

A four-fold enhancement of power conversion efficiency is observed in nanovoid organic solar cells compared to identically-prepared flat cells (Chapter 6), due largely to an increase in J_{sc} . Angle resolved reflectance shows clear excitation of surface plasmon resonance on plain silver nanovoids with the onset of localised modes present when coated with organic PV polymers. The efficiency enhancement in nanovoid cells is shown to be primarily due to these strong localized plasmon resonances of the nanovoid geometry, with close agreement in angle-resolved reflectance between experiment and theoretical simulations. Theoretical modelling suggests a mechanism for spatially separating colour with sub-wavelength plasmonic nanostructures.

Ultrathin amorphous silicon solar cells were fabricated with varying Al:ZnO spacer layers on nanovoids and randomly textured silver substrates alongside flat silver as a reference (Chapter 7). A 20% enhancement of cell efficiency is observed for nanovoid solar cells compared to flat, but with optimisation of the spacer layer, randomly textured silver allows for an even greater enhancement of up to 50%. The coupling to optical modes is found to sensitively depend on substrate geometry; the broad plasmonic resonances of silver-coated randomly textured glass benefit from larger optical thicknesses supporting enhanced scattering within the device. Angle-resolved reflectance and photocurrent measurements allow identification of the coupling mechanisms of light with varying spacer layer thickness, highlighting the importance of this separation of absorbing and plasmonic layers.

The analytical expression for the balance of surface plasmon absorption between a semiconductor and metal yields practical design principles for thin film solar cells (Chapter 8). Amorphous silicon, GaAs, and c-Si ratios show decreasing semiconductor absorption for higher energies and near their bandgap edge, with crystalline silicon showing particularly strong parasitic metal absorption for much of the visible spectrum. CdTe, CIGS and organic polymers are found to absorb more than $\sim 80\%$ of the plasmonic near-field across their absorbing spectrum. These results enable us to predict the materials for which plasmonic near-field excitation will be beneficial to absorption enhancement (CdTe, CIGS and organic polymers), and where plasmonic substrates should be harnessed more for increased scattering (a-Si:H, GaAs and c-Si). This strong material dependence can be mediated via the thickness and refractive index of the spacer layer.

Using the design principles gained from theoretical analysis, we describe three areas of ongoing research: advanced nanovoid concepts of multiple plasmonics and third generation plasmonic photovoltaics, optimising random surfaces concurrently with spacer thickness, and plasmonic pyramid structures for the rear contact of silicon solar cells.

For the 1.3 billion people in the world currently without access to electricity, it is hoped this research in some way contributes to the further development of a method of electricity generation that can be safe, cost-effective and environmentally sustainable.

List of publications

Journal articles

N. N. Lal, B. F. Soares, J. K. Sinha, F. Huang, S. Mahajan, P. N. Bartlett, N. C. Greenham, and J. J. Baumberg, “Enhancing solar cells with localized plasmons in nanovoids,” *Optics Express*, vol. 19, no. 12, pp. 3918–3924, 2011.

N. N. Lal, H. Zhou, J. K. Sinha, M. Hawkeye, P. N. Bartlett, G. A. J. Amaratunga, and J. J. Baumberg, “Using spacer layers to control metal and semiconductor absorption in ultrathin solar cells with plasmonic substrates,” *Physical Review B*, 2012, accepted, in press.

J. D. Speed, R. P. Johnson, J. T. Hugall, N. N. Lal, P. N. Bartlett, J. J. Baumberg, and A. E. Russell, “SERS from molecules bridging the gap of particle-in-cavity structures,” *Chemical Communications*, vol. 47, pp. 6335–7, June 2011.

R. B. Dunbar, T. Pfadler, N. N. Lal, J. J. Baumberg, and L. Schmidt-Mende, “Imprinting localized plasmons for enhanced solar cells,” *Journal of Applied Physics*, 2012, submitted

H. Butt, Q. Dai, N. N. Lal, T. D. Wilkinson, J. J. Baumberg, and G. A. J. Amaratunga, “Metamaterial filter for the near-visible spectrum,” *Applied Physics Letters*, 2012, submitted

T. S. Gershon, N. N. Lal, J. J. Baumberg, and J. L. MacManus-Driscoll, “Tuneable Mie-scattering from electrodeposited Cu₂O nanoparticles,” *Applied Physics Letters*, 2012, submitted

Invited presentations

N. N. Lal*, B. F. Soares, J. K. Sinha, F. Huang, S. Mahajan, P. N. Bartlett, N. C. Greenham, and J. J. Baumberg, *Optics Society of America Congress*, Karlsruhe, Germany, June, 2010

N. N. Lal*, B. F. Soares, J. K. Sinha, S. Mahajan, P. N. Bartlett, F. J. G. de Abajo, and J. J. Baumberg, *5th International Surface Plasmon Polariton Conference*, Busan, South Korea, May, 2011

Regular presentations

N. N. Lal, G. Christmann*, J. K. Sinha, F. Huang, S. Mahajan, P. N. Bartlett, N. C. Greenham, and J. J. Baumberg, *Conference on Lasers and Electro-Optics* San Jose, May, 2010

N. N. Lal, F. Huang*, J. K. Sinha, F. Huang, S. Mahajan, P. N. Bartlett, N. C. Greenham, and J. J. Baumberg, *Institute of Physics Photon 10*, Southampton, September, 2010

N. N. Lal*, B. F. Soares, J. K. Sinha, P. N. Bartlett, N. C. Greenham, and J. J. Baumberg, *UK Solar Energy Society Conference*, Edinburgh, March, 2011

N. N. Lal, F. Huang*, J. K. Sinha, F. Huang, S. Mahajan, P. N. Bartlett, N. C. Greenham, and J. J. Baumberg, *Conference on Lasers and Electro-Optics* San Jose, May, 2011

Public articles

N. N. Lal, “Finding the right energy level”, *British Science Association Quarterly*, Holbrooks, London, December, 2010

N. N. Lal, “Catching energy from the sun - how solar cells work”, *BBC Radio Naked Scientists*, Article online, bit.ly/catchingthesun, May, 2010

References

- [1] David JC Mackay, *Sustainable Energy Without The Hot Air*, UIT Cambridge Ltd, Cambridge, 2009. 2
- [2] World Bank, Population Indicator Data, data.worldbank.org/indicator, Washington, 2012. 2
- [3] International Energy Agency, World Energy Outlook, www.iea.org/weo/electricity.asp, Paris, 2012. 2
- [4] Organisation for Economic Co-operation and Development, OECD Factbook 2012, DOI:10.1787/18147364, Paris, 2012. 2, 3
- [5] Massachusetts Institute of Technology Energy Initiative Project, web.mit.edu/mitei/research/studies/index.shtml, Cambridge MA, 2012. 3
- [6] J. Painuly, Barriers to renewable energy penetration; a framework for analysis, *Renewable Energy* **24**, 73 (2001). 3
- [7] L. Weber, Some reflections on barriers to the efficient use of energy, *Energy Policy* **97**, 84 (1997). 3
- [8] US Department of Energy Information Administration 205.254.135.24/oiaf/aeo/electricity_generation.html, Washington, 2012. 4
- [9] M. A. Green, K. Emery, Y. Hishikawa, and W. Warta, Solar cell efficiency tables (version 37), *Progress in Photovoltaics: Research and Applications* **19**, 84 (2011). 4, 29, 104
- [10] A. de Vos, *Endoreversible Thermodynamics of Solar Energy Conversion*, Oxford University Press, Oxford, 1992. 4, 22, 26

- [11] Bushlight, Centre for Appropriate Technologies, www.bushlight.org.au, Alice Springs, 2012. 4
- [12] S. A. Maier, *Plasmonics: Fundamentals and Applications*, Springer, New York, 1 edition, 2007. 5, 9, 11, 12, 13
- [13] C. Kittel, *Introduction To Solid State Physics*, John Wiley and Sons, New York, 6 edition, 1986. 5, 23, 29, 47
- [14] H. Stuart and D. Hall, Absorption enhancement in silicon-on-insulator waveguides using metal island films, *Applied Physics Letters* **69**, 2327 (1996). 5, 35
- [15] S. Pillai, K. R. Catchpole, T. Trupke, and M. A. Green, Surface plasmon enhanced silicon solar cells, *Journal of Applied Physics* **101**, 093105 (2007). 6, 37, 38
- [16] K. R. Catchpole and A. Polman, Plasmonic solar cells, *Optics Express* **16**, 21793 (2008). 6, 17, 35, 36, 96
- [17] P. Ebbesen, W. Thomas, H. J. Lezec, H. F. Ghaemi, T. Thio, P. A. Wolff, Theory of extraordinary optical transmission through subwavelength hole arrays, *Nature* **391**, 667 (1998). 6, 101
- [18] S. Coyle et al., Confined Plasmons in Metallic Nanocavities, *Physical Review Letters* **87**, 15 (2001). 6, 18, 51
- [19] P. N. Bartlett, J. J. Baumberg, S. Coyle, and M. E. Abdelsalam, Optical properties of nanostructured metal films, *Faraday Discussions* **125**, 117 (2004). 6, 18, 51, 52
- [20] T. Kelf et al., Localized and delocalized plasmons in metallic nanovoids, *Physical Review B* **74**, 1 (2006). 17, 18, 19, 53, 70, 72, 78, 81
- [21] N. Perney et al., Tuning localized plasmon cavities for optimized surface-enhanced Raman scattering, *Physical Review B* **76**, 1 (2007). 20, 104
- [22] R. M. Cole et al., Understanding Plasmons in Nanoscale Voids, *Nano Letters* **7**, 2094 (2007). 6, 18, 19, 53, 62, 70, 71, 78, 80, 81, 93, 102

- [23] Notre-Dame Cathedral, en.wikipedia.org/wiki/File:GothicRayonnantRose003.jpg, 2012. 9
- [24] R. Wood, Anomalous diffraction gratings, *Physical Review* **48**, 928 (1935). 9
- [25] G. Mie, Beitrage zur optik truber medien, speziell kolloidaler metallosungen, *Annalen der Physik* **330** (1908). 9, 16
- [26] R. Ritchie, Plasma losses by fast electrons in thin films, *Physical Review* **106**, 874 (1957). 9
- [27] J. M. Pitarke, V. M. Silkin, E. V. Chulkov, and P. M. Echenique, Theory of surface plasmons and surface-plasmon polaritons, *Reports on Progress in Physics* **70**, 1 (2007). 9, 14
- [28] A. Zayats, I. Smolyaninov, and A. Maradudin, Nano-optics of surface plasmon polaritons, *Physics Reports* **408**, 131 (2005). 9
- [29] H. Raether, *Surface Plasmons on Smooth and Rough Surfaces and on Gratings*, Springer-Verlag, Berlin, 1988. 9, 14, 15
- [30] M. Marder, *Condensed Matter Physics*, John Wiley and Sons, New York, 2000. 10
- [31] E. E. Palik, *Handbook of Optical Constants of Solids*, Academic Press, 3 edition, 1998. 13, 87
- [32] W. L. Barnes, A. Dereux, and T. W. Ebbesen, Surface plasmon sub-wavelength optics, *Nature* **424**, 824 (2003). 15
- [33] C. Bohren and D. Huffman, *Absorption and scattering of light by small particles*, John Wiley and Sons, New York, 1983. 16
- [34] P. N. Bartlett, J. J. Baumberg, P. R. Birkin, M. A. Ghanem, and M. C. Netti, Highly Ordered Macroporous Gold and Platinum Films Formed by Electrochemical Deposition through Templates Assembled from Submicron Diameter Monodisperse Polystyrene Spheres, *Chemistry of Materials* **14**, 2199 (2002). 18, 67

- [35] Y. Sugawara, T. Kelf, J. J. Baumberg, M. E. Abdelsalam, and P. Bartlett, Strong Coupling between Localized Plasmons and Organic Excitons in Metal Nanovoids, *Physical Review Letters* **97**, 1 (2006). 19
- [36] N. Perney et al., Tuning localized plasmons in nanostructured substrates for surface-enhanced Raman scattering, *Optics Express* **14**, 824 (2006). 20, 104, 105
- [37] R. Williams, Becquerel photovoltaic effect in binary compounds, *Journal of Chemical Physics* **32**, 1505 (1960). 21
- [38] D. Chapin, C. Fuller, and G. Pearson, A new silicon p-n junction photocell for converting solar radiation into electrical power, *Journal of Applied Physics* **25**, 676 (1954). 21
- [39] D. Bagnall and M. Boreland, Photovoltaic technologies, *Energy Policy* **36**, 4390 (2008). 21
- [40] Earth Policy Institute, <http://www.earth-policy.org/indicators/C47>, Washington, 2012. 21
- [41] A. Goetzberger, J. Luther, and G. Willeke, Solar cells: past, present, future, *Solar Energy Materials and Solar Cells* **74** (2002). 21
- [42] L. Tsakalakos, Nanostructures for photovoltaics, *Materials Science and Engineering R* **62**, 175 (2008). 21
- [43] M. A. Green, *Third Generation Photovoltaics*, Springer, New York, 2003. 21, 22, 26, 33
- [44] W. Shockley and H. Queisser, Detailed balance limit of efficiency of p-n junction solar cells, *Journal of Applied Physics* **32** (1961). 22
- [45] M. A. Green, *Third Generation Photovoltaics*, Springer, New York, 2003. 21, 22, 26, 33
- [46] W. Shockley and H. Queisser, Detailed balance limit of efficiency of p-n junction solar cells, *Journal of Applied Physics* **32** (1961). 22
- [47] S. Sze, *Semiconductor Devices, Physics and Technology*, John Wiley and Sons, New Jersey, 2002. 22, 23

- [48] J. Nelson, *The Physics of Solar Cells*, Imperial College Press, London, 2003. 23
- [49] S. Forrest, The path to ubiquitous and low-cost organic electronic appliances on plastic, *Nature* **428**, 911 (2004). 26
- [50] J. Clark and G. Lanzani, Organic photonics for communications, *Nature Photonics* **4**, 438 (2010). 26
- [51] J. H. Burroughes et al., Light-emitting diodes based on conjugated polymers, *Nature* **347** (1990). 26
- [52] B. W. D'Andrade and S. R. Forrest, White Organic Light-Emitting Devices for Solid-State Lighting, *Advanced Materials* **16**, 1585 (2004). 26
- [53] M. A. Green, K. Emery, Y. Hishikawa, W. Warta, and E. D. Dunlop, Solar cell efficiency tables (version 39), *Progress in Photovoltaics: Research and Applications* **20**, 12 (2012). 27
- [54] H. Hoppe and N. S. Sariciftci, Organic solar cells: An overview, *Journal of Materials Research* **19**, 1924 (2004). 27, 28, 56
- [55] L. J. Koster, V. D. Mihailetschi, and P. W. Blom, Ultimate efficiency of polymer/fullerene bulk heterojunction solar cells, *Applied Physics Letters* **88**, 093511 (2006). 27
- [56] B. Kippelen and J. L. Brédas, Organic photovoltaics, *Energy & Environmental Science* **2**, 251 (2009). 27
- [57] P. Peumans, A. Yakimov, and S. R. Forrest, Small molecular weight organic thin-film photodetectors and solar cells, *Journal of Applied Physics* **93**, 3693 (2003). 27
- [58] C. Brabec, *Organic Photovoltaics*, Springer, New York, 2003. 27, 56
- [59] T. Soderstrom, *Single and multijunction thin film silicon solar cells for flexible photovoltaics*, PhD thesis, University of Neuchatel, 2009. 29
- [60] R. Street, *Hydrogenated amorphous silicon*, Cambridge University Press, Cambridge, 1991. 29

- [61] C. Jiang et al., Distribution of the electrical potential in hydrogenated amorphous silicon solar cells, *Thin Solid Films* **472**, 203 (2005). 31
- [62] F. J. Beck, A. Polman, and K. R. Catchpole, Tunable light trapping for solar cells using localized surface plasmons, *Journal of Applied Physics* **105**, 114310 (2009). 31, 37, 99, 104
- [63] F. J. Beck, S. Mokkaapati, A. Polman, and K. R. Catchpole, Asymmetry in photocurrent enhancement by plasmonic nanoparticle arrays located on the front or on the rear of solar cells, *Applied Physics Letters* **96**, 033113 (2010). 31, 37, 66, 99, 104
- [64] V. E. Ferry, A. Polman, and H. A. Atwater, Modeling Light Trapping in Nanostructured Solar Cells., *ACS Nano* (2011). 32, 39, 88
- [65] C. Battaglia et al., Light Trapping in Solar Cells: Can Periodic Beat Random?, *ACS Nano* (2012). 32, 85
- [66] V. E. Ferry et al., Light trapping in ultrathin plasmonic solar cells, *Optics Express* **18**, 237 (2010). 32, 39
- [67] H. A. Atwater and A. Polman, Plasmonics for improved photovoltaic devices., *Nature Materials* **9**, 205 (2010). 32, 36, 41, 42, 96
- [68] M. van Exter and A. Lagendijk, Ultrashort surface-plasmon and phonon dynamics, *Physical Review Letters* **80** (1988). 32
- [69] J. Klein-Wiele, P. Simon, and H. Rubahn, Size-dependent plasmon lifetimes and electron-phonon coupling time constants for surface bound Na clusters, *Physical Review Letters* **80** (1998). 32
- [70] D. M. Callahan, J. N. Munday, and H. A. Atwater, Solar cell light trapping beyond the ray optic limit, *Nano Letters* **12**, 214 (2012). 33
- [71] M. A. Green, Estimates of Te and In Prices from Direct Mining of Known Ores, *Progress in Photovoltaics: Research and Applications* **17**, 347 (2009). 33
- [72] B. Soller and D. Hall, Energy transfer at optical frequencies to silicon-based waveguiding structures, *Journal of the Optical Society of America A* **18**, 2577 (2001). 35

- [73] M. Westphalen, U. Kreibig, J. Rostalski, H. Luth, and D. Meissner, Metal cluster enhanced organic solar cells, *Solar Energy Materials and Solar Cells* **61**, 97 (2000). 36
- [74] B. P. Rand, P. Peumans, and S. R. Forrest, Long-range absorption enhancement in organic tandem thin-film solar cells containing silver nanoclusters, *Journal of Applied Physics* **96**, 7519 (2004). 36
- [75] S. S. Kim, S. I. Na, J. Jo, D. Y. Kim, and Y. C. Nah, Plasmon enhanced performance of organic solar cells using electrodeposited Ag nanoparticles, *Applied Physics Letters* **93**, 073307 (2008). 36, 37
- [76] A. J. Morfa, K. L. Rowlen, T. H. Reilly, M. J. Romero, and J. van De Lagemaat, Plasmon-enhanced solar energy conversion in organic bulk heterojunction photovoltaics, *Applied Physics Letters* **92**, 013504 (2008). 36
- [77] D. Duche et al., Improving light absorption in organic solar cells by plasmonic contribution, *Solar Energy Materials and Solar Cells* **93**, (2009). 36
- [78] Y. C. Chang et al., Effects of surface plasmon resonant scattering on the power conversion efficiency of organic thin-film solar cells, *Journal of Vacuum Science & Technology B: Microelectronics and Nanometer Structures* **25**, 1899 (2007). 36
- [79] M. D. Brown et al., Plasmonic Dye-Sensitized Solar Cells Using Core-Shell Metal-Insulator Nanoparticles, *Nano Letters* **11**, 438 (2011). 37
- [80] F. J. Beck, S. Mokkaapati, and K. R. Catchpole, Light trapping with plasmonic particles: beyond the dipole model, *Optics Express* **19**, 25230 (2011). 37, 104
- [81] K. Nakayama, K. Tanabe, and H. A. Atwater, Plasmonic nanoparticle enhanced light absorption in GaAs solar cells, *Applied Physics Letters* **93**, 121904 (2008). 38
- [82] M. J. Mendes, A. Luque, I. Tobias, and A. Marti, Plasmonic light enhancement in the near-field of metallic nanospheroids for application

- in intermediate band solar cells, *Applied Physics Letters* **95**, 071105 (2009). 38
- [83] K. Tvingstedt, N. K. Persson, O. Inganas, A. Rahachou, and I. V. Zozoulenko, Surface plasmon increase absorption in polymer photovoltaic cells, *Applied Physics Letters* **91**, 113514 (2007). 39, 70, 74, 100
- [84] K. Soderstrom, F. J. Haug, J. Escarre, O. Cubero, and C. Ballif, Photocurrent increase in n-i-p thin film silicon solar cells by guided mode excitation via grating coupler, *Applied Physics Letters* **96**, 213508 (2010). 39, 70
- [85] V. E. Ferry, L. A. Sweatlock, D. Pacifici, and H. A. Atwater, Plasmonic Nanostructure Design for Efficient Light Coupling into Solar Cells., *Nano Letters* (2008). 39
- [86] R. a. Pala, J. White, E. Barnard, J. Liu, and M. L. Brongersma, Design of Plasmonic Thin-Film Solar Cells with Broadband Absorption Enhancements, *Advanced Materials* **21**, 3504 (2009). 39
- [87] J. Zhu, C. M. Hsu, Z. Yu, S. Fan, and Y. Cui, Nanodome solar cells with efficient light management and self-cleaning., *Nano Letters* **10**, 1979 (2010). 39, 70
- [88] V. E. Ferry, J. N. Munday, and H. A. Atwater, Design Considerations for Plasmonic Photovoltaics., *Advanced Materials* **22**, 4794 (2010). 39, 70
- [89] J. W. Menezes, J. Ferreira, M. J. L. Santos, L. Cescato, and A. G. Brolo, Large-Area Fabrication of Periodic Arrays of Nanoholes in Metal Films and Their Application in Biosensing and Plasmonic-Enhanced Photovoltaics, *Advanced Functional Materials* **20**, 3918 (2010). 39
- [90] V. E. Ferry et al., Improved red-response in thin film a-Si:H solar cells with soft-imprinted plasmonic back reflectors, *Applied Physics Letters* **95**, 183503 (2009). 39, 40, 70
- [91] V. E. Ferry et al., Optimized spatial correlations for broadband light trapping nanopatterns in high efficiency ultrathin film a-Si:H solar cells., *Nano Letters* **11**, 4239 (2011). 40, 41

- [92] C. Kothandaraman, T. Tonon, C. Huang, and A. Delahoy, Improvement of a-Si:H P-I-N devices using zinc oxide based back-reflectors, *Materials Research Society Symposium* **219**, 475 (1991). 40, 77, 85
- [93] R. H. Franken et al., Understanding light trapping by light scattering textured back electrodes in thin film n-i-p-type silicon solar cells, *Journal of Applied Physics* **102**, 014503 (2007). 40, 42, 96
- [94] F. J. Haug, T. Soderstrom, O. Cubero, V. Terrazzoni-Daudrix, and C. Ballif, Plasmonic absorption in textured silver back reflectors of thin film solar cells, *Journal of Applied Physics* **104**, 064509 (2008). 40, 77, 82, 85, 96
- [95] Sopra nk Database, www.sspectra.com/sopra.html, Courbevoie, 2012. 46, 87
- [96] E. J. Meijer et al., Solution-processed ambipolar organic field-effect transistors and inverters., *Nature Materials* **2**, 678 (2003). 47
- [97] M. Al-Ibrahim et al., Flexible large area polymer solar cells based on poly(3-hexylthiophene)-fullerene, *Solar Energy Materials and Solar Cells* **85**, 13 (2004). 47
- [98] M. M. Alam and S. A. Jenekhe, Polybenzobisazoles As Efficient Electron Transport Materials for Improving the Performance and Stability of Polymer Light-Emitting Diodes, *Chemistry of Materials* **14**, 4775 (2002). 47
- [99] J. Benson-Smith et al., Formation of a Ground-State Charge-Transfer Complex in Polyfluorene-[6,6]-Phenyl-C61 Butyric Acid Methyl Ester (PCBM) Blend Films and Its Role in the Function of Polymer/PCBM Solar Cells, *Advanced Functional Materials* **17**, 451 (2007). 47
- [100] B. Streetman and S. Banerjee, *Solid state electronic devices*, Prentice Hall, New Jersey, 2006. 47
- [101] N. Koch et al., Conjugated organic molecules on metal versus polymer electrodes: Demonstration of a key energy level alignment mechanism, *Applied Physics Letters* **82**, 70 (2003). 47

- [102] J. Y. Lee, S. T. Connor, Y. Cui, and P. Peumans, Solution-processed metal nanowire mesh transparent electrodes., *Nano Letters* **8**, 689 (2008). 48, 74, 100
- [103] D. S. Leem et al., Efficient organic solar cells with solution-processed silver nanowire electrodes., *Advanced Materials* **23**, 4371 (2011). 48, 74, 100
- [104] R. Reif and W. Kern, *Thin Film Processes II: Plasma-Enhanced Chemical Vapor Deposition*, 1991. 48
- [105] M. Kushner, A model for the discharge kinetics and plasma chemistry during plasma enhanced chemical vapor deposition of amorphous silicon, *Journal of Applied Physics* **3**, 2532 (1988). 48
- [106] W. Flack, D. Soong, A. Bell, and D. Hess, A mathematical model for spin coating of polymer resists, *Journal of Applied Physics* **56**, 1199 (1984). 49
- [107] C. Lawrence, The mechanics of spin coating of polymer films, *Physics of Fluids* **31**, 2786 (1988). 49
- [108] R. Swati, R. Banerjee, N. Basu, A. Batabyal, and A. Barua, Properties of tin doped indium oxide thin films prepared by magnetron sputtering, *Journal of Applied Physics* **54**, 3497 (1983). 50
- [109] T. Minami, N. Hidehito, and S. Takata, Highly conductive and transparent aluminum doped zinc oxide thin films prepared by RF magnetron sputtering, *Japanese Journal of Applied Physics* **23**, L280 (1984). 50
- [110] N. Denkov et al., Mechanism of formation of two-dimensional crystals from latex particles on substrates, *Langmuir* **8**, 3183 (1992). 51
- [111] T. Kelf, *Light-matter interactions on nanostructured metallic films*, PhD thesis, University of Southampton, 2006. 52, 53
- [112] R. M. Cole, *Plasmonic properties of metal nanovoids*, PhD thesis, University of Cambridge, 2009. 55

- [113] F. Garcia de Abajo, Colloquium: Light scattering by particle and hole arrays, *Reviews of Modern Physics* **79**, 1267 (2007). 61
- [114] F. Huang and J. J. Baumberg, Actively tuned plasmons on elastomerically driven Au nanoparticle dimers, *Nano Letters* **10**, 1787 (2010). 62
- [115] F. Huang et al., Dressing plasmons in particle-in-cavity architectures, *Nano Letters* **11**, 1221 (2011). 62
- [116] Lumerical FDTD Solutions, www.lumerical.com, Vancouver, 2012. 64, 87
- [117] J. J. Baumberg, Plasmon-Enhanced Low-Cost Photovoltaics, EU Patent **2047521** (2007). 66
- [118] P. N. Saeta, V. E. Ferry, D. Pacifici, J. N. Munday, and H. A. Atwater, How much can guided modes enhance absorption in thin solar cells?, *Optics Express* **17**, 20975 (2009). 66
- [119] M. E. Abdelsalam, P. N. Bartlett, T. Kelf, and J. J. Baumberg, Wetting of Regularly Structured Gold Surfaces, *Langmuir* **21**, 1753 (2005). 66
- [120] T. V. Teperik et al., Omnidirectional absorption in nanostructured metal surfaces, *Nature Photonics* **2**, 299 (2008). 66, 70
- [121] C. Chao, C. Wang, and J. Chang, Spatial distribution of absorption in plasmonic thin film solar cells, *Optics Express* **18**, 11763 (2010). 70, 73
- [122] A. Polman and H. A. Atwater, Photonic design principles for ultrahigh-efficiency photovoltaics., *Nature Materials* **11**, 174 (2012). 71, 75
- [123] H. Hoppe, S. Shokhovets, and G. Gobsch, Inverse relation between photocurrent and absorption layer thickness in polymer solar cells, *physica status solidi (RRL) ? Rapid Research Letters* **1**, R40 (2007). 72
- [124] Y. Kim et al., A strong regioregularity effect in self-organizing conjugated polymer films and high-efficiency polythiophene:fullerene solar cells, *Nature Materials* **5**, 197 (2006). 73

- [125] N. N. Lal et al., Enhancing solar cells with localized plasmons in nanovoids, *Optics Express* **19**, 3918 (2011). 74, 88
- [126] A. C. Atre, A. Garcia-Etxarri, H. Alaeian, and J. A. Dionne, Toward high-efficiency solar upconversion with plasmonic nanostructures, *Journal of Optics* **14**, 024008 (2012). 75
- [127] S. Pillai, F. J. Beck, K. R. Catchpole, Z. Ouyang, and M. A. Green, The effect of dielectric spacer thickness on surface plasmon enhanced solar cells for front and rear side depositions, *Journal of Applied Physics* **109**, 073105 (2011). 77, 99
- [128] S. Standridge, G. Schatz, and J. Hupp, Distance Dependence of Plasmon-Enhanced Photocurrent in Dye-Sensitized Solar Cells, *J. Am. Chem. Soc* **131**, 8407 (2009). 77
- [129] F. J. Haug, T. Soderstrom, O. Cubero, V. Terrazzoni-Daudrix, and C. Ballif, Influence of the ZnO buffer on the guided mode structure in Si/ZnO/Ag multilayers, *Journal of Applied Physics* **106**, 044502 (2009). 77
- [130] V. E. Ferry, A. Polman, and H. A. Atwater, Modeling light trapping in nanostructured solar cells., *ACS Nano* **5**, 10055 (2011). 77
- [131] A. Lin and J. Phillips, Optimization of random diffraction gratings in thin-film solar cells using genetic algorithms, *Solar Energy Materials and Solar Cells* **92**, 1689 (2008). 77
- [132] Asahi Glass Company, VU-type glass, www.agc.com, Tokyo, 2012. 78
- [133] V. E. Ferry et al., Optimized Spatial Correlations for Broadband Light Trapping Nanopatterns in High Efficiency Ultrathin Film a-Si:H Solar Cells., *Nano Letters* **11**, 4239 (2011). 85
- [134] M. A. Green, Enhanced evanescent mode light trapping in organic solar cells and other low index optoelectronic devices, *Progress in Photovoltaics: Research and Applications* **19** (2010). 86

- [135] M. Caglar, S. Ilican, Y. Caglar, and F. Yakuphanoglu, The effects of Al doping on the optical constants of ZnO thin films prepared by spray pyrolysis method, *Journal of Materials Science: Materials in Electronics* **19**, 704 (2007). 87
- [136] M. Green and S. Pillai, Harnessing plasmonics for solar cells, *Nature Photonics* **6** (2012). 96
- [137] J. D. Speed et al., SERS from molecules bridging the gap of particle-in-cavity structures., *Chemical communications (Cambridge, England)* **47**, 6335 (2011). 101
- [138] H. Sai and M. Kondo, Effect of self-orderly textured back reflectors on light trapping in thin-film microcrystalline silicon solar cells, *Journal of Applied Physics* **105**, 094511 (2009). 103
- [139] H. Sai, H. Jia, and M. Kondo, Impact of front and rear texture of thin-film microcrystalline silicon solar cells on their light trapping properties, *Journal of Applied Physics* **108**, 044505 (2010). 103
- [140] J. Springer et al., Absorption loss at nanorough silver back reflector of thin-film silicon solar cells, *Journal of Applied Physics* **95**, 1427 (2004). 103
- [141] P. Campbell and M. A. Green, Light trapping properties of pyramidally textured surfaces, *Journal of Applied Physics* **2033**, 243 (1987). 103, 104
- [142] J. Zhao, A. Wang, M. A. Green, and F. Ferrazza, 19.8% efficient "honeycomb" textured multicrystalline and 24.4% monocrystalline silicon solar cells, *Applied Physics Letters* **73**, 1991 (1998). 103
- [143] J. T. Hugall, J. J. Baumberg, and S. Mahajan, Surface-enhanced Raman spectroscopy of CdSe quantum dots on nanostructured plasmonic surfaces, *Applied Physics Letters* **95**, 141111 (2009). 104
- [144] Y. Yang, S. Pillai, H. Mehrvarz, H. Kampwerth, and M. A. Green, Solar Energy Materials & Solar Cells Enhanced light trapping for high efficiency crystalline solar cells by the application of rear surface plasmons, *Solar Energy Materials and Solar Cells* , 1 (2012). 104